A Survey on Gravity Waves in the Brazilian Sector Based on Radiosonde Measurements from 32 Aerodromes

Alysson Brhian de S. M. S. [1,2], Marco A. Ridenti [1], Marisa Roberto [1], Alessandro J. de Abreu [4,1], José R. Abalde Guede[4,1], Elson de Campos[3]

[1]Aeronautics Institute of Technology (ITA)
[2]Federal Institute of Amazonas (IFAM)
[3]Escola de Especialistas de Aeronáutica (EEAR)
[4]Nacional Institute for Space Researh (INPE)

Key Points:

- Comprehensive survey on GWs using data from 32 locations in the Brazilian territory totaling 49,652 wind and temperature profiles.
- The energy densities of the GWs at each layer are spatially correlated, with a decorrelation distance of approximately 3000 km.
- It was found that waves propagating in the troposphere and low stratosphere are uncorrelated in the studied locations.

Corresponding author: Alysson Brhian, alysson.silva@ifam.edu.br

Abstract

In this paper, we applied a variety of statistical methods to study gravity waves in the troposphere and lower stratosphere in the Brazilian sector, using an unprecedented large database from Instituto de Controle do Espaço Aéreo (ICEA) of radiosonde measurements carried out in 2014 on 32 locations in the Brazilian territory totaling 49,652 wind profiles. The average wind profiles were computed and classified by means of a hierarchical cluster analysis. The kinetic and potential energy densities of the gravity waves were determined using a detrending technique based on the least squares method and the Fast Fourier Transform. The time series of the energy densities were analysed in detail and some persistent and seasonal behaviour was found in some cases. A systematic search for quasi monochromatic waves was carried out and the main characteristics of such waves propagating in the troposphere and the lower stratosphere were found. The correlation analysis between the troposphere and the lower ionosphere based on parameters observed on both layers was used to investigate the wave coupling between the two layers. The results we found have implications in the so-called seeding problem of the equatorial ionospheric irregularities.

Plain Language Summary

Like waves in the ocean that can be easily seen by any observer in the beach, the atmosphere is also permeated by waves of similar nature, called Gravity Waves (GWs). These waves transport energy through the atmosphere, eventually breaking, reflecting or dissipating at some point. In this work we investigated the characteristics of these waves using weather data retrieved by water balloons released from several locations in the Brazilian territory in 2014. By analysing the measurements, we quantified some parameters related to GWs, such as the kinetic and potential energy densities. We also investigated GWs that have well defined frequencies, called monochromatic waves, and determined their wavelengths, phases, amplitudes and phase velocities. We did not find correlations between the wave energies in the troposphere and the low stratosphere, which is an evidence of weak coupling between both layers. This result suggests that GWs are barred in the perturbed, turbulent and windy region between the troposphere and low stratosphere. These results have implications in the so-called seeding problem of the equatorial ionospheric irregularities that occur in the ionosphere. As a science bonus, we also identified the prevailing behaviour of the winds in each of the studied locations.

1 Introduction

Gravity waves (GWs) are atmospheric perturbations caused by the restoring force of gravity that propagate adiabatically in the atmosphere (Gossard & Hooke, 1975; Nappo, 2003; Yigit & Medvedev, 2015). These GWs occur in a stratified atmosphere and are considered internal because they can propagate vertically in the atmosphere, reaching the region of ionosphere in the upper atmosphere (Yigit & Medvedev, 2015). The GWs generated in the lower atmosphere may be associated with seeding sources of plasma bubbles (Kherani et al., 2009) and traveling ionospheric disturbances (TID) (Yigit & Medvedev, 2015). Furthermore, GWs generated in the lower atmosphere can break down and generate other GWs in the highest altitudes, as demonstrated by Vadas et al. (2003), quoted by Yigit (2015) and simulated by Heale *et. al.* (2020). The GWs are responsible to add energy and momentum in middle and high atmosphere. So their real-time characterization might predict whether there will be a TID in short or long-term.

The GWs are usually formed by natural events such as topographic sources, tropospheric convections, jet streams, shear instability, geostrophic adjustment, orographic forcings, frontal systems, turbulence and interaction between waves-waves or even human events such as nuclear bomb or mines (Gossard & Hooke, 1975; Fritts & Alexan-

der, 2003; Azeem et al., 2015; Yigit, 2015; Oliveira et al., 2016; Huang et al., 2019; C. Heale et al., 2020). In the troposphere and lower stratosphere (TLS), the average vertical wavelength is about 5.5 km in the troposphere and 3.5 km in the stratosphere (S. Zhang & Yi, 2005). Furthermore, in the troposphere, the amount of events and intensity are associated with annual seasonality and in the stratosphere with the quasi biennial oscillation (QBO) (Y. Zhang et al., 2012; C. Heale et al., 2020).

Historically, the GWs in the TLS have been studied experimentally using microbarometers, kites, aircraft, radars, sodars, lidars and satellites (Nappo, 2003). In this paper, the GWs were identified using measurements from meteorological balloons (radiosondes), which was the same approach used by Youshiki and Sato (2000), who studied the GWs at the Earth's poles. Other similar GW's studies were carried out in other geographic locations: Zink and Vicent (2001), in Macquarie Island, Australia; S. Zhang and Yi (2005), in Wuhan, China and Oliveira et al. (2016), in Rio Grande do Norte, Brazil. These radiosondes carried by weather balloons reach up to approximately 30 km (Fritts & Alexander, 2003; Brasil, 2020) and measure wind and temperature along its path (WMO, 2018), among other meteorological variables. These measurements provide quantitative information about GWs (Allen & Vincent, 1995; Nappo, 2003). Also, radiosondes are the only instruments capable of measuring the kinetic and potential energy of gravity waves (Geller & Gong, 2010).

This work analyzed radiosonde measurements carried out in 2014 at 32 aerodromes throughout Brazil by the *Instituto de Controle do Espaço Aéreo* (ICEA). Officially, these radiosondes were launched daily at 0000 and 1200 UTC, with the purpose of providing information of the lower atmosphere for research, weather forecast and aeronautics (Brasil, 2013, 2017; WMO, 2018). As long as we are concerned, this is the first work that investigates GWs systematically using radiosonde measurements from a broad net of stations (or aerodrome) distributed throughout the Brazilian territory. We computed the time averages of the wind profiles and performed a cluster analysis on them to identify regions where the prevailing winds have similar behaviour. The time averages were computed for two different samples; the first covered the dry season (fall-fa/winter-wi) and the other the wet season (spring-sp/summer-su). This analysis showed, as expected, that regions having similar latitudes tend to cluster. Signal processing techniques, such as Fast Fourier Transform (FFT) and Least Squares Minimum (LSM), were used to extract quantitative information related to the GWs from the measured profiles. The magnitude of the variability of the velocity components was quantified by integrating the power spectrum density (PSD), yielding an estimate of the kinetic energy of the GWs. The potential energy of the GWs was estimated in a similar fashion using the temperatures profiles. We also investigated the spatio-temporal correlation between the energies measured at different aerodromes. Finally, we identified and studied quasi monochromatic GWs in the TLS, finding good agreement between our results and the results reported in the literature (Vicent & Alexander, 2000; S. Zhang & Yi, 2005).

This article is divided into the following parts: the first part presents the experimental methodology and the data analysis techniques that were used to extract quantitative information from radiosonde data; the second one presents the results and discussions; and the last one summarises the main conclusions.

2 Methodology

The radiosonde's measurements used in this paper were collected in 32 aerodromes throughout the Brazilian territory at 2014, as shown in Figure 1. The radiosondes performed measurements of wind, temperature, humidity and pressure as a function of altitude and sent them to the ground station per radio signal. All the launches of radiosondes officially take place in Brazil at 0000 and 1200 UTC and usually start 30 to 45 min

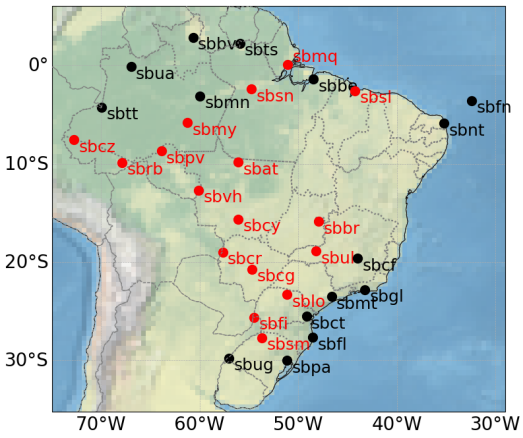

Figure 1. *These are all aerodromes operated by the ICEA during 2014 - red dots indicate aerodromes that have been operating since 2009. The characteristics of the aerodromes are shown in Table Appendix A.*

before the standard time, according national and international recommendations (Brasil, 2013; WMO, 2018; Brasil, 2017).

In some dates in 2014 the measurements were not performed and these cases were classified as missing data or not available (NA). The Figure 2 shows the smoothed histograms of the sample size for all aerodromes over one year, also over the dry and wet seasons for different atmospheric layers (troposphere and lower stratosphere) and different physical quantities (kinetic energy and potential energy), which will be defined later. There was a large number of aerodromes where measurements were performed almost every day, totalling almost 730 measurements. Typically, more measurements were carried out during the dry period (fall/winter). Table 1 shows the amount of profiles analysed by period, kind of energy and atmospheric layer, summing up a total of 49,652 profiles.

Table 1. Number of altitude profiles used to estimate the potential and kinetic energy densities in 2014 for the 32 aerodromes. The distribution of these values are shown in Figure 2.

		Dry	**Wet**	Total
Troposphere	**Kinetics**	7,296	6,332	13,628
	Potential	6,659	6,457	13,116
	Total	13,955	12,789	*26,744*
Lower Stratosphere	**Kinetics**	5,380	5,094	10,474
	Potential	6,503	5,931	12,434
	Total	11,883	11,025	*22,908*

Using the wind and temperature altitude profiles, we estimated the kinetic and potential energy densities of the GWs in the troposphere (surface-11 km) and lower stratosphere (18-25 km). The kinetic energy E_K and the potential energy E_P are defined as (Stull, 1988; Vicent & Alexander, 2000; Youshiki & Sato, 2000; S. Zhang & Yi, 2005; Geller & Gong, 2010, 2010):

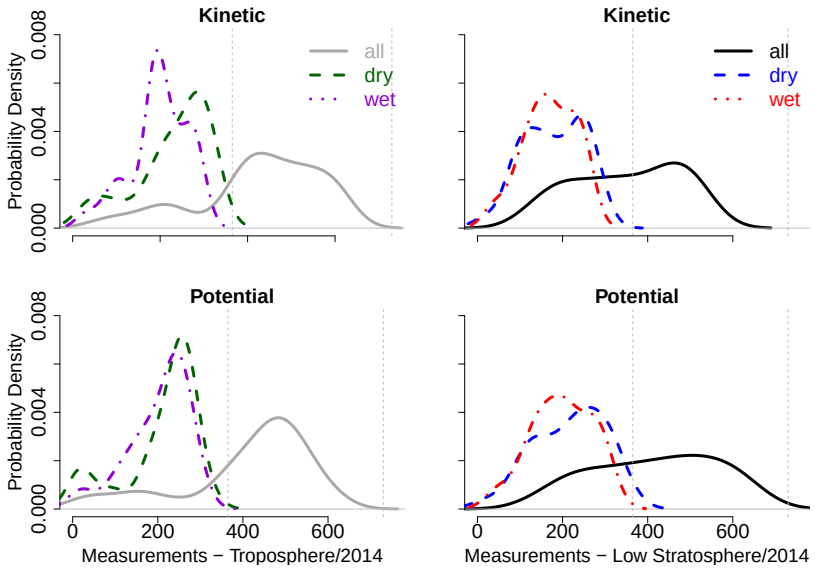

Figure 2. Probability densities associated with the distribution of measurements in 2014 at 32 aerodromes. The upper figures correspond to measurements from which the kinetic energy densities were estimated, while the lower figures correspond to measurements from which the potential energy densities were estimated. The figures on the left correspond to the troposphere and the figures on the right correspond to the lower stratosphere.

$$E_K = \frac{1}{2}(\overline{u'^2} + \overline{v'^2}) \tag{1}$$

$$E_P = \frac{1}{2}\left(\frac{g\overline{T'}}{N T_0}\right)^2 , \tag{2}$$

where $N = g\sqrt{\frac{\gamma-1}{\gamma}\frac{M_{air}}{RT_0}}$ is the *Brunt-Väisälä*'s frequency, overline means the average values, primed variables correspond to wave oscillations, u is the zonal wind, v is the meridional wind, $g = 9.80665$ m/s^2 is the mean gravitational acceleration, $\gamma = 1.4$ is the adiabatic index of air, $M_{air} = 28.9647 \times 10^{-3}$ kg/mol is the molar mass of air, $R = 8.314463$ J/(mol·K) is the ideal gas constant and T' is the temperature normalized by $T_0 = T_0(z)$ background temperature. Since the data was not regularly spaced in altitude, the wind and the temperature profiles were interpolated to a 50 m grid.

The estimate of primed amplitudes was made by Least Squares Method (LSM), procedure that remove the background wind assuming that it had a parabolic shape (Vincent & Eckermann, 1997; S. Zhang & Yi, 2005). After removing the trend, the Power Spectrum Density (PSD) was computed using the Fast Fourier Transform (FFT) (Stull, 1988; Press et al., 2007; Martinson, 2018). The quadratic sum of the FFT components yields the mean kinetic and potential energy densities (Stull, 1988). The mean square of the primed quantities is computed as (Vicent & Alexander, 2000; S. Zhang & Yi, 2005):

$$y' = y - \hat{a}h^2 - \hat{b}h - \hat{c} , \tag{3}$$

$$\overline{y'^2} = \frac{1}{2M}\sum_{k=0}^{M-1} Y'_k Y'^*_k , \tag{4}$$

where $\hat{a}$, $\hat{b}$ and $\hat{c}$ are coefficients to be determined, $Y_k^{'}$ is the FFT component and $Y_k^{'*}$ its conjugate and M is the size of the time/spatial series. An example of a detrended profile is shown in Figure 3.

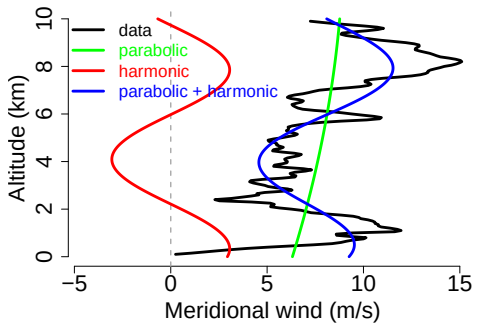

Figure 3. Meridional wind from aerodrome SBMN (Manaus - Brazil) measured in 05/14/2014 12 UTC (black) and the fitting curve (blue). The lines corresponding to the harmonic (red) and parabolic (green) contributions for the fitting curve are also shown.

The energy densities are computed for all valid height profiles. The overall statistics of the energy density provides information about the state of perturbation of the TLS. However, the wind dominant wavelength and the temperature dominant wavelength were not always consistent with each other. Therefore, we also searched for the particular cases where the wavelength of the three experimental variables were compatible, as expected in the case of a monochromatic wave, using the coefficient of variation (CV). The first guess for the monochromatic vertical wavelength is the frequency of the highest FFT component. A linear LSM (Press et al., 2007) was used to estimate the phase and amplitude, while the vertical wavelength was estimated using a search algorithm that performed a LSM fitting for each wavelength value in a evenly spaced grid with spacing $\Delta\lambda = 25$ m between 0.5 and 12.0 km. We considered that a quasi-monochromatic GWs occurred when the coefficient of variation (CV) of the three wavelengths was less than or equal to 20%, following the same approach of S. Zhang and Yi (2005). The CV is defined as the ratio between the standard deviation σ_{λ_z} to the mean $\overline{\lambda_z}$ from the vertical wavelengths (Devore, 2016):

$$CV = \frac{\sigma_{\lambda_z}}{\overline{\lambda_z}}. \tag{5}$$

In order to verify the existence of a trend in the time series of the kinetic and potential energies we used a nonlinear smoother called Centered Moving Medians (MdC) with bandwidth equal to h. The median is a robust measure of the central tendency, defined as the value separating the higher half from the lower half of a data sample. The median has the advantage of not being influenced by outliers. If $\{X_1, X_2, \ldots, X_N\}$ is a time series of size N, then the MdC filter is defined as (Cowperwait & Metcalfe, 2009; Arce, 2005):

$$Y_i = Md[X_{i-h}, ..., X_i, ..., X_{i+h}] \ , \tag{6}$$

where i ranges from $h+1$ to $N-h$. Note that the MdC filter can not be applied to data samples where $i \leq h$ or $i \geq N-h$.

Volatility (or dispersion) is defined as the square root of the variance of a sequence of random variables. It is a simple numerical measure widely used in the financial market to estimate how much a given stock changes around the mean (Sinclair, 2013; Gregorius, 2009). This measure is useful since it quantifies how rapidly one random variable varies in time, but it is not statistically robust. In this work, we employed a nonlinear and robust measure called interquartile distance Iq, which is defined as the distance between the third and first quartile of a sample (Devore, 2016). The interquartile distance was used to quantify how far the energy values have moved away from the median of a given centered period equal to $2h+1$. The Centered Moving Interquartile IqC filter is defined as:

$$Y_i = Iq[X_{i-h}, ..., X_i, ..., X_{i+h}] \tag{7}$$

where i ranges from $h+1$ to $N-h$. Here also, the IqC filter can not be applied to data samples where $i \leq h$ or $i \geq N - h$.

We used the Spearman's correlation coefficient to investigate the spatial correlations in the kinetic and potential energies between distinct aerodromes. We opted for this non-parametric and nonlinear statistics because the data was not normally distributed (Devore, 2016). The Spearman's coefficient consider positive correlation (or monotonic increase) when its value is close to 1, negative correlation (or monotonic decrease) when its value is close to -1 and without correlation when its value is close to 0 (Kanji, 2006; Gibbons & Chakraborti, 2011; Bagdonavicius et al., 2011; Bishara & Hittner, 2012). The correlation coefficients were plotted against the Haversine distances between the aerodromes (Brummelen, 2013).

The wind and temperature profiles were studied using cluster analysis. In what follows, we describe step-by-step the procedure used in the cluster analysis. First, a metric was chosen to calculate the distance between one profile to another - the Euclidean's distance metric. As there were 32 stations, then $\binom{32}{2} = 496$ distance measurements were need to build the dissimilarity matrix (or proximity). Second, the aerodromes were separated in 5 groups, according to the usual geographic divisions based on the physical characteristics; North, Northeast, Southeast, South and Midwest (*IBGE*, 2022). Third, the following linking methods were chosen and tested: average, single, complete and ward (Hair et al., 2006). Finally, the optimized group was found using the agglomerative coefficient (AC), defined as (Pandove et al., 2018; Kaufman & Rousseeuw, 2005):

$$AC = \frac{1}{n}\sum_{i=1}^{n}[1 - r(i)] \ , \tag{8}$$

where n is the total number of profiles and $r(i)$ is the distance from the first cluster where it was inserted divided by the distance in the final step of the algorithm. The values of AC range from 0 (indicating that no clustering was found) and 1 (indicating strong clustering structure).

3 Results

3.1 Wind Profiles

The temporal mean of the meridional and zonal winds height profiles were computed for each location, for each atmospheric layer of the TLS and for each season, *i.e.*, the dry and wet seasons, which were defined earlier. The temporal mean of the profiles give us a measure of the prevailing winds. The meridional winds are stronger than the zonal winds and hence (Rossby & Willet, 1948), are easily to differentiate. The cluster analysis was applied to group the profiles according to common features. Our expectation was that applying the cluster analysis to the wind profiles at a given atmospheric

layer and time period, we would find the similarities among them. As a matter of fact, this was verified. The results of the cluster analysis for samples in the each layer and period are shown on Figure 5 and 4. The five clusters were labeled by colors red (R), green (G), orange (O), cyan (C) and blue (B) and are also represented in the geographic map in Figure 6, showing that the profiles cluster according to latitude range. The hodographs in Figure 7 and Figure 8 show the behavior of the prevailing winds in the grouped samples, facilitating the comparison between the wind profiles and the identification of similarities among samples of the same group.

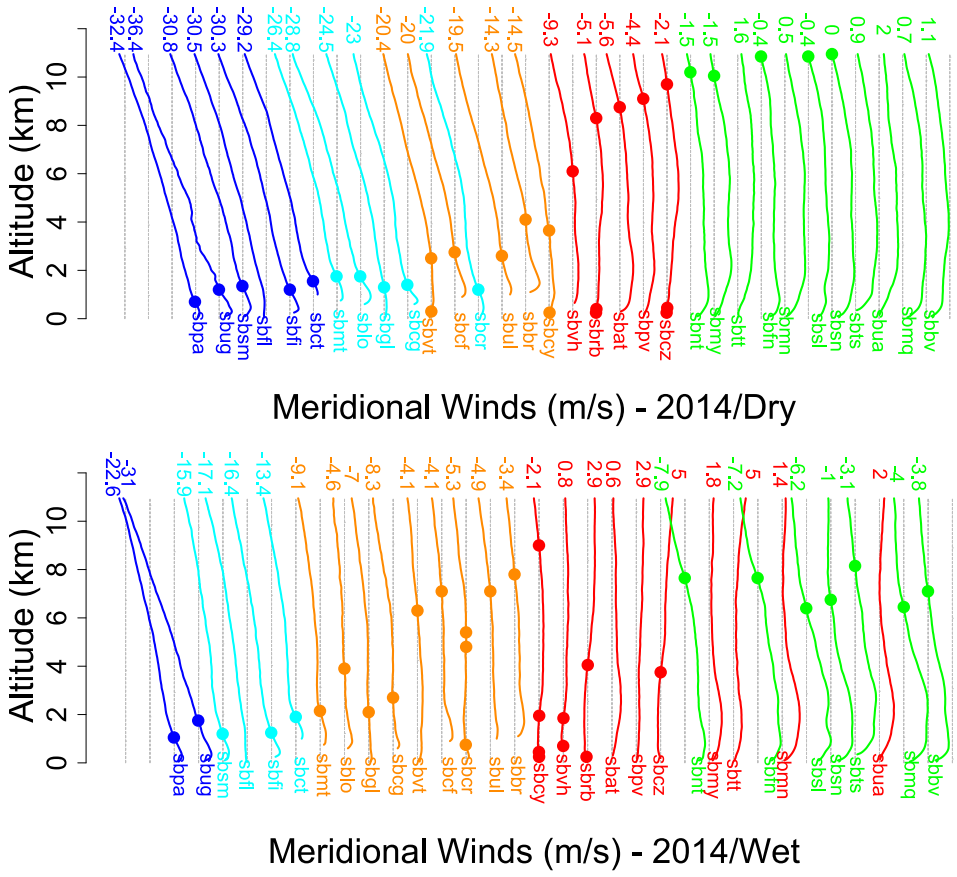

Figure 4. Profiles of the prevailing meridional winds in the troposphere for the dry and wet seasons in 2014. Each profile is translated to the right in 10 m/s. The bullets on the curves highlight the zero values of the winds, showing the point of change in the wind direction. The numeric values colored in the top are the intensity winds (m/s) in that altitude. The position of the profiles in the figure follows the geographic position of the respective aerodrome, going from the southernmost on the left to the to the northernmost on the right. Each color represents one of the computed clusters.

The cluster analysis have shown that wind profiles located in the same latitude range usually have similar features. This was expected since the atmospheric circulation cells have a strong latitudinal dependence. Also, the regions in the same latitude range are equally affected by the Coriolis force. The wind profiles (Figure 6 and the hodographs in Figure 8) have shown that clusters R and G, near the equator, have remarkable similarities. The clusters C, B and O, in the south, also have similar features, but they differ significantly from clusters R and G, located near the equator. Besides the differences

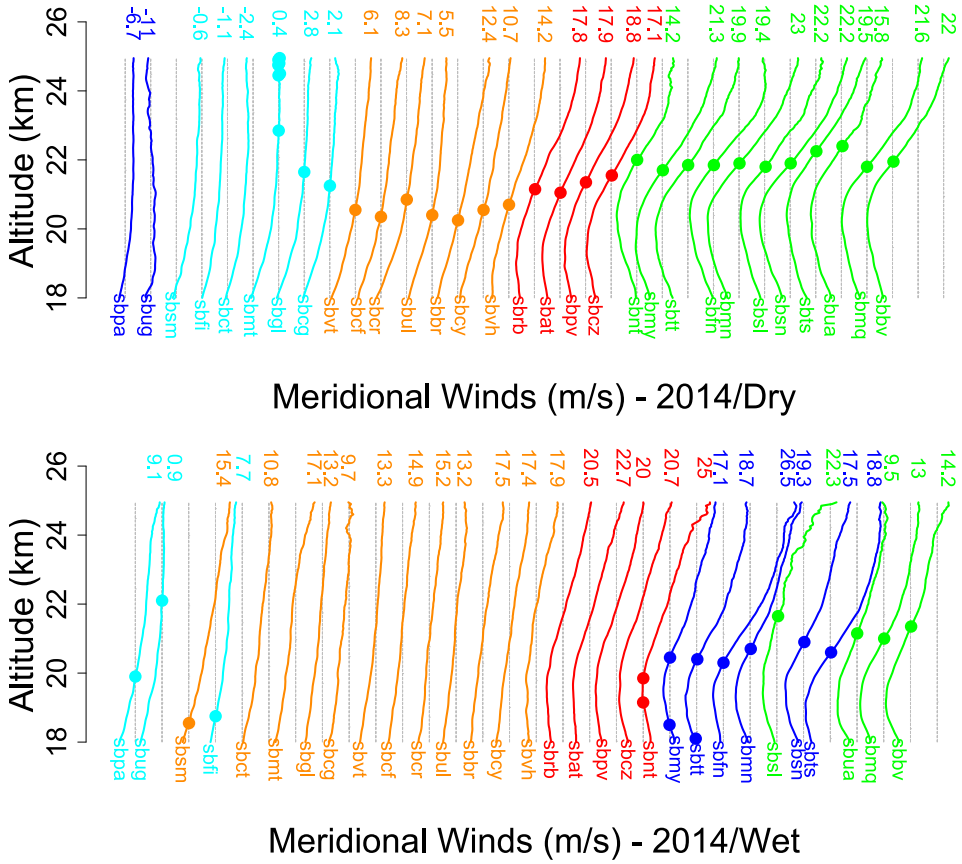

Figure 5. Profiles of the prevailing meridional winds in the lower stratosphere for the dry and wet seasons in 2014. Each profile is translated to the right in 10 m/s. The bullets on the curves highlight the zero values of the winds, showing the point of change in the wind direction. The numeric values colored in the top are the intensity winds (m/s) in that altitude. The position of the profiles in the figure follows the geographic position of the respective aerodrome, going from the southernmost on the left to the to the northernmost on the right. Each color represents one of the computed clusters.

in the wind profiles due to latitude, there are also some significant dependence of the wind profiles on the seasons. In what follows, we discuss in more detail these differences, since it will help us to interpret the results on GWs.

In general, the prevailing winds near surface are northward and weaker in magnitude. They are northward because winds near the ground move towards the Intertropical Convergence Zone (ITZC), a low pressure region near the equator. The winds near the ground are weaker due to the Planetary Boundary Limit (PBL), which is the attenuation of the wind motion in the fluid boundary layer (Ahrens & Henson, 2018; Lu & Vecchi, 2015). At higher altitudes, the prevailing winds change their direction, moving southward, closing the so called Hadley's cell, a convective roll located between the equator and the tropics where the winds next to the ground converge to the ITZC. At the top of the troposphere, the results show not only that the winds change direction, but also increase in magnitude. The magnitude of the southward winds at the top of the troposphere also changes as a function of latitude, increasing towards the south (see Figures 4 and 8). Also, the comparison between the tropospheric wind profiles in the dry

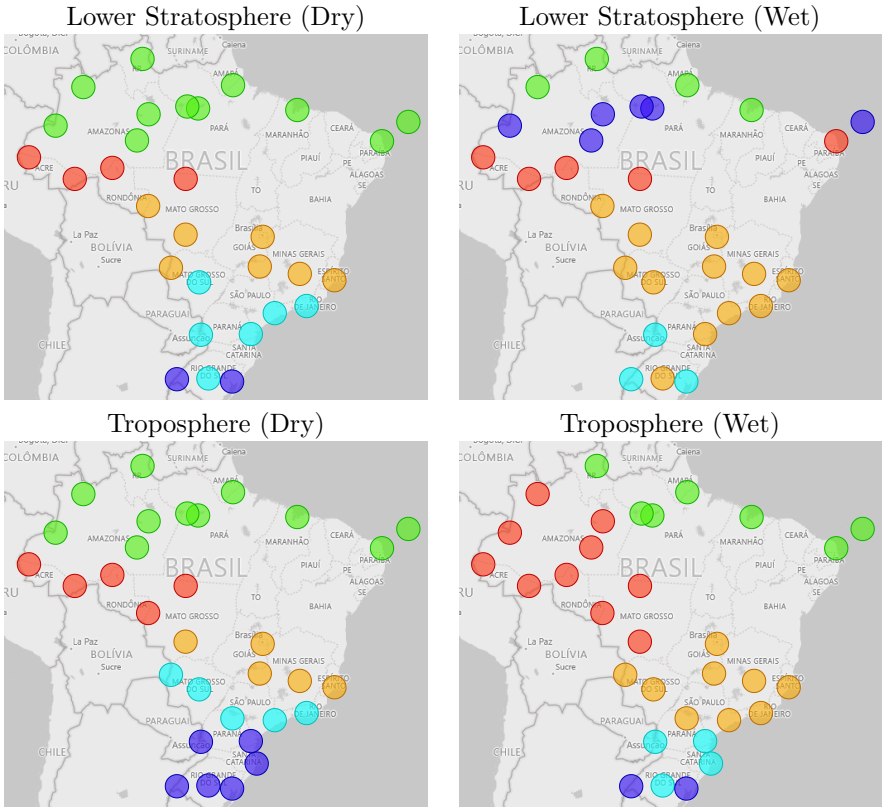

Figure 6. The points locate the aerodrome position on the map while the color indicates to which cluster it belongs according to the atmosphere layer (troposphere/lower stratosphere) and season (dry/wet).

season with the wind profiles in the wet season shows a significant increase in magnitude of the southward winds at the top of the troposphere. This last observation is specially relevant, because it helps to explain why the GWs in the troposphere seems to be more active in the dry season, as we will see later.

As mentioned earlier, the intermediate region between the troposphere and the low stratosphere was not analyzed systematically. This region contains the tropopause and it is characterized by intense winds and turbulence, which overlap in a complicated way with the GWs. To illustrate that, we show an example of an hodograph in Figure 9 where very intense winds occur in this transition region. This hodograph shows a jet stream with wind magnitudes reaching up to 70 m/s in a location between 20 and 30°, where the encounter between the Hadley cell and the Ferrel cell is expected. As we will see later, the turbulence and the high convection speeds in this transition layer explain the uncoupling between GWs in the troposphere and the low stratosphere. GWs that propagate into this perturbed intermediate layer tend to be absorbed or destroyed (Rossby & Willet, 1948; Mastrantonio et al., 1976; Fritts & Alexander, 2003; Archer & Caldeira, 2008; Yigit, 2015; Ahrens & Henson, 2018).

The wind profiles were analysed in the altitude range between 18 km and 25 km to study the lower stratosphere. The tropopause was purposely avoided, because, as explained in the Methodology section, the analysis of the GWs requires the exclusion of the tropopause altitude range and requires a constant gradient of temperature. The way the samples grouped into clusters was similar to the troposphere case, *i.e.*, the merid-

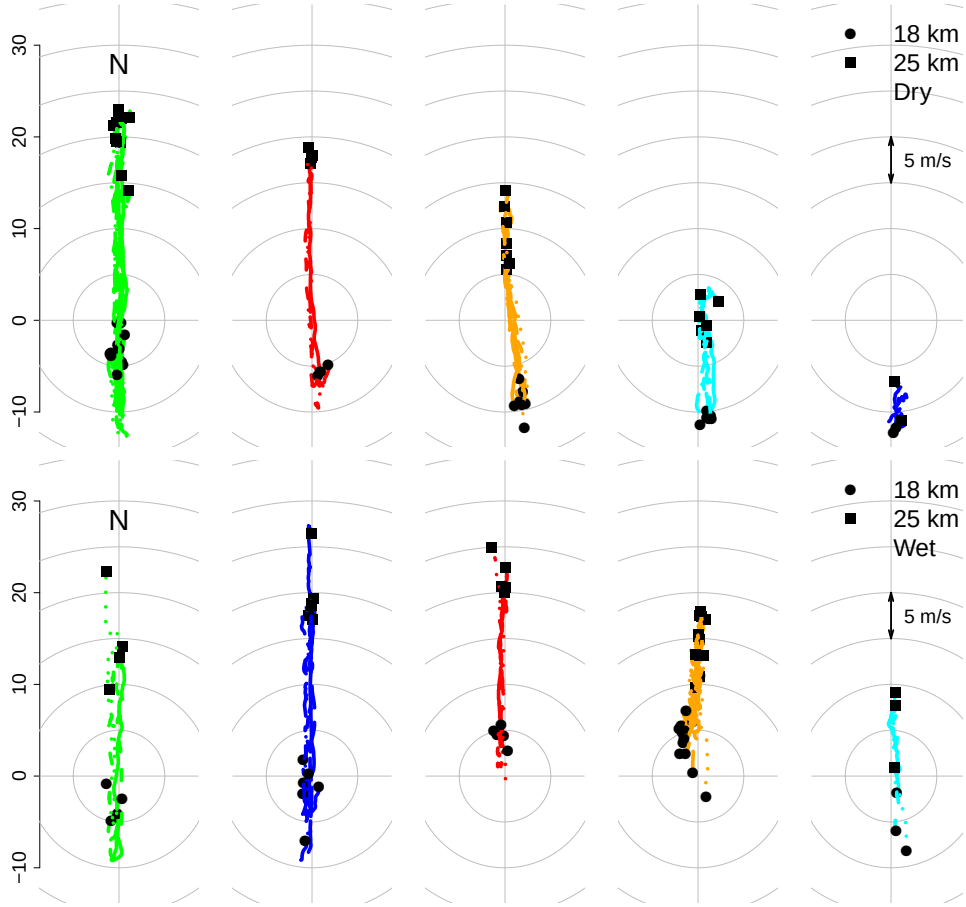

Figure 7. Hodographs grouped according to the cluster analysis of the meridiondal winds in the lower stratosphere in 2014. The top panels refer to the dry season, while the bottom panels refer to the wet period.

ional winds grouped around the latitude (Vincent & Eckermann, 1997) – see map in Figure 6.

The profiles of the meridional winds in Figure 5 and the hodographs in Figure 7 show that the winds near 18 km tend southward and the winds at higher altitudes tend northward. The change of direction in the winds in the lower stratosphere occurs at higher altitudes in the dry period. The magnitude of the winds near the equator at 25 km is stronger than the magnitude of the winds in middle latitudes at the same altitude. The direction (northward) and the stronger intensities (at 25 km) are consistent with the Brewer-Dobson's Circulation pattern. This circulation pattern considers one cell that starts near the equator (or ICTZ) and end up at high latitudes or near the poles. The strong flux of air from troposphere to stratosphere near the ICTZ explains most of the dynamics of the profiles (Brewer, 1949; Salby & Callaghan, 2005; Butchart, 2014; C. Heale et al., 2020). Figure 6 show how the clusters of the wind profiles in the lower stratosphere are located geographically. As we can see, the profiles group according to latitude ranges.

3.2 Gravity waves

As in the case of the study of the wind profiles, here we also split the analysis according to atmosphere layer (troposphere/ low stratosphere) and the season (dry/wet).

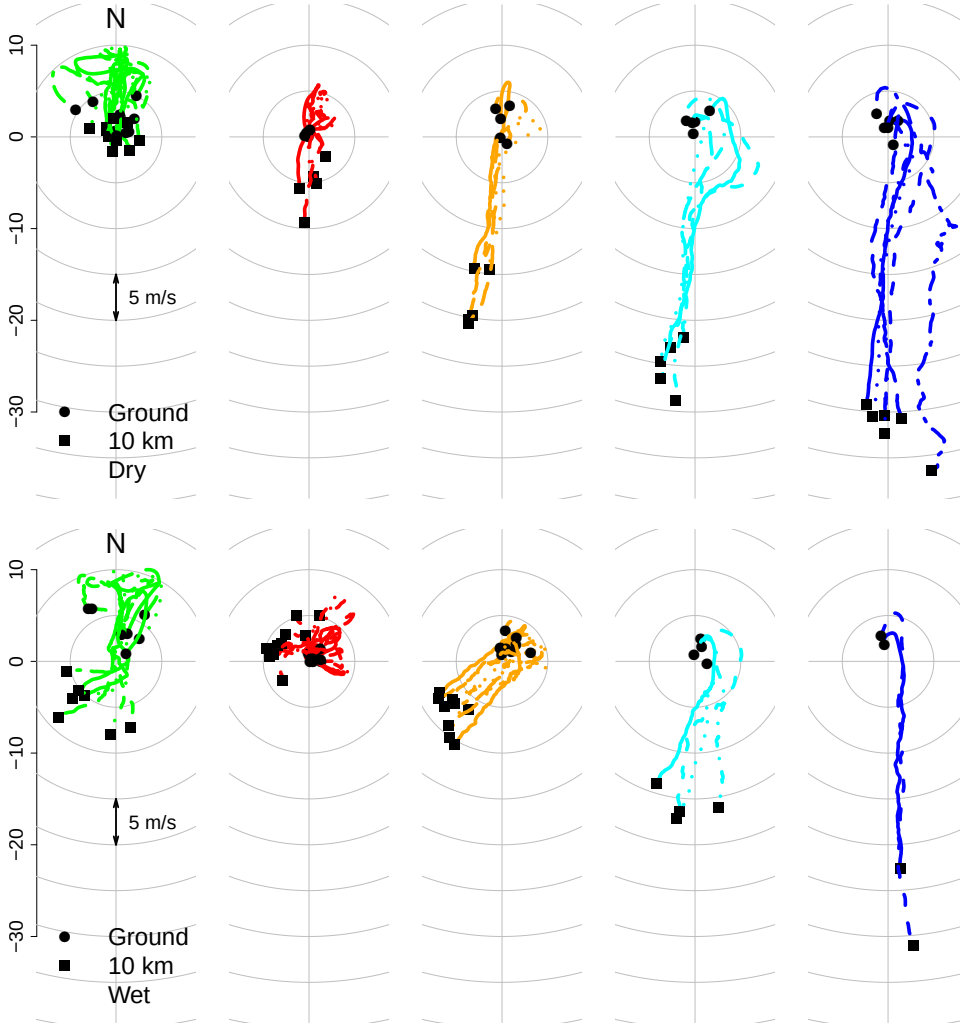

Figure 8. Hodographs grouped according to the cluster analysis of the meridiondal winds in the troposphere in 2014. The top panels refer to the dry season, while the bottom panels refer to the wet period.

For each condition and each aerodrome, the distributions of the kinetic and potential energies were studied by fitting the corresponding histograms to the gamma and normal distributions. In the end, we calculate the average and standard deviations of each fitting parameter, shown on Table 2. We also note that, in general, the distribution of the energies did not depend on the time of the day when it was collected, whether it was dusk or dawn (data not shown here). The adherence's test of Kolmogorov-Smirnov was used to test the adherence of the fitted distribution to the data. The p-values computed for the gamma distribution fittings have shown, with a level of significance of 5%, that the null hypothesis could not be rejected. In other words, the gamma distribution provided good fits for the distributions of both kinetic and potential energies.

The histograms and fitting parameters showed that the energies in the lower stratosphere were typically greater than the energies in the troposphere, possibly due to the expected increase of the amplitude in the upper layers. Besides, the energy densities in the dry season are typically greater than the energy densities in the wet season (Vincent & Eckermann, 1997; Nappo, 2003).

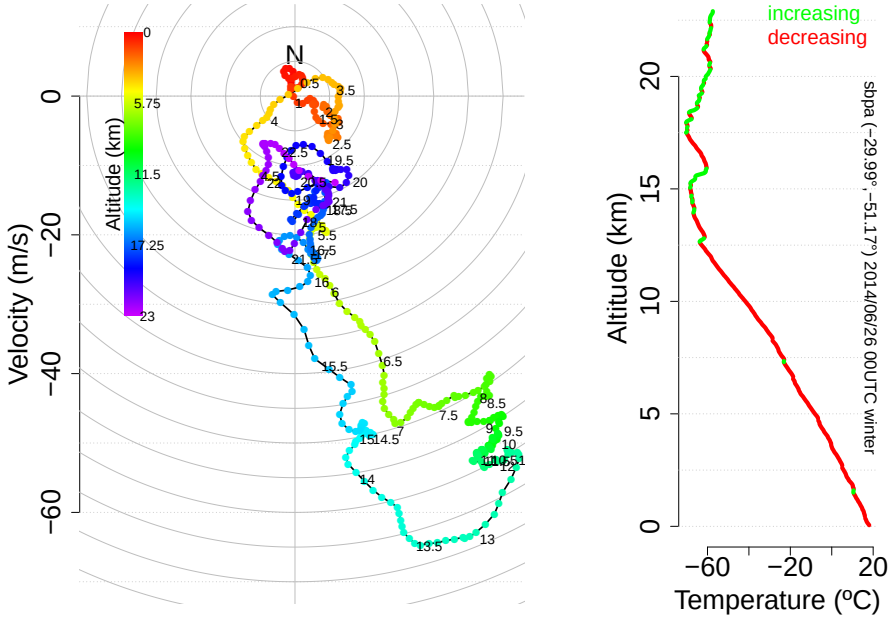

Figure 9. Hodograph (left) and temperature profile (right) from sbpa's aerodrome $(-29.99°, -51.17°)$ on 26^{th}, June 2014 at 00 UTC. The increasing and decreasing represent when the temperature gradient are respectively positive or negative. Observe the peak of velocity near the tropopause ($\sim$ 13 km), an evidence of the presence of a jet stream.

Table 2. Average values, computed over the 32 aerodromes, of the parameters of the gamma and normal distributions of the energy densities. The values are separated by atmospheric layer, troposphere (T) and lower stratosphere (S), and period, dry and wet. We used the Kolmogorov-Smirnov's adherence test with 5 % of significance level. (The values a ± b represents the average ± one standard deviation).

		Kinetic		**Potencial**	
		Dry	**Wet**	**Dry**	**Wet**
GAMMA	**S**	3.5±1.8	2.6±0.7	2.2±0.4	1.9±0.4
		(4.9±3.3)	(5.1±2.5)	(5.8±2.4)	(6.2±1.5)
shape[adimensional]	**T**	3.2±0.8	3.3±0.7	2.2±0.6	2.5±0.8
(scale[J/kg])		(2.8±1.1)	(2.3±0.8)	(2.7±1.2)	(1.7±0.8)
NORMAL	**S**	14.1±6.5	12.3±4.0	12.4±4.2	12.1±3.0
		(7.6±4.0)	(7.1±2.5)	(9.1±3.6)	(8.8±1.9)
mean[J/kg]	**T**	8.3±1.6	7.3±1.6	5.4±1.8	3.8±1.1
(sd[J/kg])		(6.8±4.9)	(5.4±2.9)	(4.9±4.0)	(3.1±1.5)

In Figure 10 we show the time series of the energy densities in 2014 for the troposphere and the lower stratosphere. The lines in gray are the moving median ($h = 15$) for each aerodrome, the black line is the average over all aerodromes and the red lines are the envelopes formed by the addition and subtraction of one standard deviation about the average. The energy densities at the lower stratosphere had a greater dispersion than the energy densities at the troposphere. Also, the average values in the lower stratosphere

were around 50% higher than the values in the troposphere. This observation is consistent with the expected increase of the wave amplitudes as a function of altitude.

The energy densities in the troposphere were greater in the dry season (mainly in the end of winter), a behaviour that was also observed in a study using radiosonde measurements in Australia (Allen & Vincent, 1995) and in US (Geller & Gong, 2010). The increased values of the kinetic energy densities in the dry season may be related to the wind dynamics of this period, that is characterized by stronger meridional winds, also confirmed by our measurements (Figure 7). In the lower stratosphere case, there was a slight increase in the kinetic energy density in the dry period (Allen & Vincent, 1995; Alexander et al., 2010; Geller & Gong, 2010), but no clear trend in the potential energy density. Also, the kinetic energy density in the low stratosphere was typically greater than the potential energy (Vicent & Alexander, 2000).

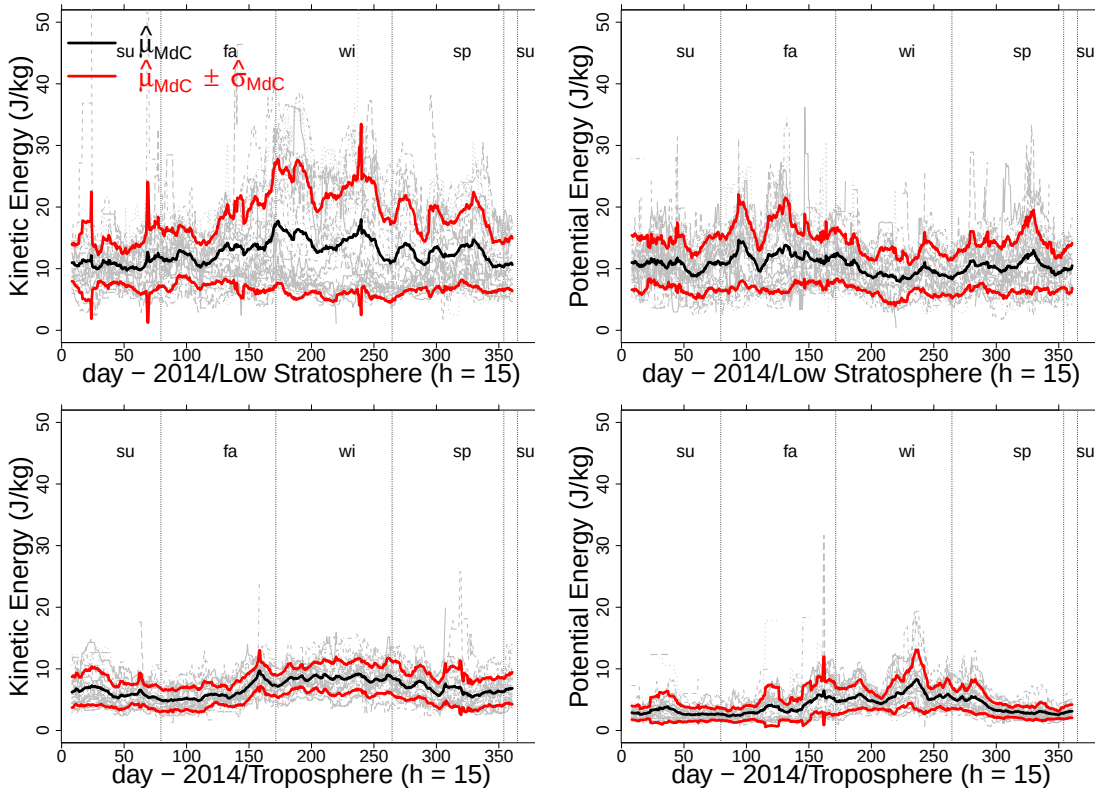

Figure 10. The lines in gray are the moving median (h = 15) for each aerodrome, the black line is the average over the aerodromes and the red lines are the envelopes formed by the addition and the subtraction of one standard deviation about the average.

The plots in Figure 11 show the dispersion (or volatility) of the kinetic and the potential energy densities in the troposphere and the lower stratosphere. In this analysis, the outliers and missing data were filtered using the Centered Moving Interquartile Distance (IqC), with h = 15. The gray line represent each aerodrome, the black one represents the mean over the aerodromes and the green one represent the mean ± one standard deviation.

The average volatility values were smaller in the troposphere, for both kinetic and potential energy densities. This was already clear in Figure 10, which shows that the dispersion of the energy densities were remarkably larger in the lower stratosphere. These

results show that either the variability of the energies are amplified in the transition from the troposphere to the lower stratosphere or the variability is produced in the lower stratosphere itself from perturbing processes that are not related to the state of the troposphere below 12 km. The correlation analysis between the energies at different strata will show that the former statement is the most probably true.

The results also show that the volatility of the potential energy density in the troposphere was greater in the dry period, a behavior that was also found in measurements from Australia (Allen & Vincent, 1995). On the other hand, the volatility of the kinetic energy density on the troposphere increased only slightly in the dry season. In the lower stratosphere, only the volatility of the kinetic energy presented a slight increase in the dry season. As in the previous case, all time series of volatility in 2014 had high persistence - similar to the behavior of a pink noise.

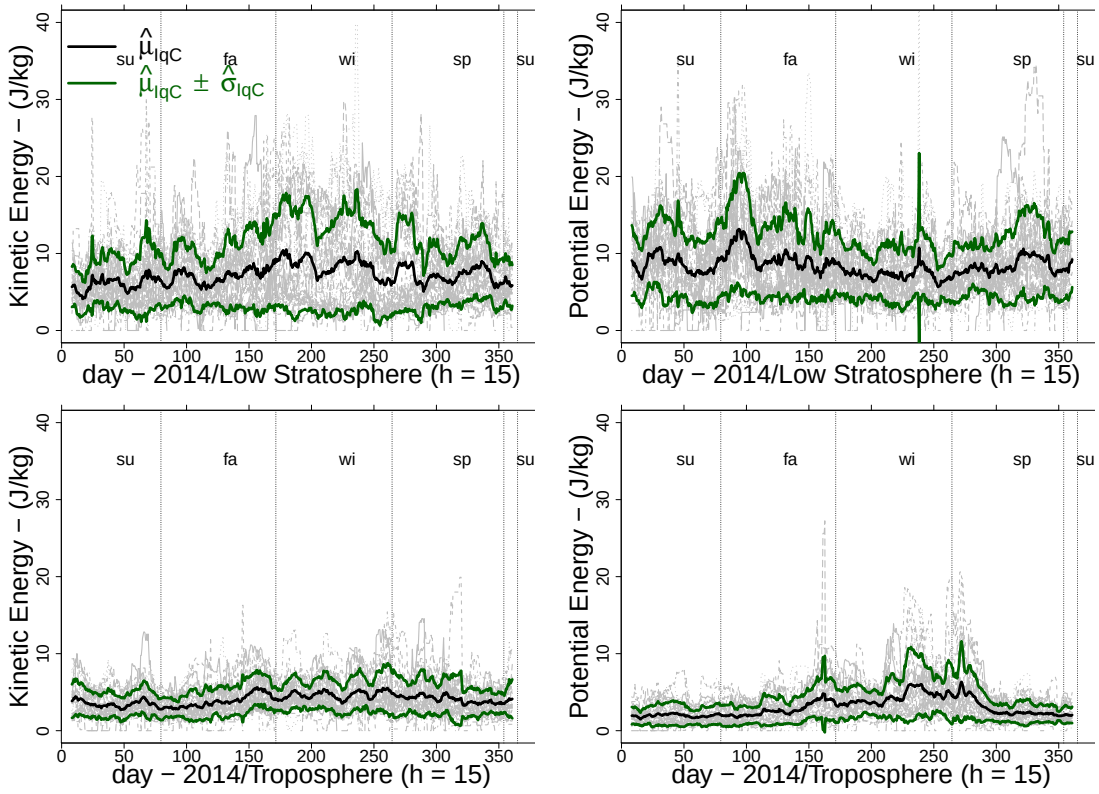

Figure 11. Volatility of the kinetic (left) and potential (right) energy densities in 2014 for each aerodrome (gray line) at the troposphere (below) and lower stratosphere (top). The Centered Moving Interquartile Distance (IqC) with h = 15 was used to smooth the time series. The black line refers to the average over all aerodromes and the green envelopes represent ± one standard deviation.

The spatial correlation between the energy densities of each aerodrome was computed from the total pairwise combinations of aerodromes $\binom{32}{2} = 496$. The correlation coefficient (Spearman's coefficient) for each pairwise combination is plotted against their distances in Figure 12. From this analysis, it is possible to compute the typical decorrelation distance, *i.e.*, the distance below which the GW energy densities are still spatially correlated. Our analysis showed that the decorrelation distance is approximately 3,000 km ($\sim 27°$) in the troposphere and approximately 3,900 km ($\sim 35°$) in the lower stratosphere, as shown in Figure 12. In all cases, the correlation coefficient is typically

positive. Besides, the closer the aerodromes are the higher are the coefficient values. This result confirms what we expected from previous knowledge about GWs: the waves manifest collectively in a large volume of the atmosphere, so the closer are the measurement spots, the higher is the probability to get similar measurements.

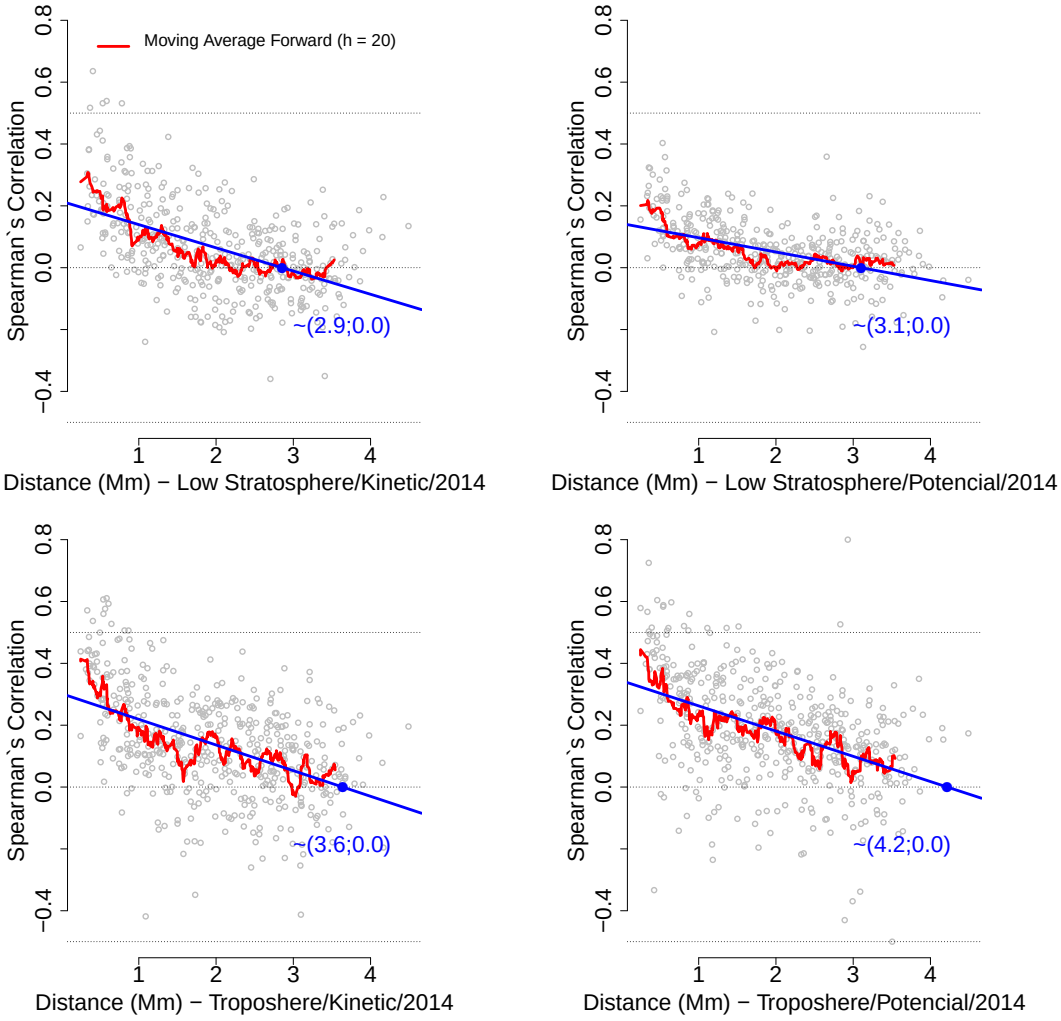

Figure 12. Spearman's correlation coefficient between the kinetic energy (left) and potential energy (right) densities from the total pairwise combinations of aerodromes as a function of the pair distance in the troposphere (bottom) and lower stratosphere (top). The red line is the forward moving average with h = 20 and the blue line is the fitted straight line. The x-axis intercept gives an estimate of the decorrelation distance (see text).

We also computed the correlation between the energy densities at different atmospheric layers, comparing only measurements from the same aerodromes and the same balloon launches. If GWs propagating through the troposphere reaches the lower stratosphere, the correlation coefficients are expected to be non-null and positive. What we observed was that the average value of the correlation coefficients was close to zero. The histogram of Spearman's correlation coefficient of all aerodromes is shown in Figure 13.

The absence of correlation between measurements at different atmospheric layers indicates that typically the GWs propagating through the troposphere below 12 km are

not the cause of the GWs propagating through the lower stratosphere (Allen & Vincent, 1995; Geller & Gong, 2010). That being true, at least in the Brazilian territory, we may rule out the hypothesis that the seeding mechanism of plasma bubbles in the upper atmosphere frequently has its remote cause on perturbations coming from the troposphere below 12 km. However, we should not rule out sporadic events, such as tropospheric deep cloud convection, because it can directly reach and perturb the lower stratosphere (Sivakandan et al., 2019; Takahashi et al., 2020). Also, we do not rule out wind shear mechanisms that occur in the transition region above 12 km, which we consider the most probable source of GWs observed in the lower stratosphere. Some authors, such as Sivakandan *et al* (Sivakandan et al., 2019), consider this a tropospheric perturbation. Using ray tracing methods they concluded that most probably the observed mesospheric GWs were triggered in the troposphere by shear mechanisms. Since the wind shear was evaluated at an altitude range from 1 km to 21 km, it is not clear if the authors were accurate on their definition of troposphere. In other geographic locations, characterized by mountainous relief with high peaks, GWs perturbations can propagate to the lower stratosphere under certain circumstances (C. J. Heale et al., 2020), but such topographical profiles are simply absent in the Brazilian territory. We also counted more monochromatic waves in the lower stratosphere (Figure 14), but this may or may not be related to our previous conclusion.

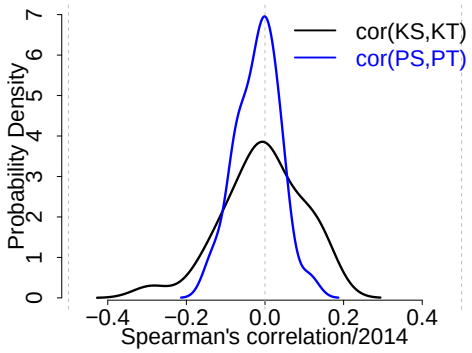

Figure 13. Probability density function of the correlation coefficients between (kinetic - K and potential - P) energy densities in the lower stratosphere (S) and troposphere (T) during 2014.

3.3 Monochromatic GWs

When counting monochromatic GWs, it must be taken into account the fact that the number of radiosonde launches were not uniform in time. Some months had a larger number of launches than others, as shown in the hot tables in Figures B1 and B2, where each line is ordered by geographic latitude (the tables only shown aerodromes with more than 2 GWs identified in 2014).

Figure 14 shows that in the troposphere the count of monochromatic GWs in the dry season was greater than the count in the wet period. This happened probably because of the fewer number of launches in the wet period due to rain, or maybe because of synchronization loss between radiosonde and aerodrome due to bad weather or instrument failure. It was also observed that there was more GWs detected in the middle latitudes than in the equatorial region. On average, the ratio between the count of GWs and launches was less than 35 %.

In the lower stratosphere, the quantity of monochromatic GWs were greater than the same quantity in the troposphere. However, the Figure 14 shows that there were no

trend in the count of GWs in the lower stratosphere, but only what seemed to be a random variation about the mean value. Also, on average, in the lower stratosphere, the ratio between the count of GWs and launches was no greater than 40 %. This different behavior between the troposphere and the lower stratosphere also suggests that there were no correlation between them, corroborating the conclusion that GWs propagating through the troposphere below 12 km are not coupled to GWs in the lower stratosphere. These GWs propagating in the troposphere below 12 km most probably do not reach the lower stratosphere. It probably breaks, get absorbed or reflected before reaching the stratosphere (Nappo, 2003), or it interacts destructively with strong wind streams in the transition region. The GWs observed in the lower stratosphere is probably created in the tropopause where winds are subject to more intense shear.

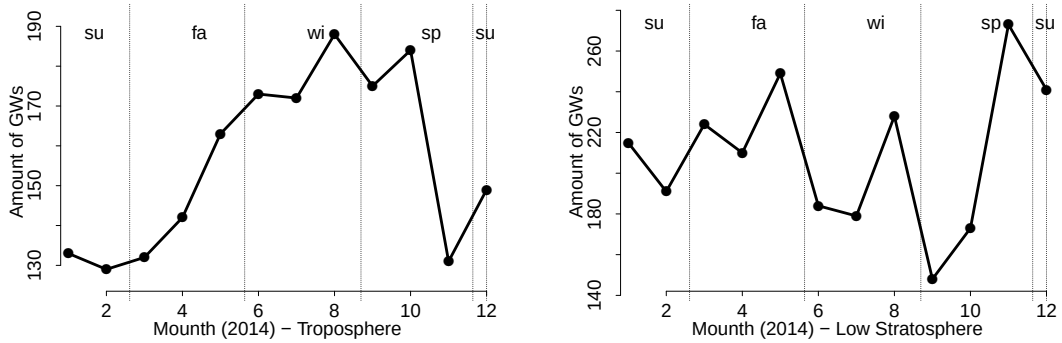

Figure 14. Count of GWs in the troposphere (left) and lower stratosphere (right).

The vertical wavelengths computed for each atmospheric layer and grouped according to day period (dusk/dawn) are shown in Figure 15 as function of time. The wavelength distribution is symmetric, independently of whether it is dawn or dusk, or whether it is the wet or dry season. The wavelength distribution is also independent of the location of the aerodromes (geographic latitude). Considering all the measurements of monochromatic waves in 2014 in the troposphere, the calculated mean values ± standard deviation for the vertical wavelength was (6.07 ± 0.90) km for dawn time and (6.06 ± 0.87) km for dusk time. For the lower stratosphere, the mean values ± standard deviation for the vertical wavelength was (2.87 ± 0.73) km for dawn time and (3.15 ± 0.72) km for dusk time, very similar to the values found by Vincent and Alexander (2000). Hence, the mean vertical wavelength in the lower stratosphere was shorter than the mean vertical wavelength in the troposphere. These average values for the vertical wavelengths, in both layers, agree well with the values reported by other authors (Vincent & Eckermann, 1997; S. Zhang & Yi, 2005).

The values of the ratio $\hat{\omega}/f$ are shown in Figure 16. The distributions have a weak dependence on latitude and season. The median value of this ratio was approximately 2.8 in the wet season and 2.4 in the dry season for the troposphere. But, the median value of this ratio was approximately 2.1 in the wet season and 2.4 and dry season for the low stratosphere. The distribution and typical values are consistent with other results from literature (S. Zhang & Yi, 2005). These results did not show any substantial variation of the ratio with latitude (Geller & Gong, 2010).

Considering the Coriolis's factor f for latitudes greater than 20° and the theory of internal wave propagation in the atmosphere, we estimated the intrinsic wave angular frequency $\hat{\omega}$ (Tsuda et al., 1990; Vincent & Eckermann, 1997; Vicent & Alexander, 2000; Fritts & Alexander, 2003). The computed values are shown in Figure 18. The intrinsic frequencies values are typically less than $3.0{\cdot}10^{-4}/2\pi$ Hz in both layers, but usu-

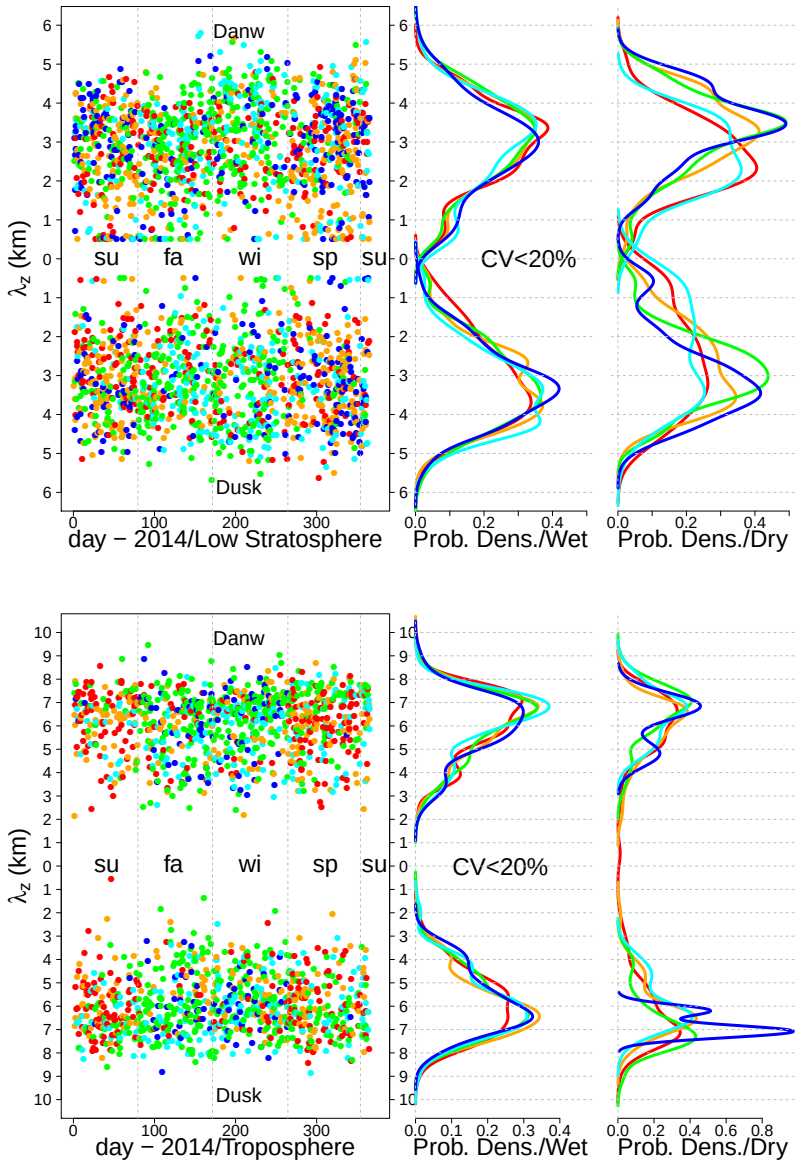

Figure 15. Left: daily variation of the GWs vertical wavelengths with variation coefficient less than 20 % (between zonal wind, meridional wind and temperature) in the troposphere and lower stratosphere in 2014. Right: vertical wavelength probability density discriminated by the cluster to which the measurements belong and season (dry/wet).

ally greater than the frequency of Coriolis. The period will range between 5 h to 17 h ($f_{\hat{\omega}} = 1.0 \cdot 10^{-4}/2\pi$ Hz to $f_{\hat{\omega}} = 3.0 \cdot 10^{-4}/2\pi$ Hz, where the frequency correspond to the first and third quartiles) for latitude greater than 20° in Brazilian territory. In addition, the value of $\hat{\omega}$ increases monotonically with latitude and, conversely, the period of GWs decreases monotonically with latitude. Considering the typical range of intrinsic frequencies and the average values of the vertical wavelength, the vertical velocities of the monochromatic GWs in both layers will typically vary from 9.0×10^{-2} m/s to $2.8{\times}10^{-1}$ m/s (troposphere) and $4.0{\times}10^{-2}$ m/s to $1.4{\times}10^{-1}$ m/s (low stratosphere). These results show that the vertical velocities of GWs in the troposphere are usually greater

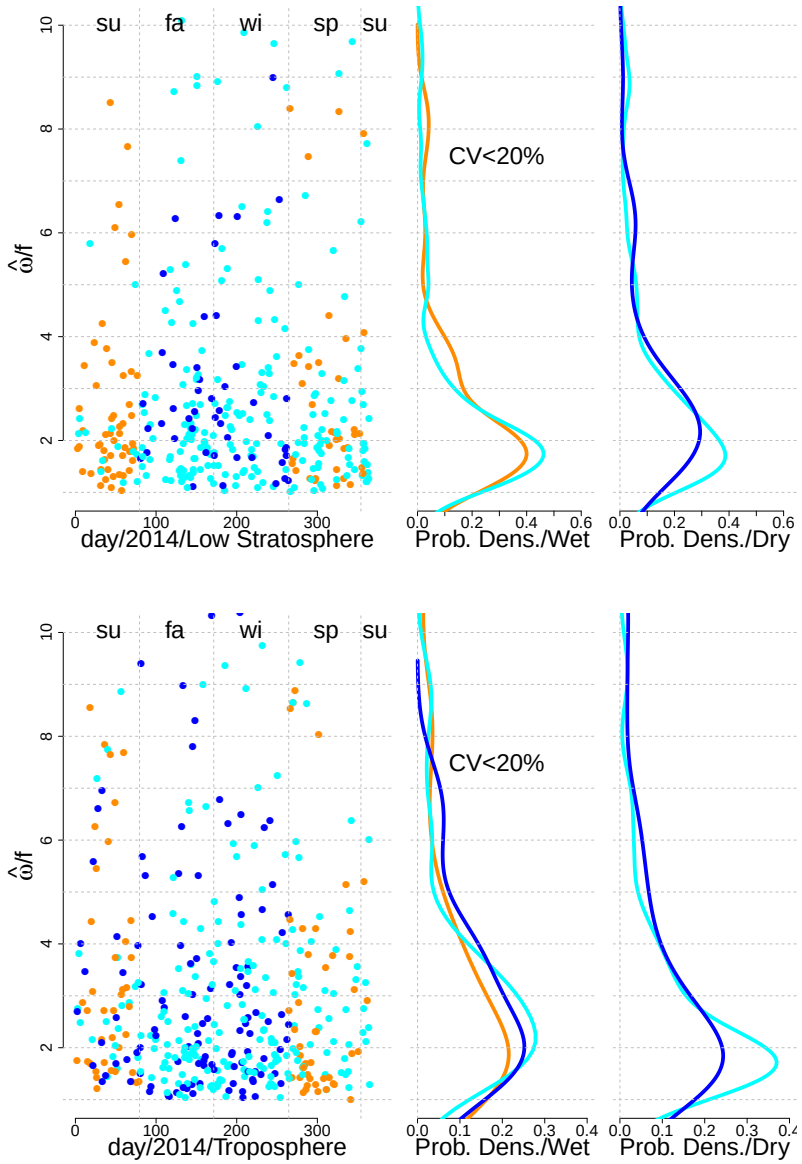

Figure 16. Left: Ratio $\frac{\hat{\omega}}{f}$ of the monochromatic GWs in the troposphere and lower stratosphere during 2014 as a function of time for aerodromes located at latitudes greater than 20°. Right: probability density $\frac{\hat{\omega}}{f}$ discriminated by the cluster to which the measurements belong and season (dry/wet).

than the vertical velocities in the low stratosphere (Vicent & Alexander, 2000). Observations of GWs in the mesosphere above Japan (35°N, 136°E), showed that vertical wavelengths were in the range from 5 to 15 km and that the intrinsic period was about 8.6 h (Tsuda et al., 1990), leading us to conclude that GWs observed much above the low stratosphere have larger vertical wavelengths, but similar periods.

The horizontal wavelength of quasi-monochromatic GWs propagating in the troposphere for aerodromes with latitudes greater than 20° had a median value of 582 km in the wet season and 690 km in the dry season (see Figure 18). In the low stratosphere,

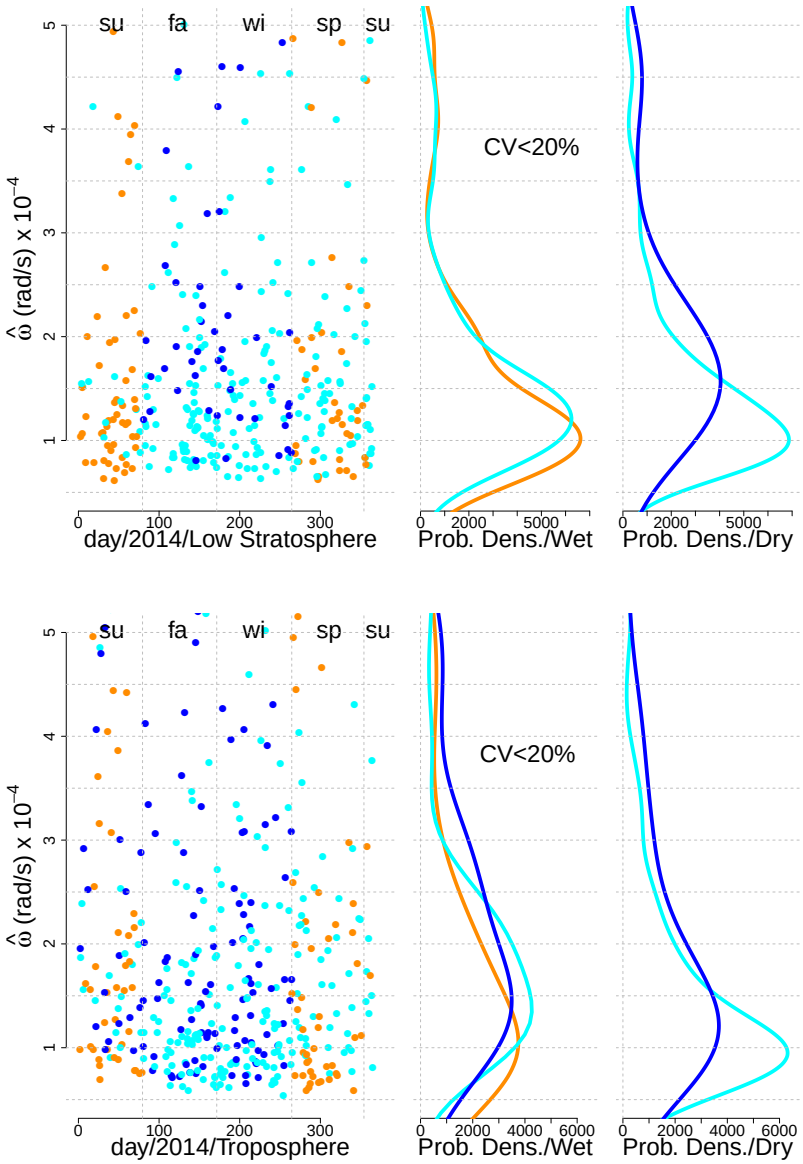

Figure 17. Left: intrinsic angular frequency $\hat{\omega}$ of the GWs in the troposphere and lower stratosphere in 2014 as a function of time for aerodromes located at latitudes greater than 20°. Right: probability density of the intrinsic angular frequency discriminated by the cluster to which the measurements belong and season (dry/wet).

the median values for the horizontal wavelength was 495 km in the wet season and 379 km in the dry season. We did not find any significant difference between the horizontal wavelength from locations at different latitudes in both layers. Using the computed horizontal wavelengths and the wave frequencies $\hat{\omega}$, we computed the wave horizontal velocity. In the troposphere the velocities were in the range $9.2 \times 10^0 - 2.7 \times 10^1$ m/s in the wet season and $1.0 \times 10^1 - 3.2 \times 10^1$ m/s in the dry season. In the low stratosphere, the horizontal velocity was in the range $7.8 \times 10^0 - 2.3 \times 10^1$ m/s in wet season and $6.0 \times 10^0 - 1.8 \times 10^1$ m/s in the dry season.

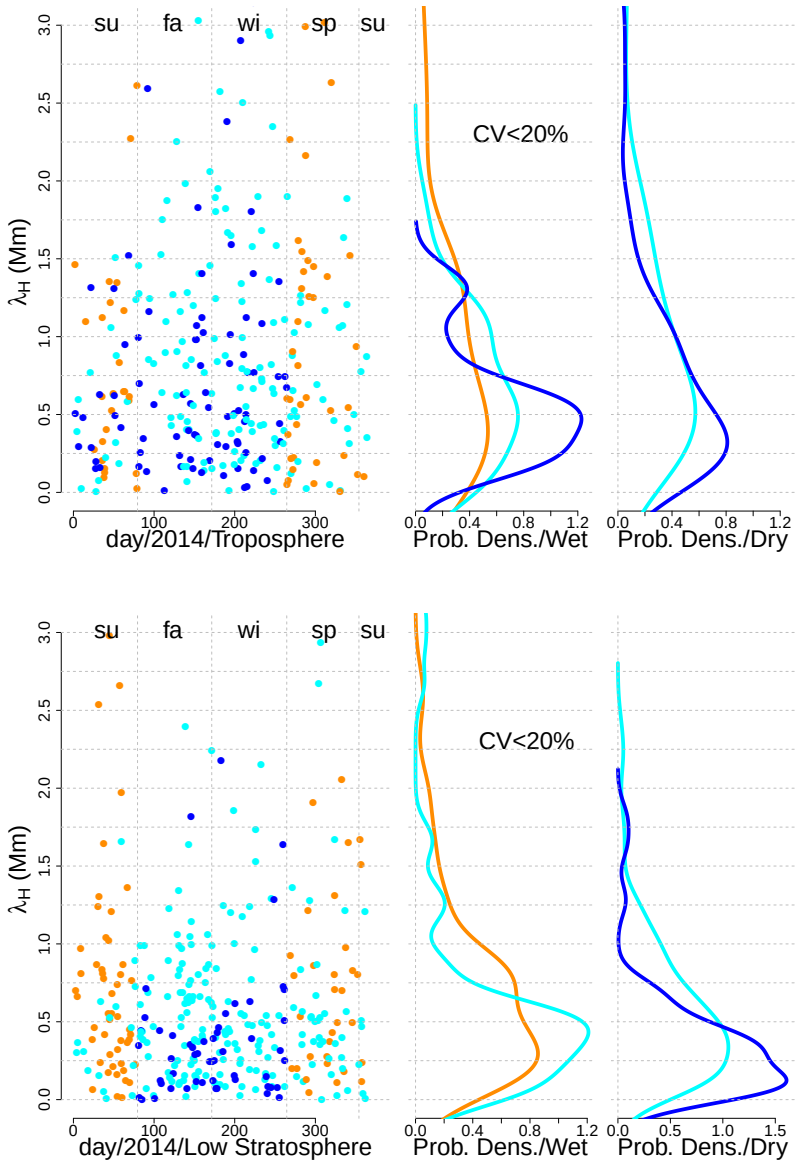

Figure 18. Left: horizontal wavelength λ_H of the GWs in the troposphere and lower stratosphere in 2014 as a function of time for aerodromes located at latitudes greater than 20°. Right: probability density of the horizontal wavelength λ_H discriminated by the cluster to which the measurements belong and season (dry/wet).

Finally, we have taken the values of amplitude, vertical wavelength and phase of the monochromatic GWs and computed the correlation coefficients between the lower stratosphere values and the troposphere values for each aerodrome, as shown in Figure 19. The correlation coefficients are represented in the histogram in Figure 13. Here again all the average correlation coefficients were close to zero, corroborating our previous results.

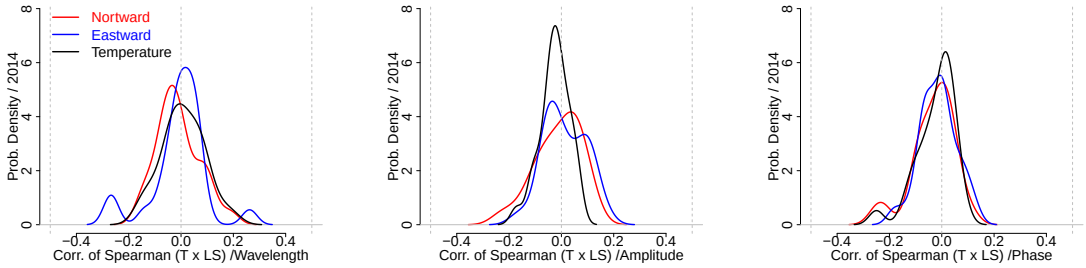

Figure 19. Histograms of Spearman's correlation coefficients between the values of vertical wavelength (left), amplitude (center) and phase (right) of monochromatic GWs in the lower stratosphere and the corresponding parameters in the troposphere.

4 Conclusion

In this paper, we applied a variety of statistical methods to study gravity waves in the troposphere and lower stratosphere in the Brazilian sector, using an unprecedented large database of radiosonde measurements. Some of these techniques were applied for the first time in this context, such as cluster analysis, spatial correlation analysis, gamma distribution fitting, least squares fitting with simultaneous harmonic and parabolic detrending, non-parametric moving central estimators to smooth temporal series and Spearman's correlation.

The average meridional wind profiles were grouped by means of a hierarchical cluster analysis using euclidean distance and ward's link. The cluster analysis identified aerodromes with similar characteristics and demonstrated that the wind profiles typically groups in the same range of latitudes. Therefore, the wind profiles located in the same latitude range usually have similar features. In the troposphere, the wind intensities were northward and weaker near the ground, as expected, and at higher altitudes in the troposphere the winds were typically southward and stronger. In the lower stratosphere, on the other hand, the winds tend to be southward in the lower limit (18 km) and northward at the upper limit (24 km).

By building the hodographs, we were able to compare in detail the wind average profiles in each aerodrome. Using this method, we identified the atmospheric circulation cells, such as the Hardley's cell and the Intertropical Convergence Zone (ITCZ), in the troposphere, and the Brewer-Dobson's circulation cell, in the lower stratosphere. On average, the intensities of the winds in the troposphere were greater in the dry season. This was associated with the observation of an increased GW kinetic energy density in the dry season.

At the top of the lower stratosphere (25 km), the winds were greater near the equator line, probably due to the flux or air from the troposphere to the stratosphere. The values of wind intensities in the lower stratosphere were also greater in the dry season.

The kinetic and potential energy densities were studied using standard temporal series techniques. We dealt with missing data by applying a smooth filter based on robust statistics. In the troposphere, the average values of kinetic and potential energy densities in the dry period were greater than the values in the wet period. Besides that, it was also observed an increase in the volatility of the potential energy density in the troposphere in the dry period. These results suggest that the increased wind intensity in the dry season plays an important role on the GW excitation process in the troposphere.

In the lower stratosphere, the values of the kinetic and potential energy densities were higher than the values in the troposphere. Also, no seasonality in the kinetic and potential energy densities was identified in the lower stratosphere. However, it was observed an increase in the volatility in the kinetic energy density in the lower stratosphere in the dry season. These results are relevant in the context of the seeding problem of ionospheric irregularities such as plasma bubbles. For instance, if gravity waves created at the lower stratosphere are coupled to gravity waves that perturb the bottom ionosphere at much higher altitudes, than there should be no season where such waves are more probable, unless there is some intermittent process that favours its transport to higher altitudes. In other words, our results corroborates the hypothesis that bottom side perturbations in the ionosphere are always there, randomly distributed in time.

The distribution of the energy densities were studied in both atmosphere layers. The distributions had an asymmetric shape and they were better described by a gamma distribution instead of a normal distribution. The higher adherence found using the Kolmogorov-Smirnov's test proved that.

No correlation was found between the kinetic or potential energy densities in the lower stratosphere against the corresponding values in the troposphere. This result suggests that GWs propagating through the troposphere below 12 km are not coupled to GWs in the lower stratosphere. A similar correlation analysis was carried out using the parameters from the monochromatic gravity waves and the same result was found. These results also have an important implication for the seeding problem of ionospheric irregularities in the Brazilian sector: if gravity waves of troposphere/lower stratosphere origin play any role in the initial perturbation, than it is probably created above 12 km by intense wind shear in the transition region, but not in the lower troposphere.

This study also investigated the spatial correlation of the kinetic and potential energy densities at distinct aerodromes. The results showed that the correlation was positive and decreased with the distance between the aerodromes both in the troposphere and lower stratosphere, as expected. The decorrelation distance was computed, yielding a value of around 3,000 km ($\sim 27°$) in the troposphere e around 3,900 km ($\sim 35°$) in the lower stratosphere.

We also studied the characteristics of the monochromatic GWs. The absolute frequency in the troposphere was greater in the dry period, but this should not be automatically interpreted as a result of greater GWs activity, because the samples are not uniform. In the lower stratosphere, no seasonality was found in the counts of GWs.

The vertical wavelength in each layer were normally distributed, independent of time (whether dawn or dusk) and independent of location (aerodrome). In the troposphere the average vertical wavelength was (6.07 $\pm$ 0.90) km in the dawn and (6.06 $\pm$ 0.87) km in the dusk. In the lower stratosphere the average vertical wavelength was (2.87 $\pm$ 0.73) km in the dawn and (3.15 $\pm$ 0.72) km in the dusk time.

From the hodographs of the fitted monochromatic waves, it was possible to estimate the intrinsic frequency of each wave. In the Brazilian territory with latitude greater than 20° theses values were distributed in the interval $1.0 \times 10^{-4} - 3.0 \times 10^{-4}$ rad/s. Considering the typical range of intrinsic frequencies and the average values of the vertical wavelength, the vertical velocities of GWs in both layers will typically vary in the range from $9.0{\times}10^{-2}$ m/s to $2.8{\times}10^{-1}$ m/s (troposphere) and $4.0{\times}10^{-2}$ m/s to $1.4{\times}10^{-1}$ m/s (low stratosphere). These results show that the vertical velocities of GWs in the troposphere are usually greater than the vertical velocities in the low stratosphere

The horizontal wavelength of quasi-monochromatic GWs propagating in the troposphere for aerodromes with latitudes greater than 20° had a median value of 582 km in the wet season and 690 km in the dry season (see Figure 18). In the low stratosphere, the median values for the horizontal wavelength was 495 km in the wet season and 379 km in the dry season. In the troposphere the horizontal velocities were in the range $9.2{\times}10^{0} - 2.7 \times 10^{1}$ m/s in the wet season and $1.0 \times 10^{1} - 3.2 \times 10^{1}$ m/s in the dry season. In the low stratosphere, the horizontal velocity was in the range $7.8 \times 10^{0} - 2.3 \times 10^{1}$ m/s in wet season and $6.0 \times 10^{0} - 1.8 \times 10^{1}$ m/s in the dry season.

Finally, we calculated the correlation coefficients of the amplitude, vertical wavelength and phase in the lower stratosphere against the respective values in the troposphere. No significant correlation was found between these variables. These results also lead us to the conclusion that GWs in the troposphere below 12 km were not coupled to the GWs above the tropopause in the Brazilian sector. Therefore, the analysis resulting from the energy density measurements and the analysis resulting from the parameters of the monochromatic waves are consistent and lead us to the same conclusion.

Appendix A Aerodromes

Table A1. Information of aerodromos controled by ICEA during 2014.

	Aerodrome	City	UF	Latitude (°)	Longitude (°)	Altitude (m)	Region
1	sbat	ALTA FLORESTA	MT	-9.87	-56.10	289	CO
2	sbbr	BRASÍLIA	DF	-15.87	-47.92	1066	CO
3	sbbv	BOA VISTA	RR	2.84	-60.69	84	N
4	sbcf	CONFINS	MG	-19.62	-43.97	827	SE
5	sbcg	CAMPO GRANDE	MS	-20.47	-54.67	559	CO
6	sbcr	CORUMBÁ	MS	-19.01	-57.67	141	CO
7	sbct	CURITIBA	PR	-25.53	-49.18	911	S
8	sbcy	VÁRZEA GRANDE	MT	-15.65	-56.12	188	CO
9	sbcz	CRUZEIRO DO SUL	AC	-7.60	-72.77	194	N
10	sbfi	FOZ DO IGUAÇU	PR	-25.60	-54.48	240	S
11	sbfl	FLORIANÓPOLIS	SC	-27.67	-48.55	5	S
12	sbfn	FERNANDO DE NORONHA	PE	-3.85	-32.43	58	NE
13	sbgl	RIO DE JANEIRO	RJ	-22.81	-43.25	9	SE
14	sblo	LONDRINA	PR	-23.33	-51.14	569	S
15	sbmn	MANAUS	AM	-3.04	-60.05	80	N
16	sbmq	MACAPÁ	AP	0.05	-51.07	17	N
17	sbmt	SÃO PAULO	SP	-23.51	-46.63	722	SE
18	sbmy	MANICORÉ	AM	-5.82	-61.28	53	N
19	sbnt	NATAL	RN	-5.90	-35.23	52	NE
20	sbpa	PORTO ALEGRE	RS	-29.99	-51.17	4	S
21	sbpv	PORTO VELHO	RO	-8.71	-63.90	88	N
22	sbrb	RIO BRANCO	AC	-9.87	-67.90	193	N
23	sbsl	SÃO LUÍS	MA	-2.59	-44.24	54	NE
24	sbsm	SANTA MARIA	RS	-29.71	-53.69	88	S
25	sbsn	SANTARÉM	PA	-2.42	-54.79	60	N
26	sbts	ÓBIDOS	PA	-2.22	-55.93	344	N
27	sbtt	TABATINGA	AM	-4.25	-69.94	85	N
28	sbua	SÃO GABRIEL DA CACHOEIRA	AM	-0.15	-66.99	76	N
29	sbug	URUGUAIANA	RS	-29.78	-57.04	78	S
30	sbul	UBERLÂNDIA	MG	-18.88	-48.23	943	SE
31	sbvh	VILHENA	RO	-12.69	-60.10	615	N
32	sbvt	VITÓRIA	ES	-20.26	-40.29	3	SE

Appendix B Hot tables showing the count of GWs in each aerodrome

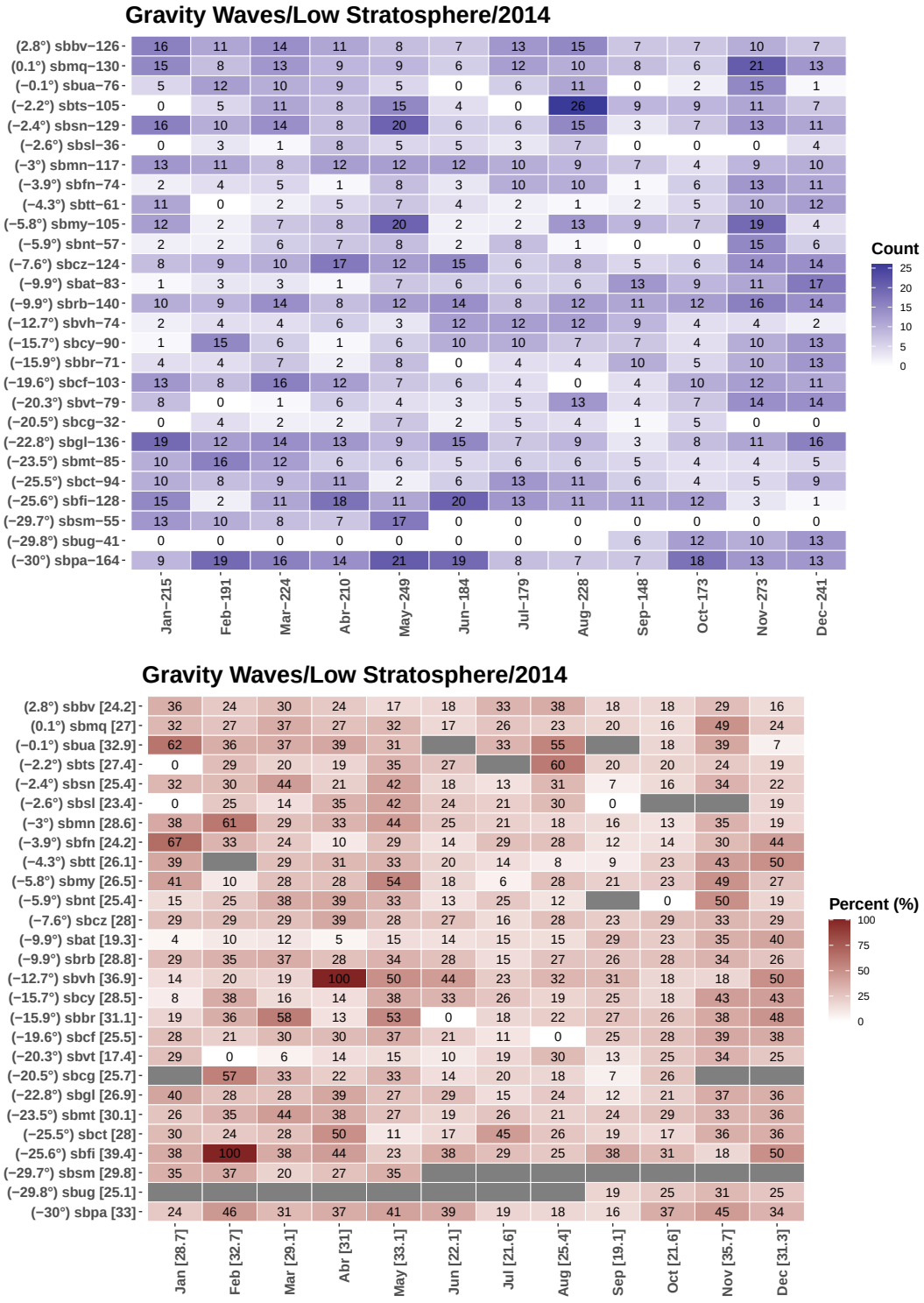

Figure B1. Monthly counts of GWs (top) in the lower stratosphere in 2014 and ratio between the counts and the number of radiosonde launches (botton). The rows correspond to aerodromes ordered by geographic latitude. Values between [ ] mean average values by line and column.

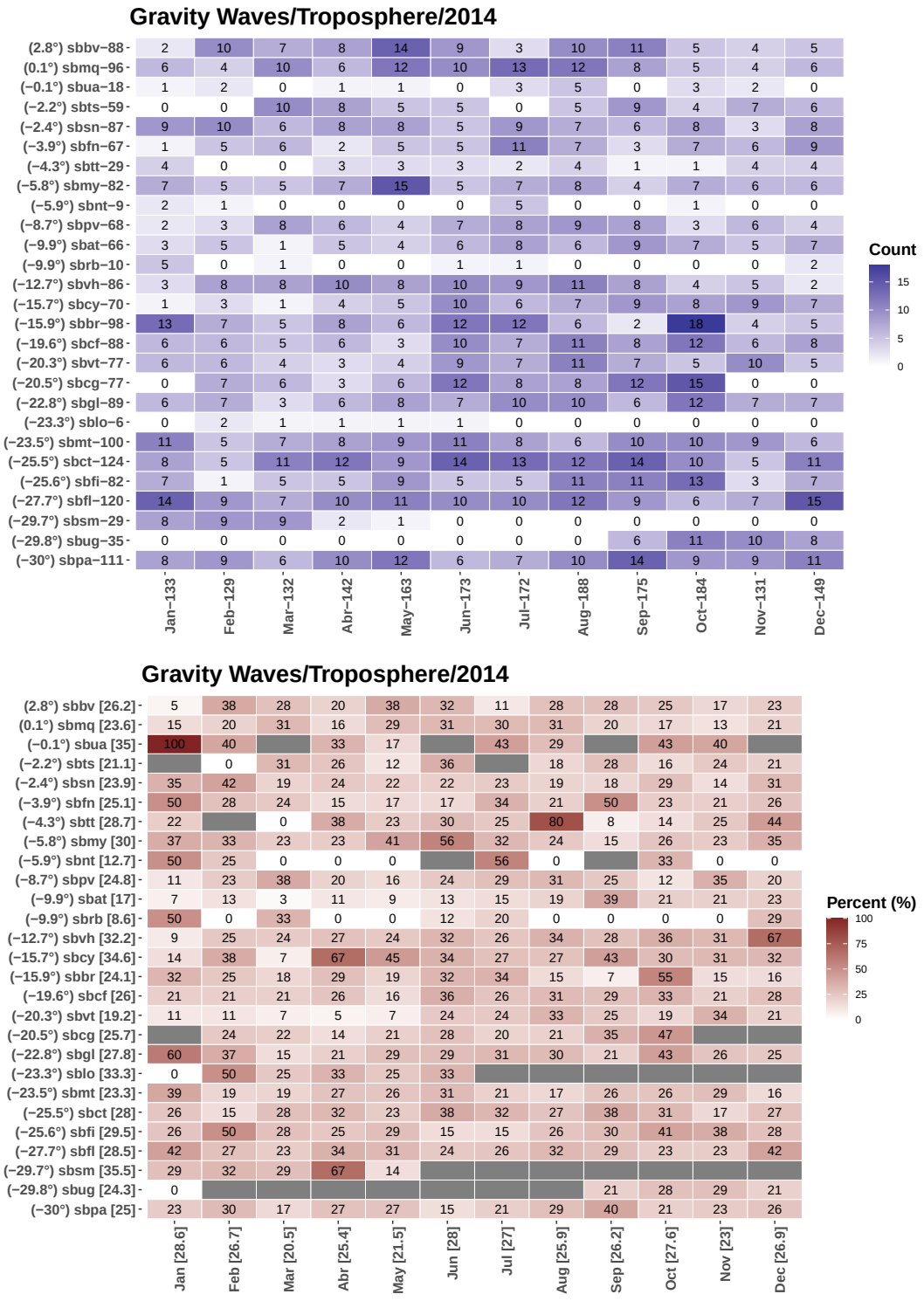

Figure B2. Monthly counts of GWs (top) in the troposphere in 2014 and ratio between the counts and the number of radiosonde launches (botton). The rows correspond to aerodromes ordered by geographic latitude. Values between [ ] mean average values by line and column.

Acknowledgments

The authors would like to thank the Instituto de Controle do Espaço Aéreo (ICEA) for the data provided to carry out this research. Also, thanks for Federal Institute of Amazonas (IFAM), Fundação de Amparo à Pesquisa do Estado do Amazonas (FAPEAM) and Aeronautics Institute of Technology (ITA) for support in this research. This research has been partially supported by project 16/24970-7 by FAPESP (Fundação de Amparo à Pesquisa do Estado de São Paulo).

References

Ahrens, C., & Henson, R. (2018). *Meteorology today, an introduction to weather, climate, and the environment* (12th ed.). Cengage.

Alexander, M. J., Geller, M., McLandress, C., Polavarapu, S., Preusse, P., Sassi, F., ... Watanabe, S. (2010). Recent developments in gravity-wave effects in climate models and the global distribution of gravity-wave momentum flux from observations and models. *Royal Meteorological Society*, *136*(650), 1103-1124. doi: https://doi.org/10.1002/qj.637

Allen, S., & Vincent, R. (1995). Gravity wave activity in the low atmosphere: seasonal and latitudinal variations. *Jornal of Geophysical Research*, *100*, 1327–1350. doi: 10.1029/94JD02688

Arce, G. (2005). *Nonlinear signal processing: A statistical approach* (1st ed.). Wiley.

Archer, C., & Caldeira, K. (2008). Historical trends in the jet streams. *Geophysical Research Letters*, *35*(8). doi: 10.1029/2008gl033614

Azeem, I., Yue, J., Hoffmann, L., Miller, S., Straka III, W., & Crowley, G. (2015). Multisensor profiling of a concentric gravity wave event propagating from the troposphere to the ionosphere. *Geophysical Research Letters*, *42*, 7874–7880. doi: 10.1002/2015GL065903

Bagdonavicius, V., Kruopis, J., & Nikulin, M. (2011). *Non-parametric test for complete data* (1st ed.). Wiley.

Bishara, A., & Hittner, J. (2012). Testing the significance of a correlation with nonnormal data: Comparison of pearson, spearman, transformation, and resampling approaches. *Psychological Methods*, *17*(3). doi: 10.1037/a0028087

Brasil. (2013). Procedimentos operacionais referentes ao lançamento de balão meteorológico [Computer software manual].

Brasil. (2017). Coordenação met/ats referente ao lançamento de balão meteorológico [Computer software manual]. `https://publicacoes.decea.mil.br/publicacao/circea-63-3`.

Brasil. (2020). Manual de meteorologia e oceanografia de defesa [Computer software manual]. `https://www.gov.br/defesa/pt-br/arquivos/legislacao/emcfa/publicacoes/inteligencia/mda_32a_ma_04a_manuala_completo.pdf`.

Brewer, A. (1949). Evidence for a world circulation provided by the measurements of helium and water vapour distribuition in the stratosphere. *Quarterly Journal of the Royal Meteorological Society*, *75*(326). doi: 10.1002/qj.49707532603

Brummelen, G. (2013). *Heavenly mathematics: The forgotten art of spherical trigonometry* (1st ed.). Princeton University Press.

Butchart, N. (2014). The brewer-dobson circulation. *Reviwer of Geophysics*(52). doi: 10.1002/2013RG000448

Cowperwait, P., & Metcalfe, A. (2009). *Introductory time series with r* (1st ed.). Springer.

Devore, J. (2016). *Probability and statistics: for engineering and the sciences* (9th ed.). Cengage.

Fritts, D., & Alexander, M. (2003). Gravity wave dynamics and effects in the middle atmosphere. *Reviews of Geophysics*, *41*, 1–64. doi: 10.1029/2001RG000106

Geller, M., & Gong, J. (2010). Gravity wave kinetic, potential, and vertical fluctuation energies as indicators of different frequency gravity waves. *Journal of Geophysical Research*, *115*(D11111). doi: 10.1029/2009JD012266

Gibbons, J., & Chakraborti, S. (2011). *Nonparametric statistical inference* (5th ed.). CRC Press.

Gossard, E., & Hooke, W. (1975). *Waves in the atmosphere* (1st ed.). Elsevier.

Gregorius, G. (2009). *Stock market volatility* (1st ed.). CRC Press.

Hair, J., Black, W., Babin, B., Anderson, R., & Tathan, R. (2006). *Multivariate data analysis* (6th ed.). Pearson.

Heale, C., Bossert, K., Vadas, S., Hoffmann, L., Dörnbrack, A., Stober, G., ... Jacobi, A. (2020). Secondary gravity waves generated by breaking mountain waves over europe. *JGR: Atmosphere*, *125*(5). doi: 10.1029/2019JD031662

Heale, C. J., Bossert, K., Vadas, S., Hoffmann, L., Dörnbrack, A., Stober, G., ... Jacobi, C. (2020). Secondary gravity waves generated by breaking mountain waves over europe. *Journal of Geophysical Research: Atmospheres*, *125*(5), e2019JD031662.

Huang, C., Helmboldt, J., Park, J., Pedersen, T., & Willermann, R. (2019). Ionospheric detection of explosive events. *Reviews of Geophysics*, *57*, 78–105. doi: 10.1029/2017RG000594

Ibge. (2022). Retrieved from `https://www.ibge.gov.br/geociencias/organizacao-do-territorio/divisao-regional/15778-divisoes-regionais-do-brasil.html?=&t=o-que-e`

Kanji, G. (2006). *100 statistical tests* (3rd ed.). Sage Publication.

Kaufman, L., & Rousseeuw, P. (2005). *Finding groups in data: An introduction to cluster analysis* (1st ed.). Wiley.

Kherani, E., Abdu, M., Paula, E., Fritts, D., Sobral, J., & Meneses Jr, F. (2009). The impact of gravity waves rising from convection in the lower atmosphere on the generation and nonlinear evolution of equatorial bublble. *Annales Geophisicae*, *27*, 1657–1668. doi: 10.5194/angeo-27-1657-2009

Lu, J., & Vecchi, G. (2015). Tropical meteorology & climate — hadley circulation. In G. R. North, J. Pyle, & F. Zhang (Eds.), *Encyclopedia of atmospheric sciences (second edition)* (Second Edition ed., p. 113-120). Oxford: Academic Press. Retrieved from `https://www.sciencedirect.com/science/article/pii/B9780123822253001614` doi: https://doi.org/10.1016/B978-0-12-382225-3.00161-4

Martinson, D. (2018). *Quantitative methods of data analysis for the physical science and engineering* (1st ed.). Cambridge University Press.

Mastrantonio, G., Einaudi, F., Fua, D., & Lalas, D. (1976). Generation of gravity waves by jet streams in the atmosphere. *Journal of Atmospheric Sciences*, *33*(9). doi: 10.1175/1520-0469(1976)033⟨1730:GOGWBJ⟩2.0.CO;2

Nappo, C. (2003). *An introduction to atmospheric gravity waves* (2nd ed.). Elsevier: Academic press.

Oliveira, A., Cazuza, E., Medeiros Neto, J., Silva Junior, J., Barbosa, A., Borba, A., ... Alcântara, M. (2016). Ondas de gravidade na estratosfera equatorial brasileira: estudo de caso. *Holos*, *8*(32), 24–35. doi: 10.15628/holos.2016.4638

Pandove, D., Goel, S., & Rani, R. (2018). General correlation coefficient based agglomerative clustering. *Cluster Computing*, *22*, 553–583. doi: 10.1007/s10586-018-2863-y

Press, W., Teukolsky, S., Vetterling, W., & Flannery, B. (2007). *Numerical recipes: The art of scientific computing* (3rd ed.). Cambridge.

Rossby, C., & Willet, H. (1948). The circulation of the upper troposphere and lower stratosphere. *Science*, *108*(2815). doi: 10.1126/science.108.2815.643

Salby, M., & Callaghan, P. (2005). Interaction between the brewer-dobson circulation and the hardley circulation. *Journal of Climate*, *18*(20). doi: 10.1175/jcli3509.1

Sinclair, E. (2013). *Volatility trading* (2nd ed.). Wiley.

Sivakandan, M., Paulino, I., Ramkumar, T., Taori, A., Patra, A., Sripathi, S., ... Bilibio, A. (2019). Multi-instrument investigation of troposphere-ionosphere coupling and the role of gravity waves in the formation of equatorial plasma bubble. *J. of Atmospheric and Solar-Terrestrial Physics*, *189*, 65–79. doi: 10.1016/j.jastp.2019.04.006

Stull, R. (1988). *An introduction to boundary layer meteorology* (1st ed.). Kluwer.

Takahashi, H., Wrasse, C., Figueiredo, C., Barros, D., Paulino, I., Essien, P., ... Shiokawa, K. (2020). Equatorial plasma bubble occurrence under propagation of mstid and mlt gravity waves. *Journal of Geophysical Research: Space Physics*, *125*(9), e2019JA027566.

Tsuda, T., Kato, T., Yokoi, T., Inoue, T., Yamamoto, M., VanZant, T., ... Sato, T. (1990). Gravity waves in the mesophere observed with the middle and upper atmosphere radar. *Radio Science*, *26*(5), 1005–1018. doi: 10.1029/RS025i005p01005

Vadas, S., Fritts, D., & Alexander, M. (2003). Mechanism for the generation of secondary waves in wave breaking regions. *Jornal of the Atmospheric Science*, *60*, 194–214. doi: 10.1175/1520-0469(2003)060⟨0194:MFTGOS⟩2.0.CO;2

Vicent, R., & Alexander, M. (2000). Gravity waves in the tropical lower stratosphere: An observational study of season and interannual variability. *J. of Geophysical Research*, *105*, 17971–17982. doi: 10.1029/2000JD900197

Vincent, R., & Eckermann, S. (1997). Gravity-wave parameters in the low stratosphere. In K. Hamilton (Ed.), *Gravity wave processes: Their parameterization in global climate models* (pp. 7–25). Springer. doi: 10.1007/978-3-642-60654-0_2

WMO. (2018). *Guide to instruments and methods of observation* (Vol. 1) (No. 8). Author.

Yigit, E. (2015). *Atmospheric and space science: Neutral atmospheres* (1st ed.). Springer.

Yigit, E., & Medvedev, A. (2015). Internal wave coupling process in earth's atmosphere. *Advances in Space Research*, *55*, 983–1003. doi: 10.1016/j.asr.2014.11.020

Youshiki, M., & Sato, K. (2000). A statistical study of gravity waves in the polar regions based on operation radiosonde data. *J. Geophysical Research*, *105*(D14), 17995–18011. doi: 10.1029/2000JD900204

Zhang, S., & Yi, F. (2005). A statistical study of gravity waves from radiosonde observation at wuhan (30° n, 114° e) china. *Annales Geophisicae*, *23*, 665–673. doi: 10.5194/angeo-23-665-2005

Zhang, Y., Xiong, J., Liu, L., & Wan, W. (2012). A global morphology of gravity wave activity in the stratosphere revealed by the 8-year saber/timed data. *J. Geophysical Research*, *117*(D21101), 1–13. doi: 10.1029/2012JD017676

Zink, F., & Vicent, R. (2001). Wavelet analysis of stratospheric gravity wave packets over macquarine island. *J. Geophysical Research*, *106*(D10), 10275–10288. doi: 10.1029/2000JD900846

Figure.

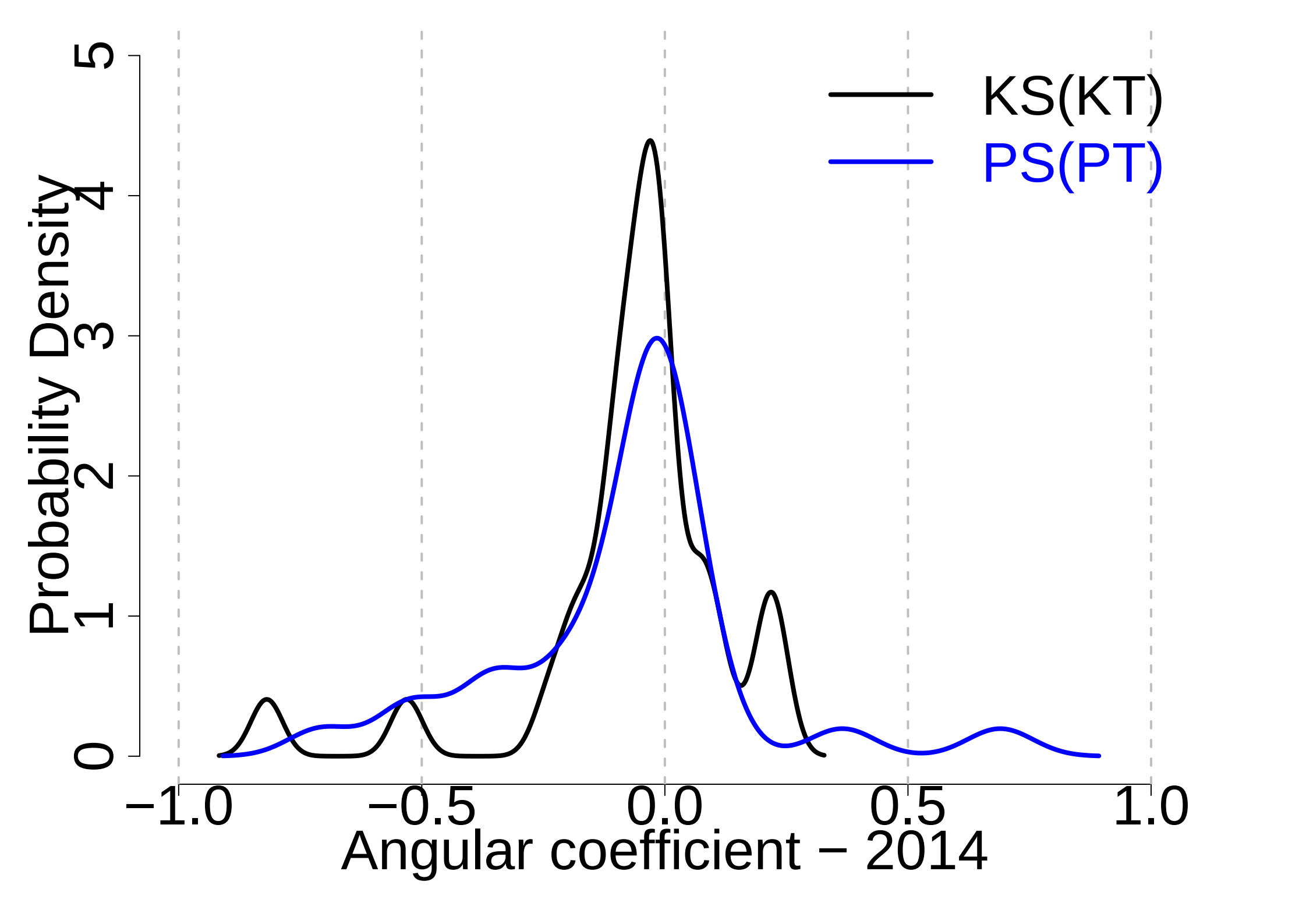
KS(KT)
PS(PT)
Probability Density
0
1
2
3
4
5
−1.0
−0.5
0.0
0.5
1.0
Angular coefficient − 2014

Figure.

Voltar ao relatório | **GRUPO, LATITUDE E LONGITUDE**

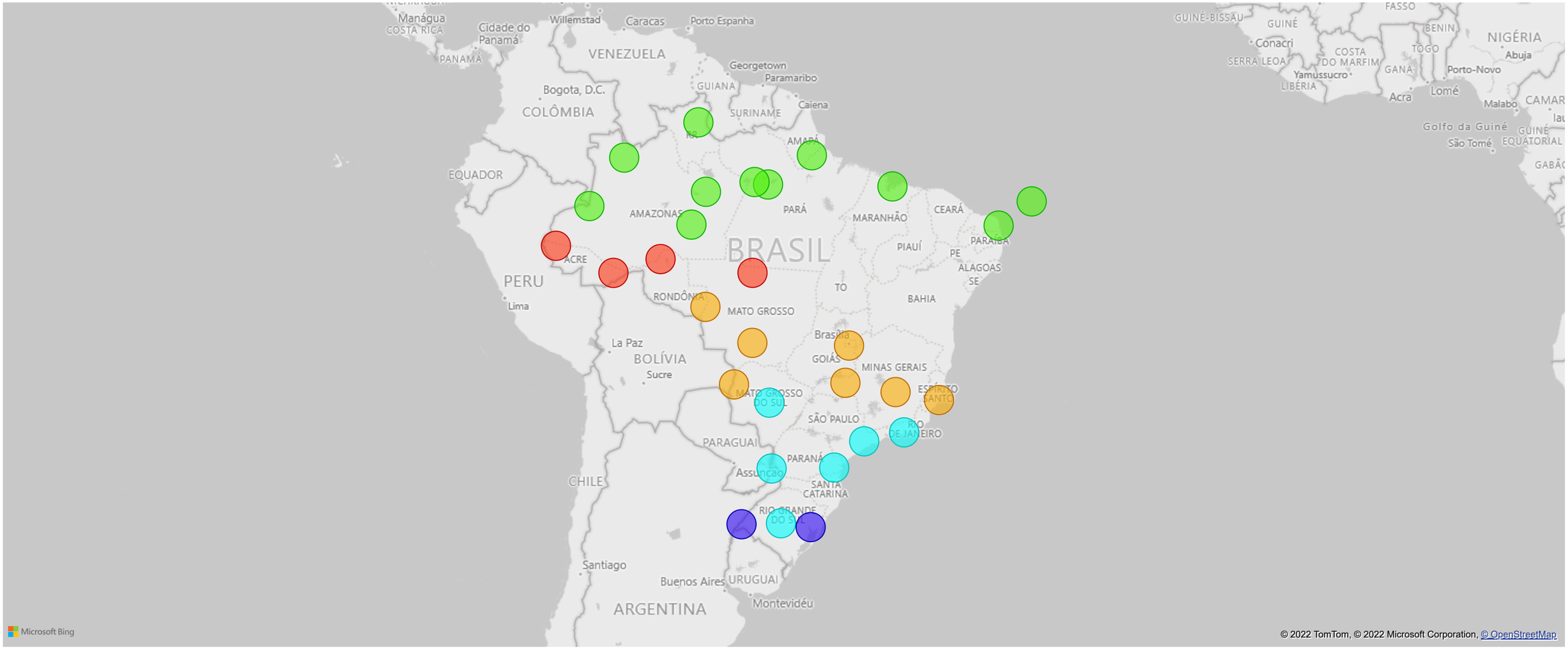

Clusters 1 2 3 4 5

Figure.

Voltar ao relatório | **GRUPO, LATITUDE E LONGITUDE**

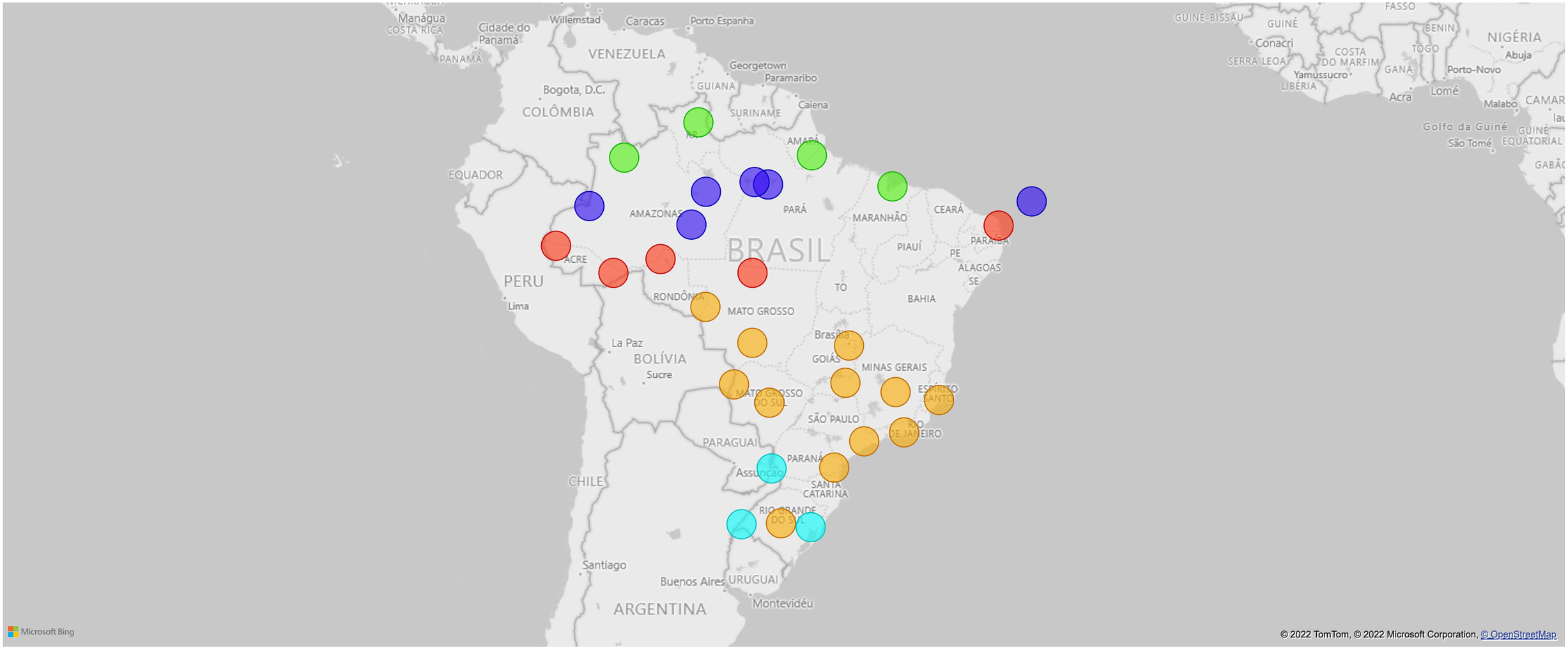

Clusters 1 2 3 4 5

Figure.

Voltar ao relatório | **GRUPO, LATITUDE E LONGITUDE**

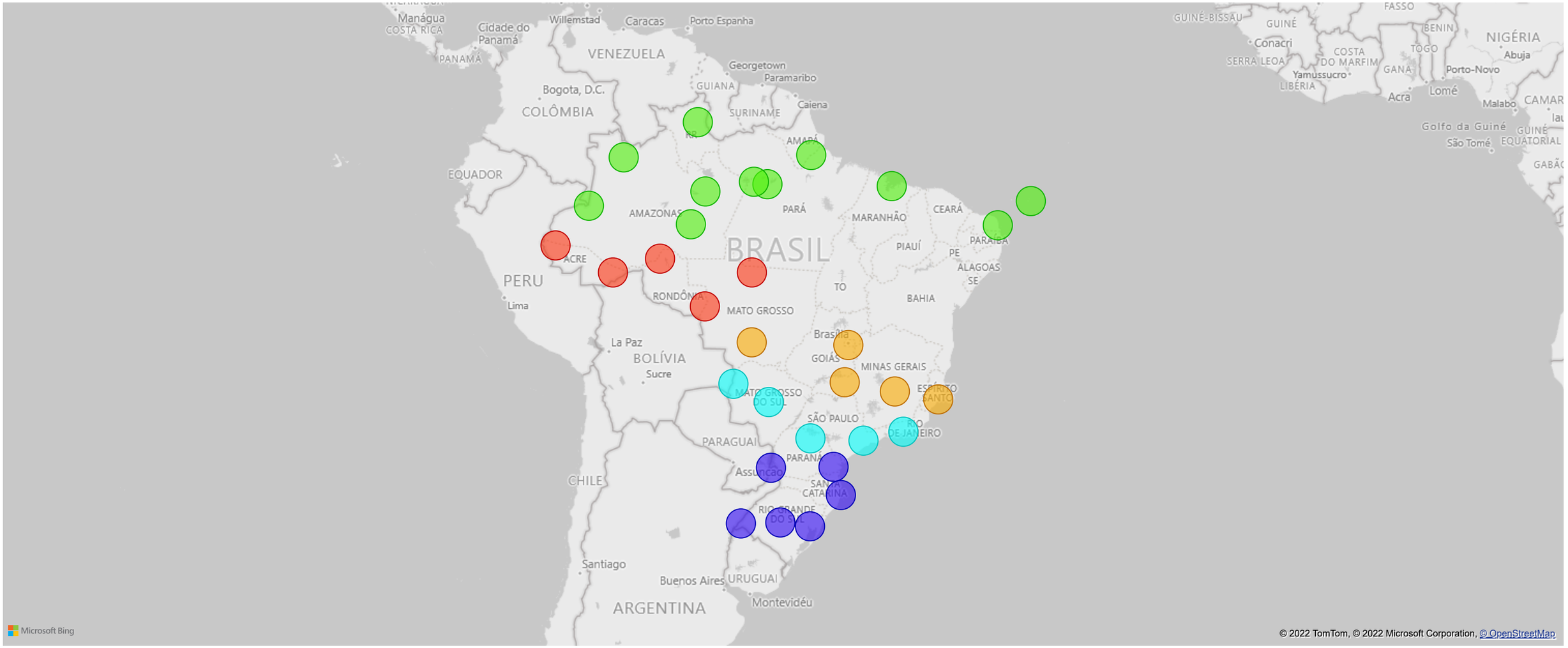

Clusters 1 2 3 4 5

Figure.

Voltar ao relatório | **GRUPO, LATITUDE E LONGITUDE**

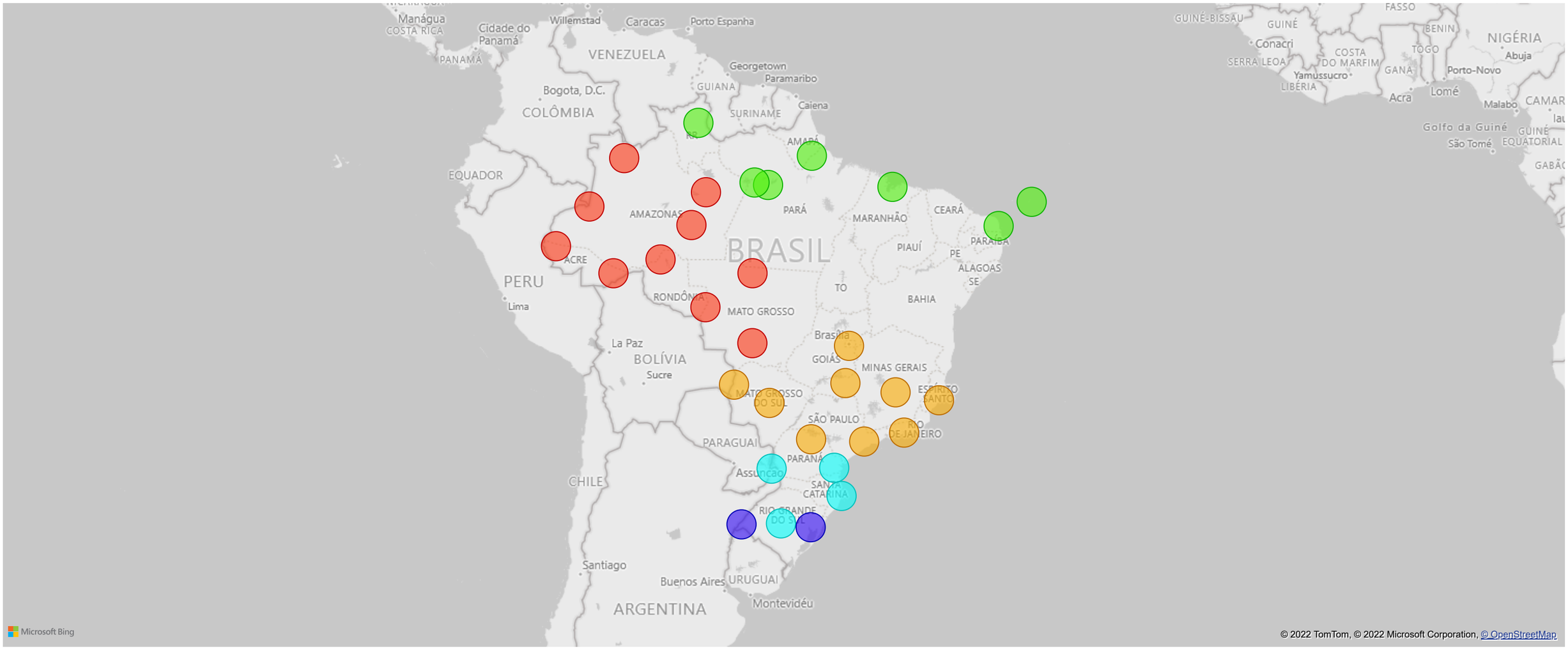

Clusters 1 2 3 4 5

Figure.

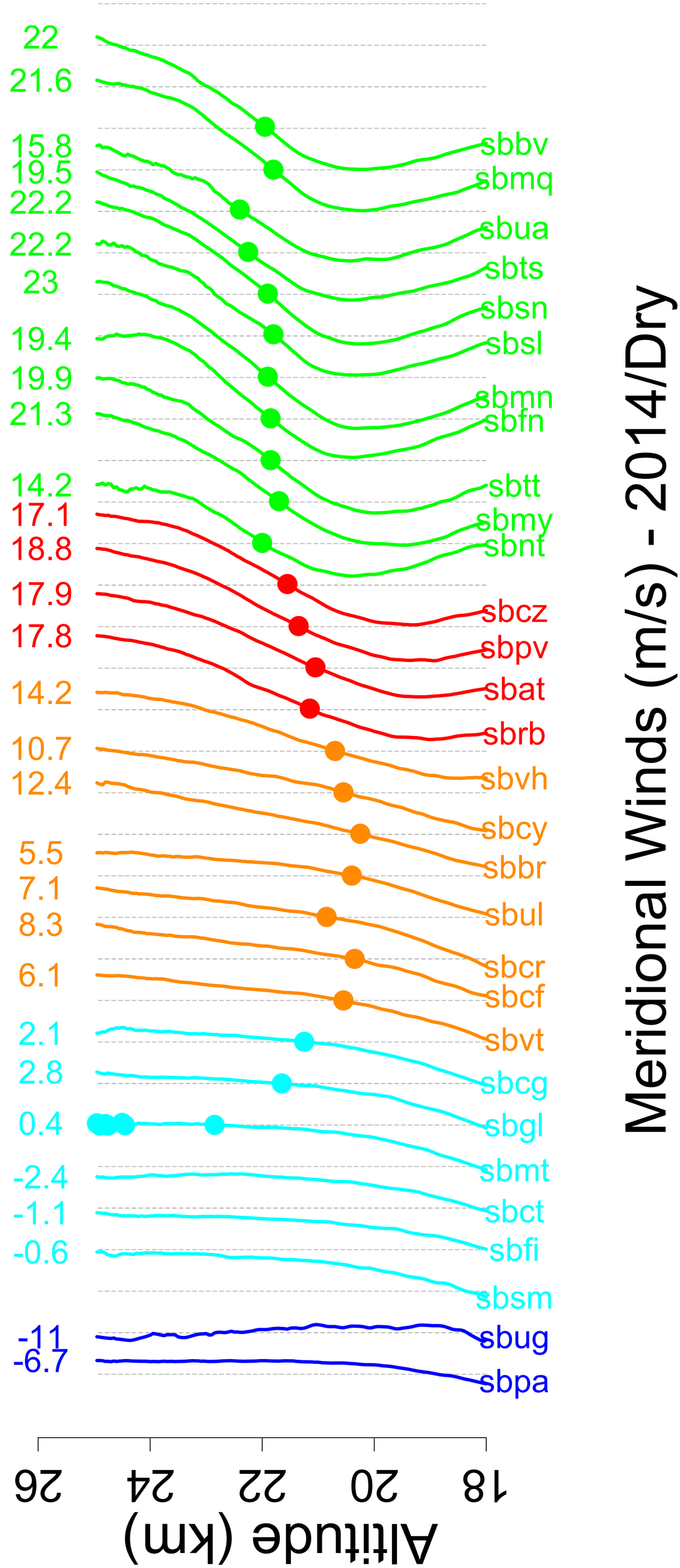
22
21.6
15.8
19.5
22.2
22.2
23
19.4
19.9
21.3
14.2
17.1
18.8
17.9
17.8
14.2
10.7
12.4
5.5
7.1
8.3
6.1
2.1
2.8
0.4
-2.4
-1.1
-0.6
-11
-6.7
sbbv
sbmq
sbua
sbts
sbsn
sbsl
sbmn
sbfn
sbtt
sbmy
sbnt
sbcz
sbpv
sbat
sbrb
sbvh
sbcy
sbbr
sbul
sbcr
sbcf
sbvt
sbcg
sbgl
sbmt
sbct
sbfi
sbsm
sbug
sbpa
26
24
22
20
18
Altitude (km)
Meridional Winds (m/s) - 2014/Dry

Figure.

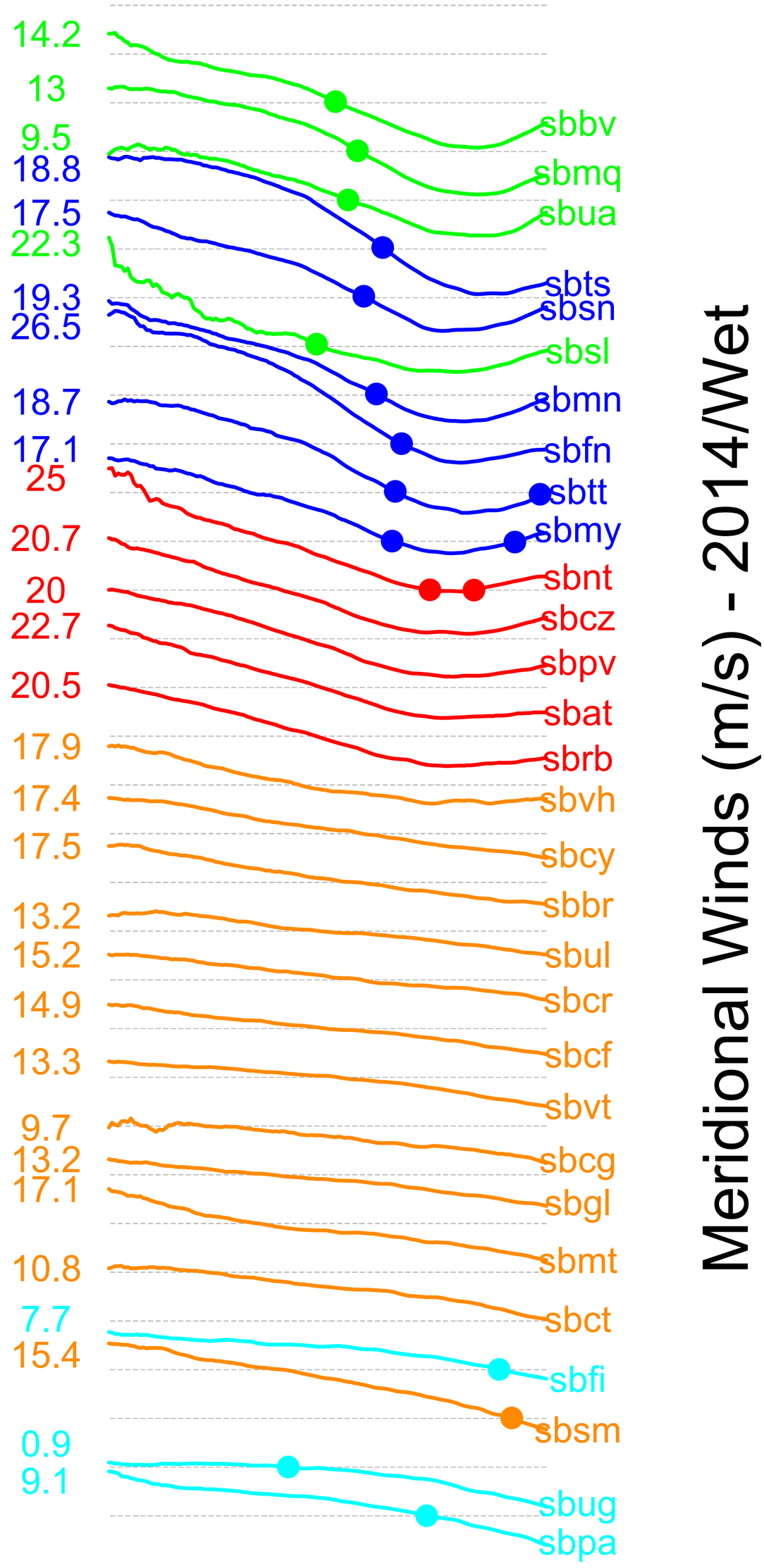
14.2
13
9.5
18.8
17.5
22.3
19.3
26.5
18.7
17.1
25
20.7
20
22.7
20.5
17.9
17.4
17.5
13.2
15.2
14.9
13.3
9.7
13.2
17.1
10.8
7.7
15.4
0.9
9.1
sbbv
sbmq
sbua
sbts
sbsn
sbsl
sbmn
sbfn
sbtt
sbmy
sbnt
sbcz
sbpv
sbat
sbrb
sbvh
sbcy
sbbr
sbul
sbcr
sbcf
sbvt
sbcg
sbgl
sbmt
sbct
sbfi
sbsm
sbug
sbpa
26
24
22
20
18
Altitude (km)
Meridional Winds (m/s) - 2014/Wet

Figure.

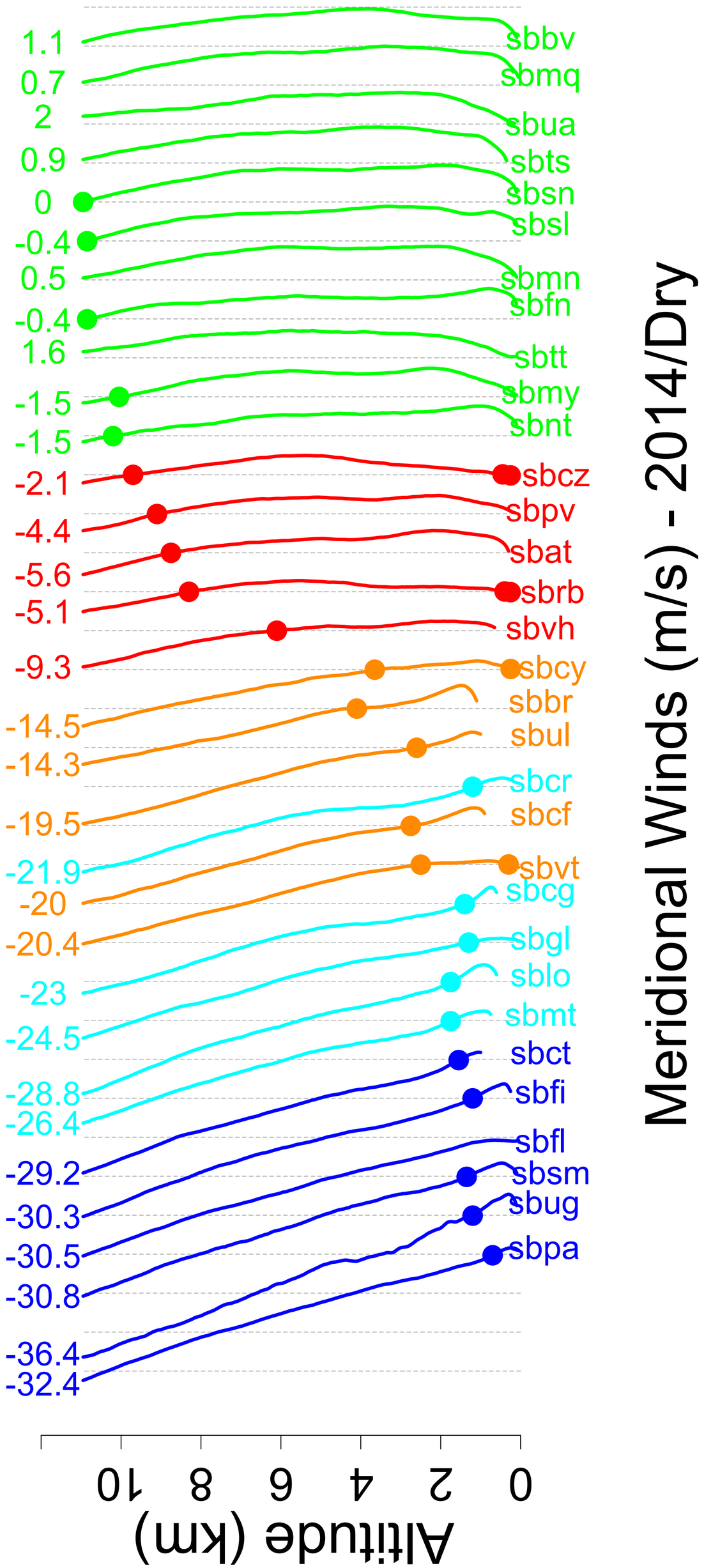
1.1
0.7
2
0.9
0
-0.4
0.5
-0.4
1.6
-1.5
-1.5
-2.1
-4.4
-5.6
-5.1
-9.3
-14.5
-14.3
-19.5
-21.9
-20
-20.4
-23
-24.5
-28.8
-26.4
-29.2
-30.3
-30.5
-30.8
-36.4
-32.4
sbbv
sbmq
sbua
sbts
sbsn
sbsl
sbmn
sbfn
sbtt
sbmy
sbnt
sbcz
sbpv
sbat
sbrb
sbvh
sbcy
sbbr
sbul
sbcr
sbcf
sbvt
sbcg
sbgl
sblo
sbmt
sbct
sbfi
sbfl
sbsm
sbug
sbpa
0
2
4
6
8
10
Altitude (km)
Meridional Winds (m/s) - 2014/Dry

Figure.

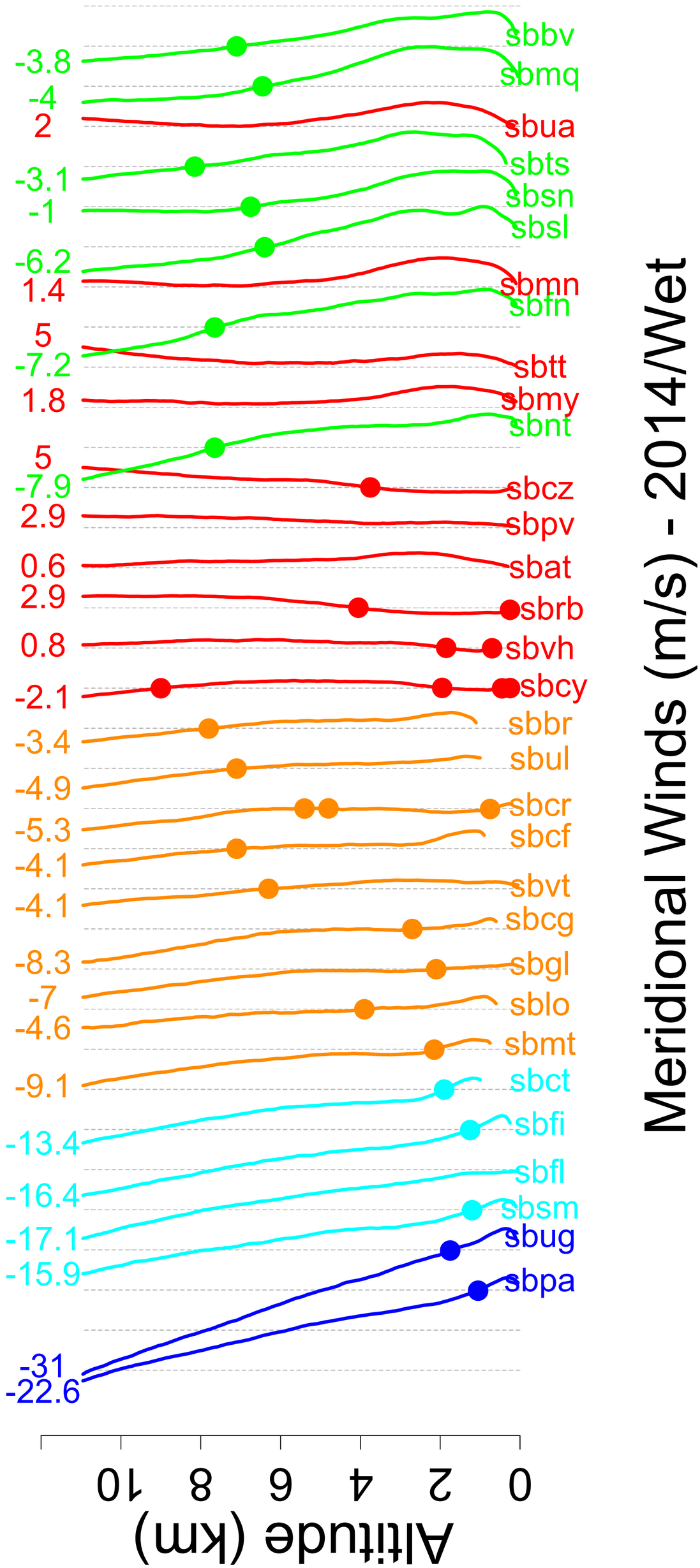
Meridional Winds (m/s) - 2014/Wet
Altitude (km)
0
2
4
6
8
10
sbbv
sbmq
sbua
sbts
sbsn
sbsl
sbmn
sbfn
sbtt
sbmy
sbnt
sbcz
sbpv
sbat
sbrb
sbvh
sbcy
sbbr
sbul
sbcr
sbcf
sbvt
sbcg
sbgl
sblo
sbmt
sbct
sbfi
sbfl
sbsm
sbug
sbpa
-3.8
-4
2
-3.1
-1
-6.2
1.4
5
-7.2
1.8
5
-7.9
2.9
0.6
2.9
0.8
-2.1
-3.4
-4.9
-5.3
-4.1
-4.1
-8.3
-7
-4.6
-9.1
-13.4
-16.4
-17.1
-15.9
-31
-22.6

Figure.

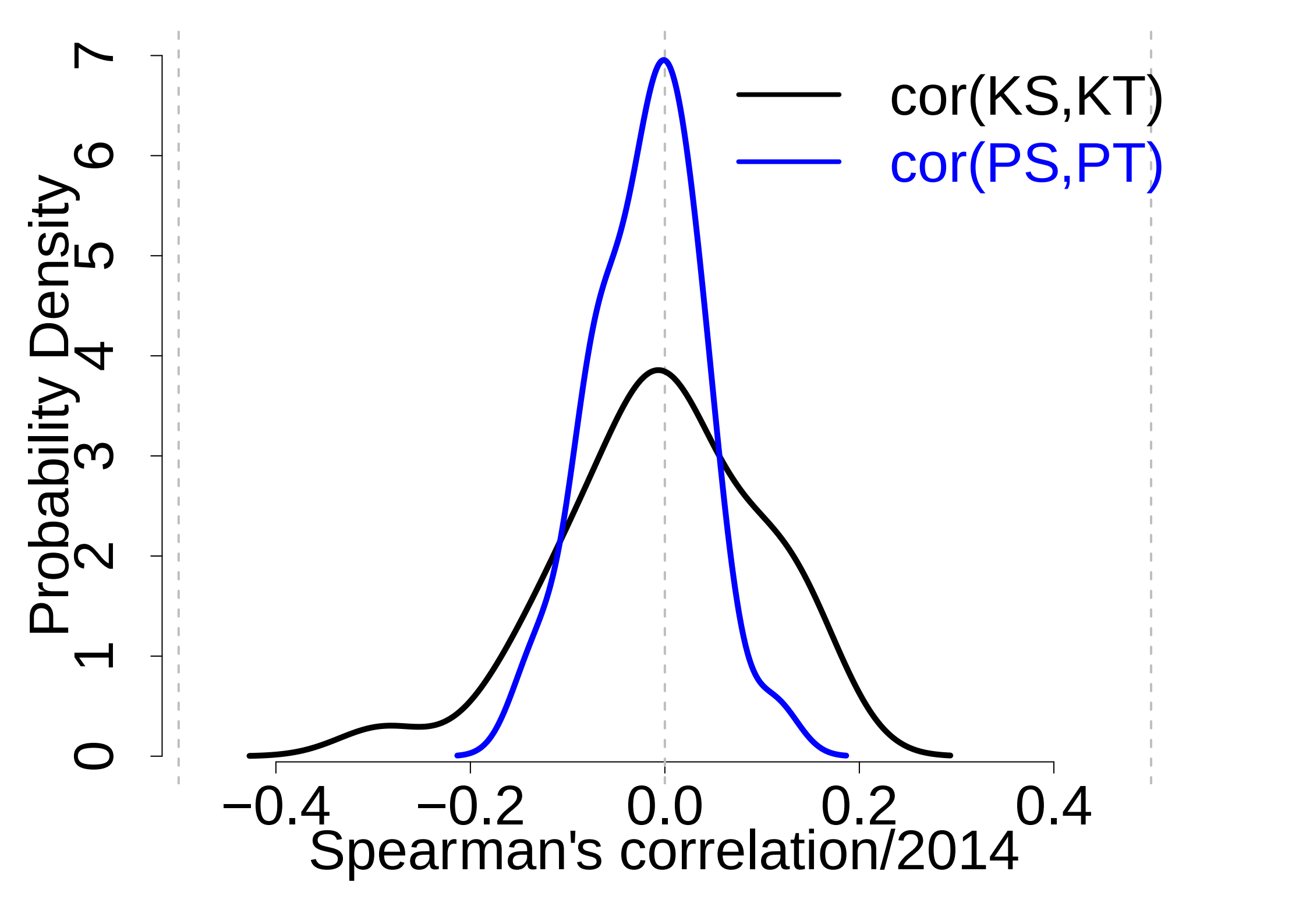
Probability Density
0
1
2
3
4
5
6
7
cor(KS,KT)
cor(PS,PT)
−0.4
−0.2
0.0
0.2
0.4
Spearman's correlation/2014

Figure.

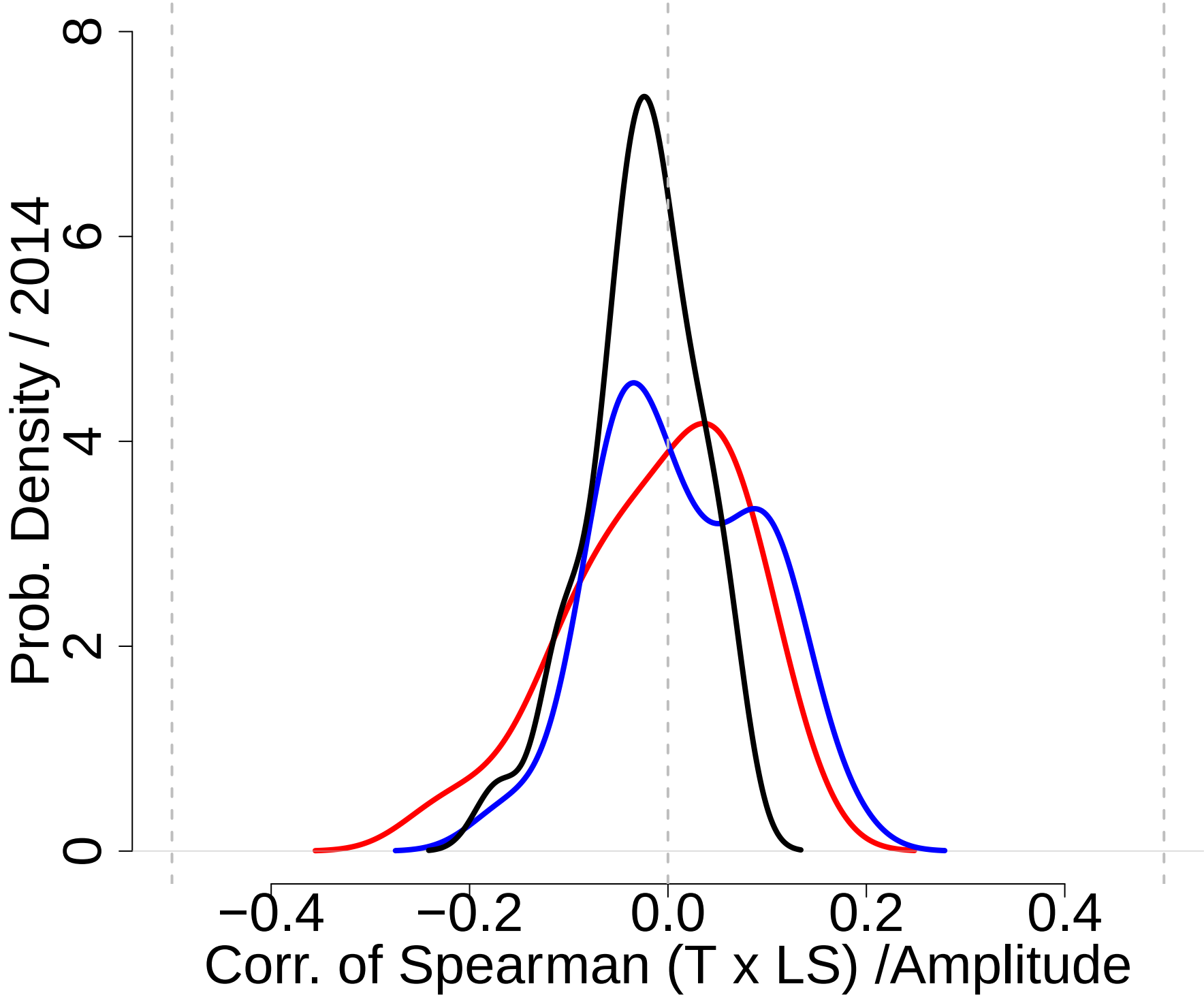
Prob. Density / 2014
0
2
4
6
8
−0.4
−0.2
0.0
0.2
0.4
Corr. of Spearman (T x LS) /Amplitude

Figure.

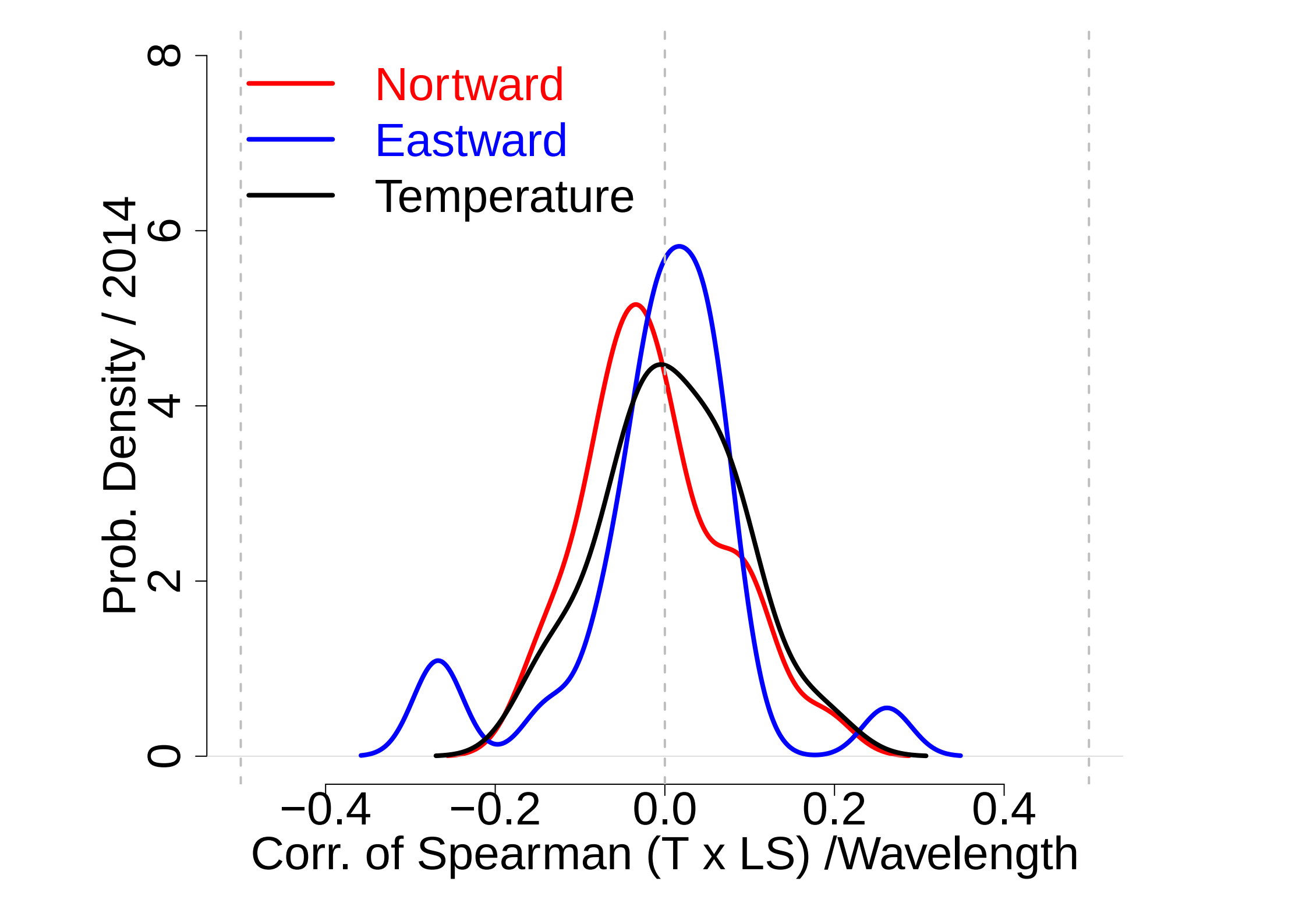
Nortward
Eastward
Temperature
Prob. Density / 2014
0
2
4
6
8
−0.4
−0.2
0.0
0.2
0.4
Corr. of Spearman (T x LS) /Wavelength

Figure.

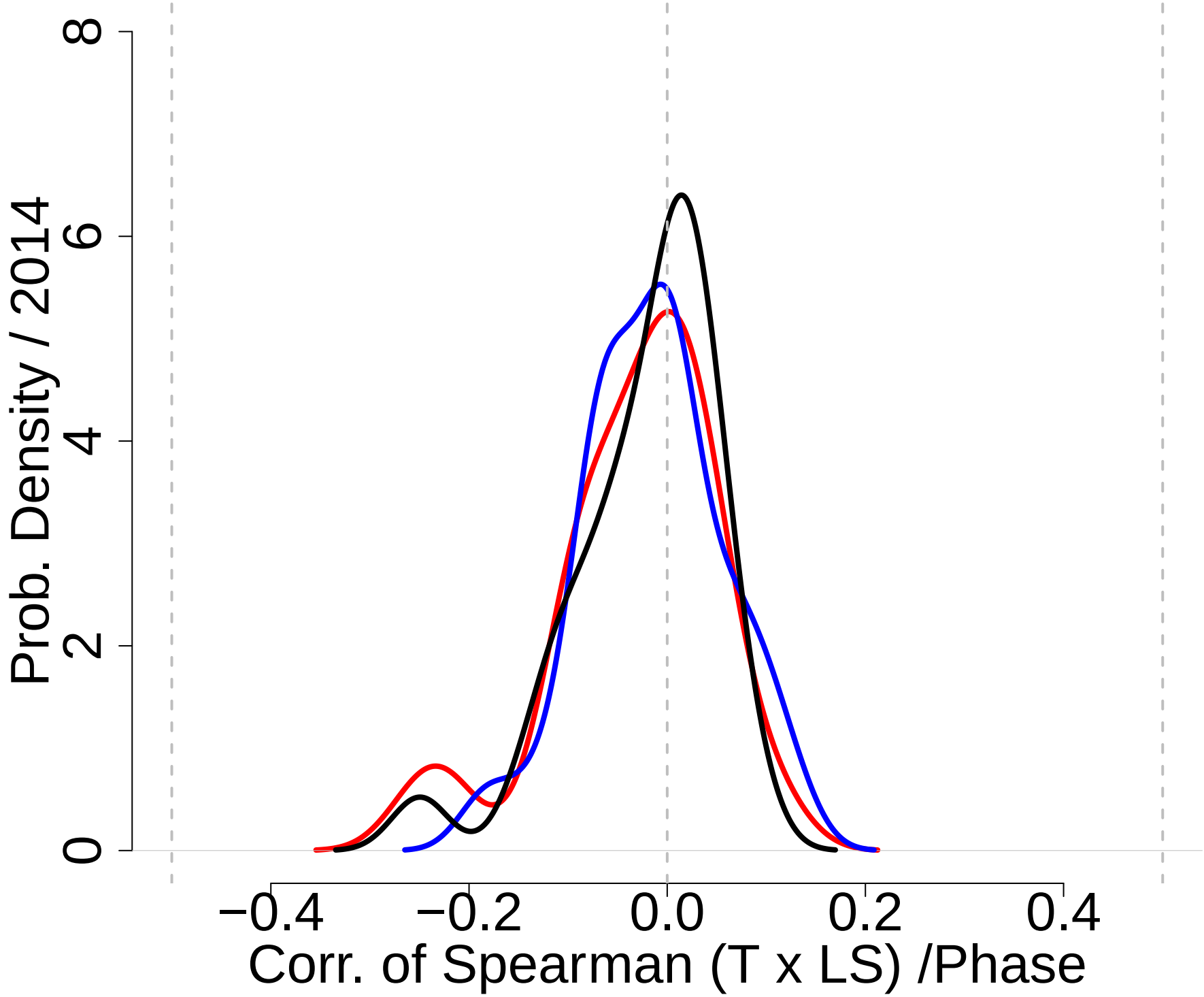
Prob. Density / 2014
0
2
4
6
8
−0.4
−0.2
0.0
0.2
0.4
Corr. of Spearman (T x LS) /Phase

Figure.

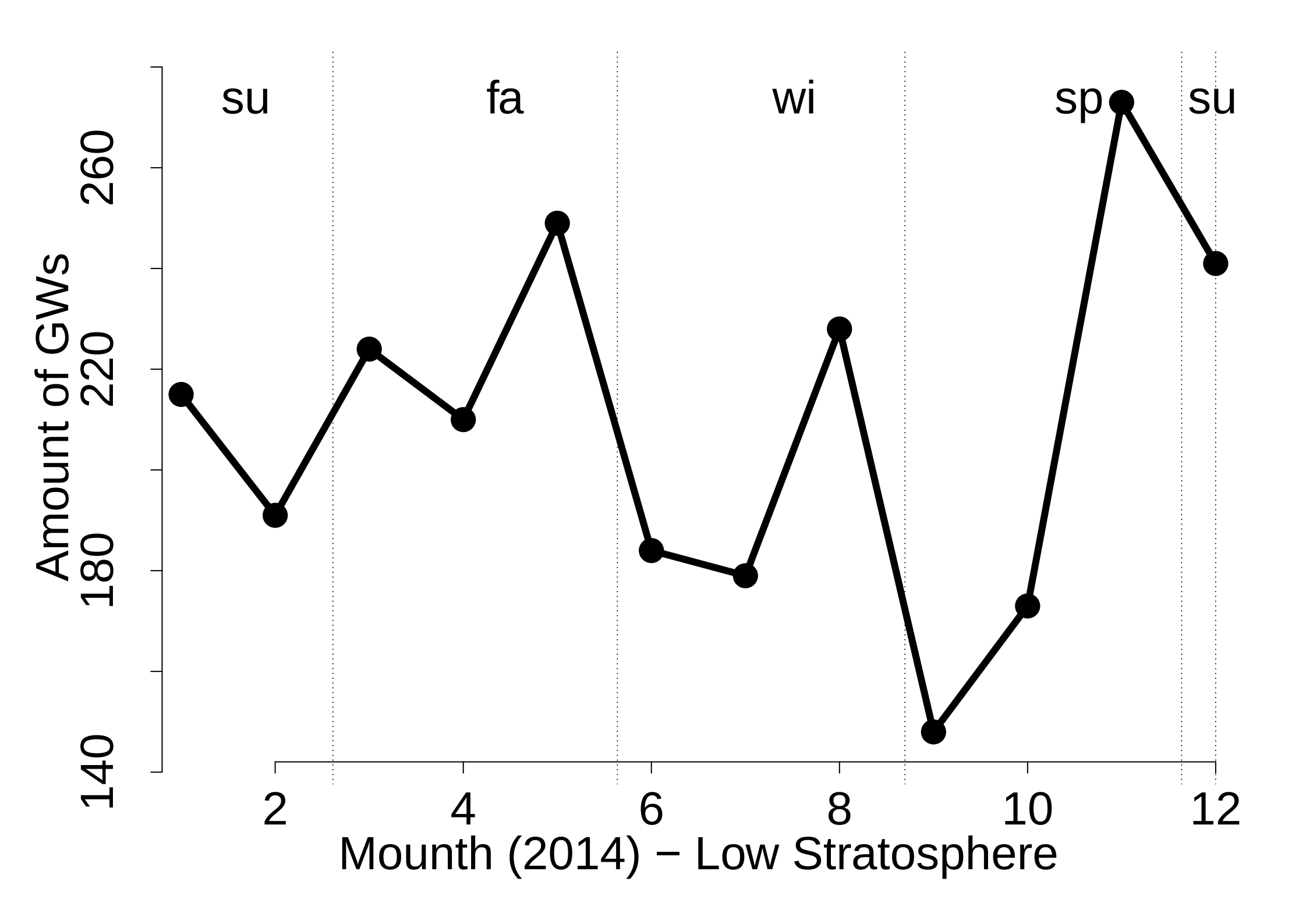
su
fa
wi
sp
su
Amount of GWs
140
180
220
260
2
4
6
8
10
12
Mounth (2014) − Low Stratosphere

Figure.

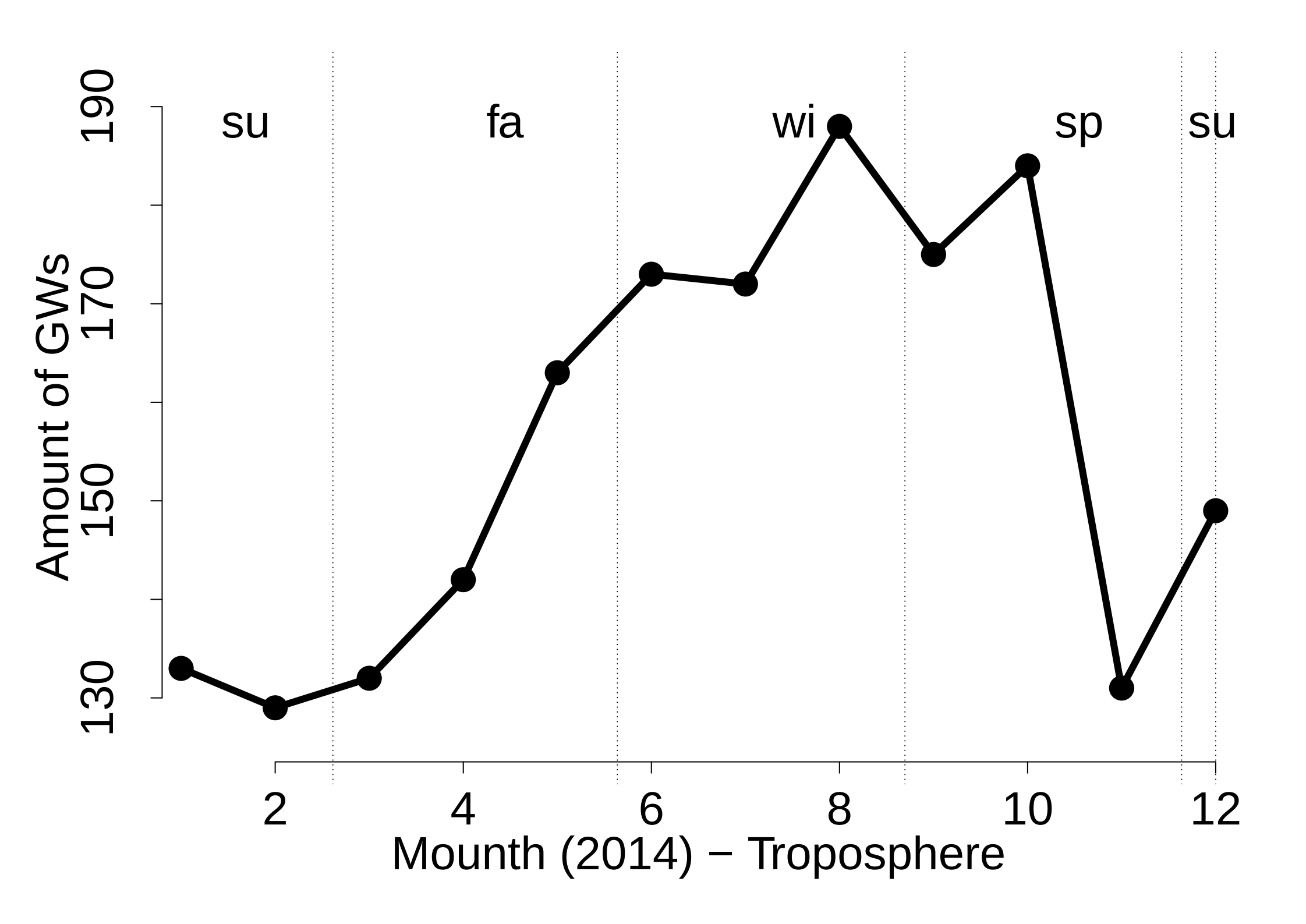
su
fa
wi
sp
su
Amount of GWs
130
150
170
190
2
4
6
8
10
12
Mounth (2014) − Troposphere

Figure.

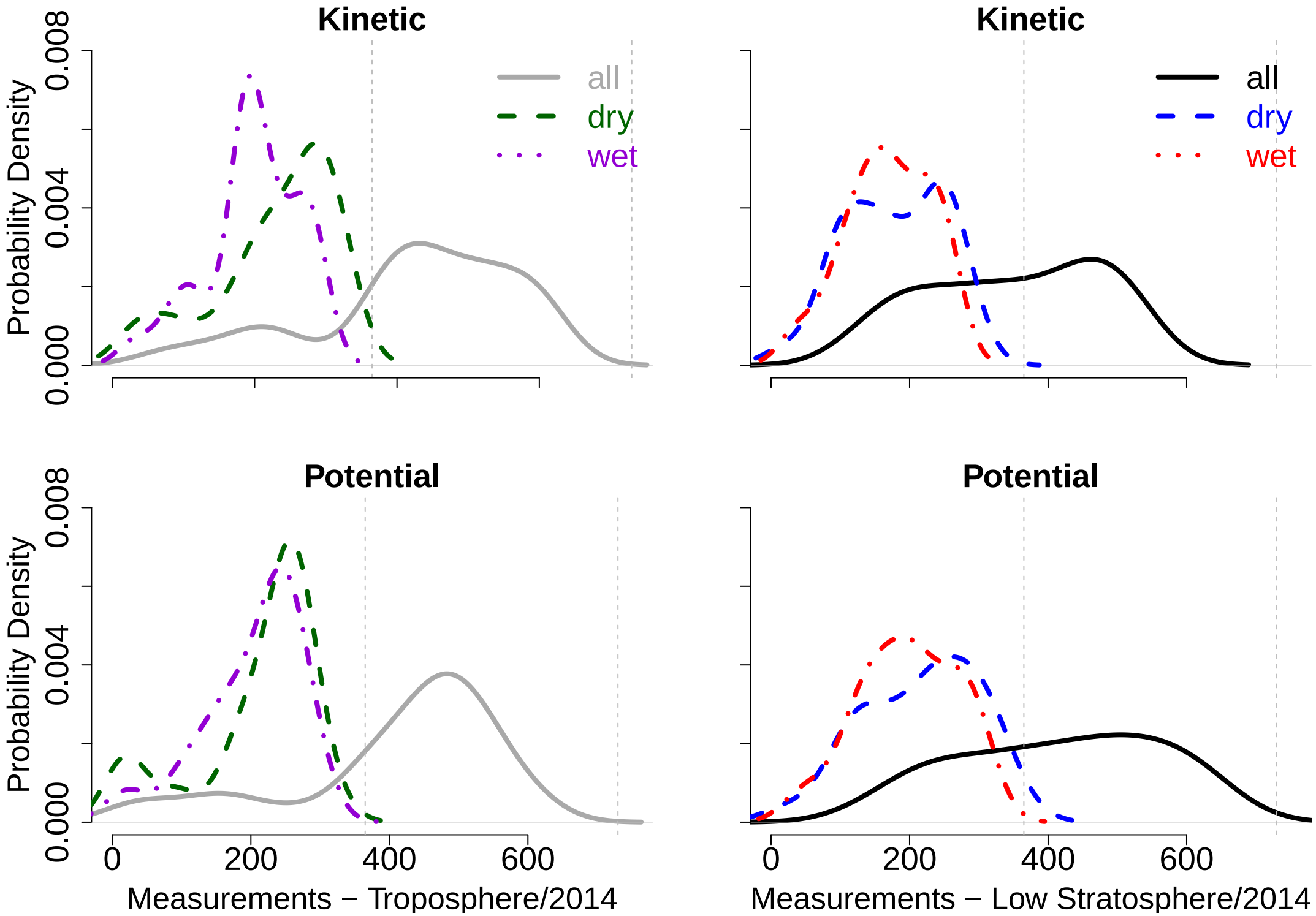
Kinetic
Kinetic
Potential
Potential
Probability Density
0.000
0.004
0.008
all
dry
wet
0
200
400
600
Measurements − Troposphere/2014
Measurements − Low Stratosphere/2014

Figure.

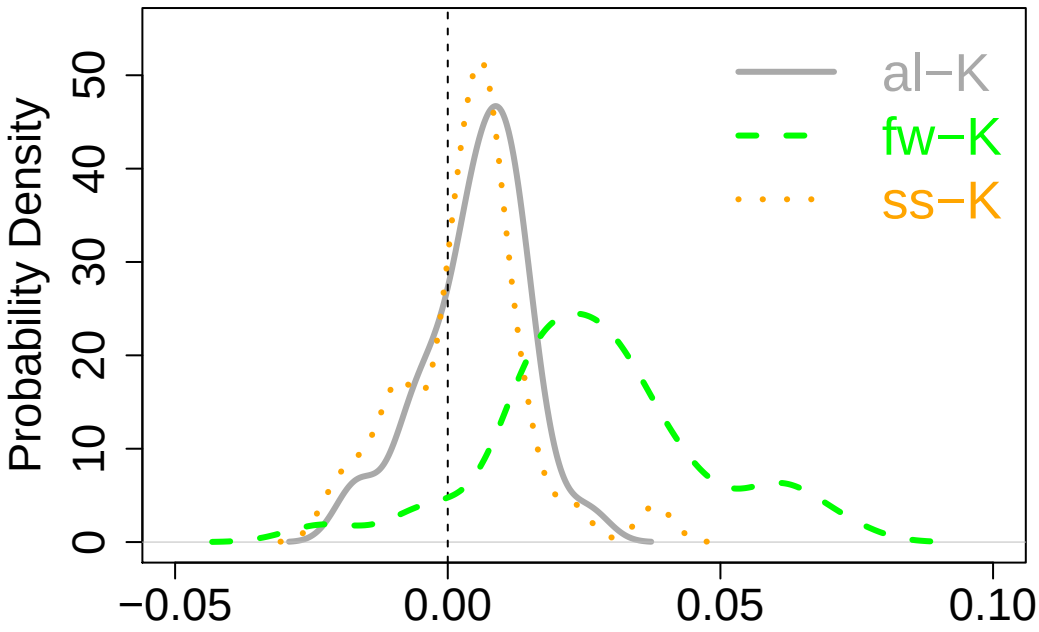
Probability Density
0
10
20
30
40
50
−0.05
0.00
0.05
0.10
al−K
fw−K
ss−K

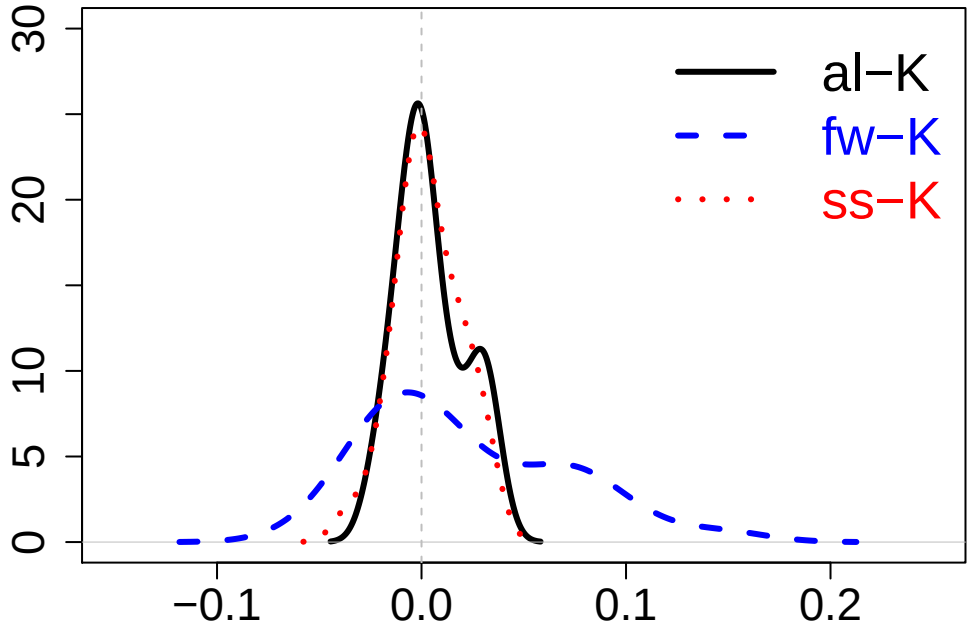
0
5
10
20
30
−0.1
0.0
0.1
0.2
al−K
fw−K
ss−K

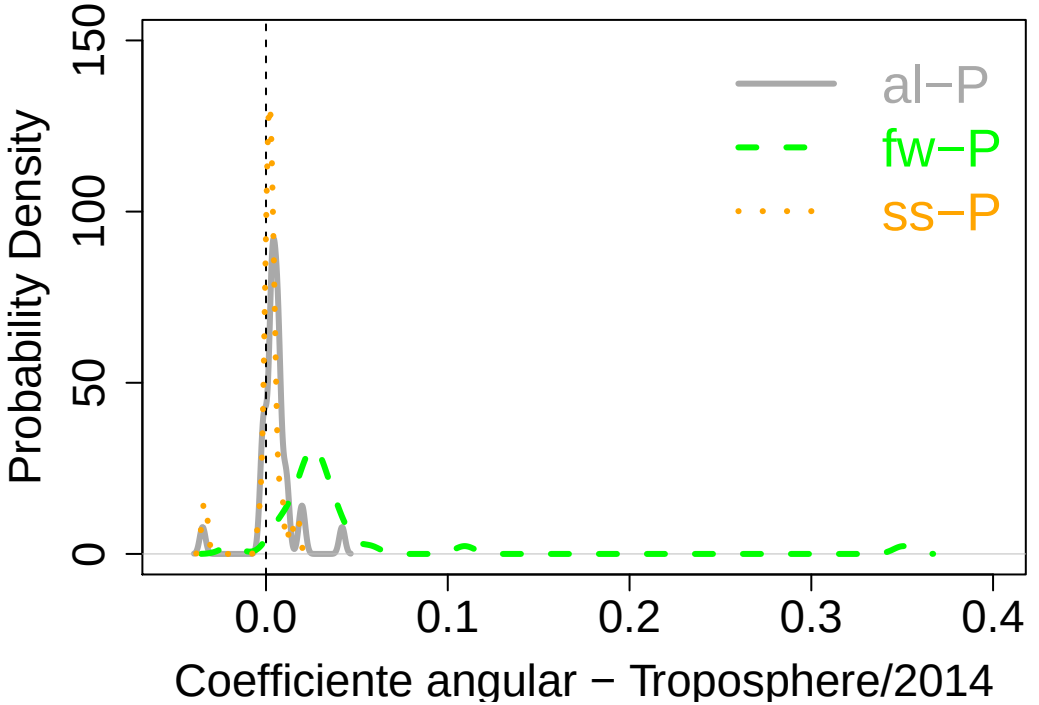
Probability Density
0
50
100
150
0.0
0.1
0.2
0.3
0.4
al−P
fw−P
ss−P
Coefficiente angular − Troposphere/2014

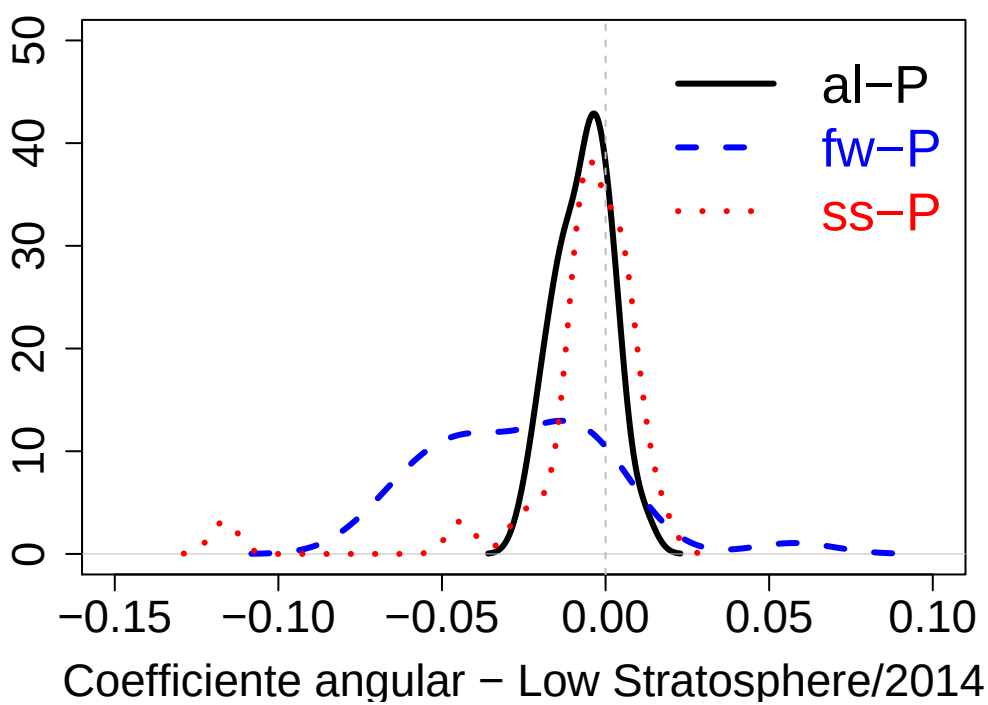
0
10
20
30
40
50
−0.15
−0.10
−0.05
0.00
0.05
0.10
al−P
fw−P
ss−P
Coefficiente angular − Low Stratosphere/2014

Figure.

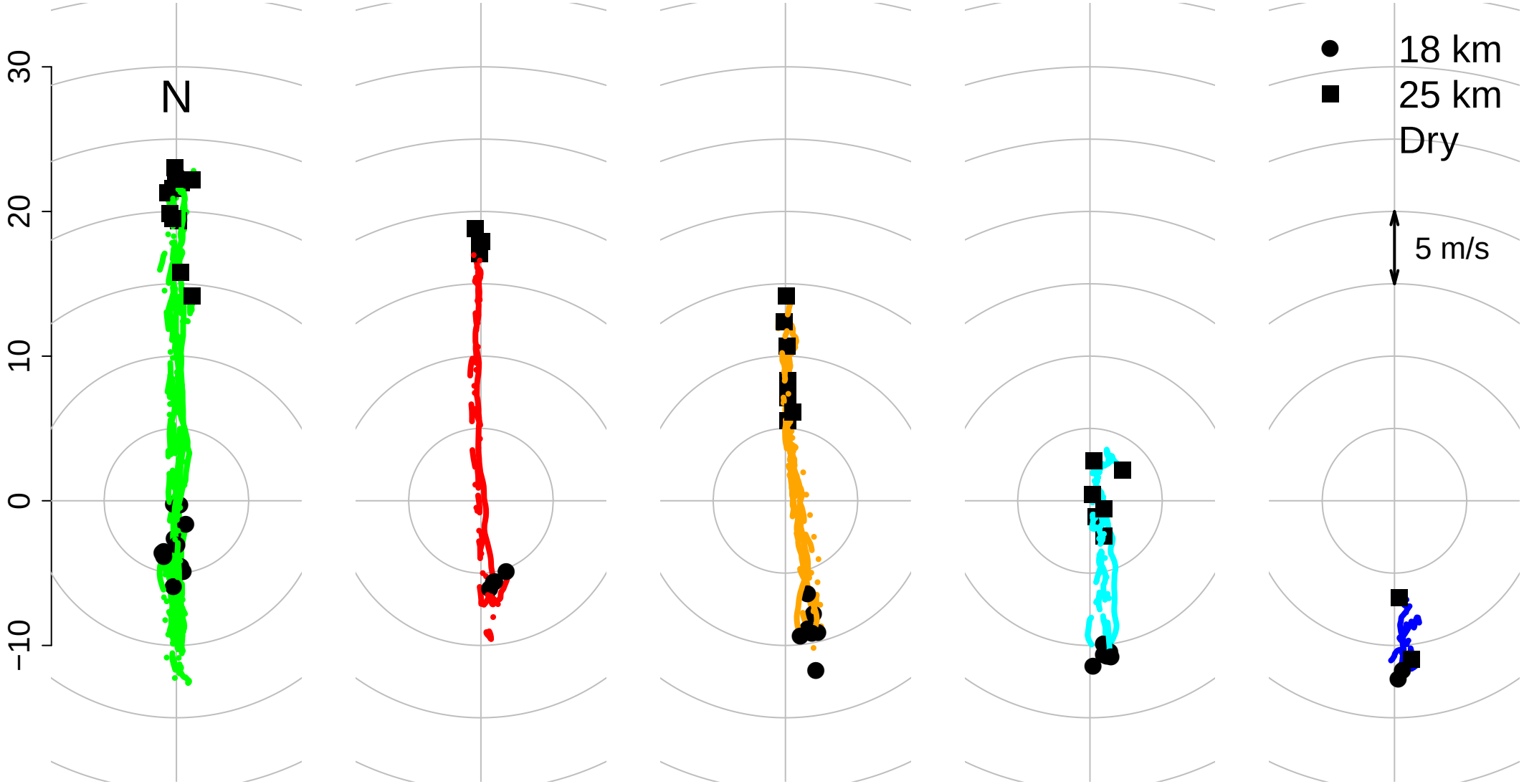
N
30
20
10
0
−10
18 km
25 km
Dry
5 m/s

Figure.

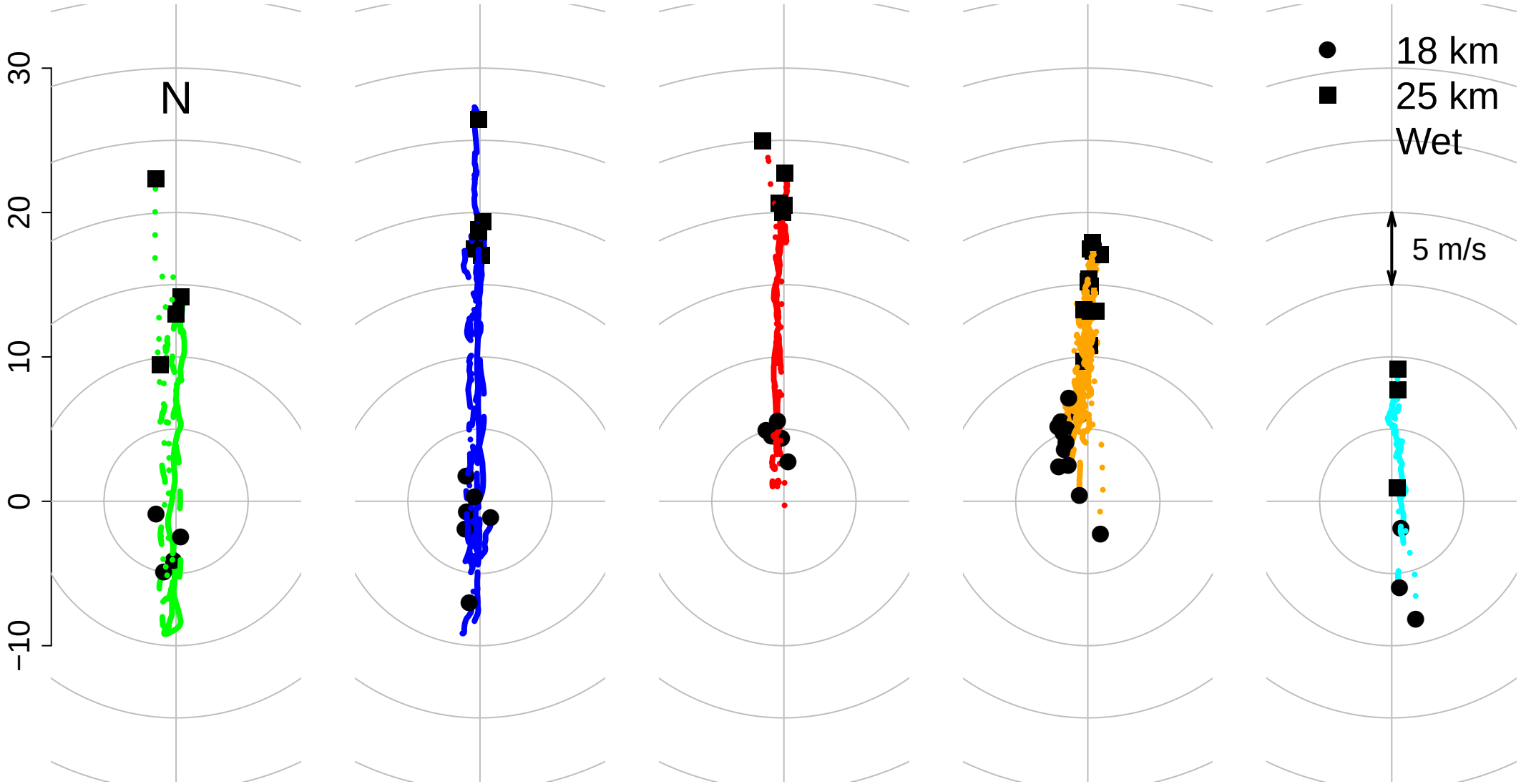
N
30
20
10
0
−10
18 km
25 km
Wet
5 m/s

Figure.

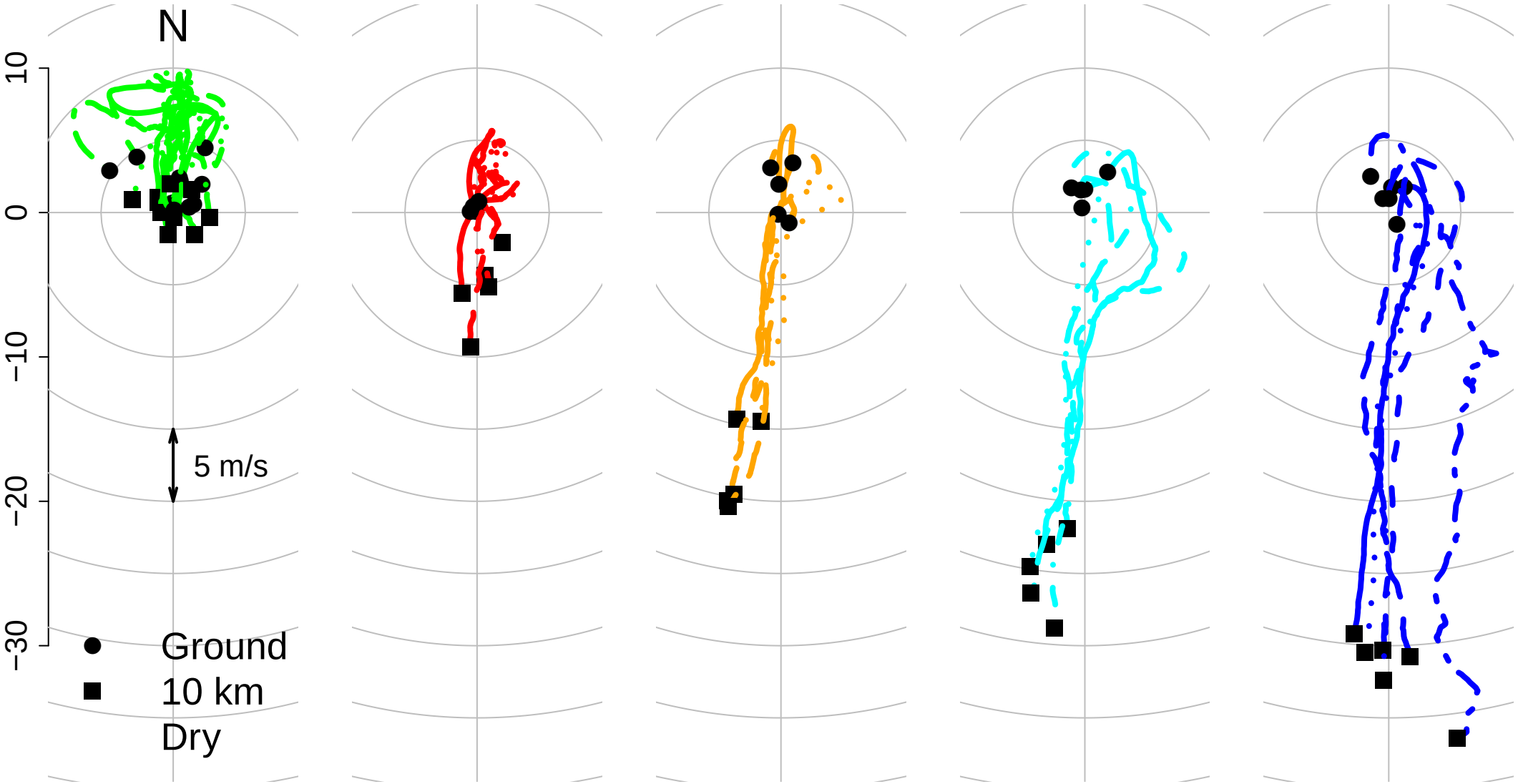
N
10
0
−10
−20
−30
5 m/s
Ground
10 km
Dry

Figure.

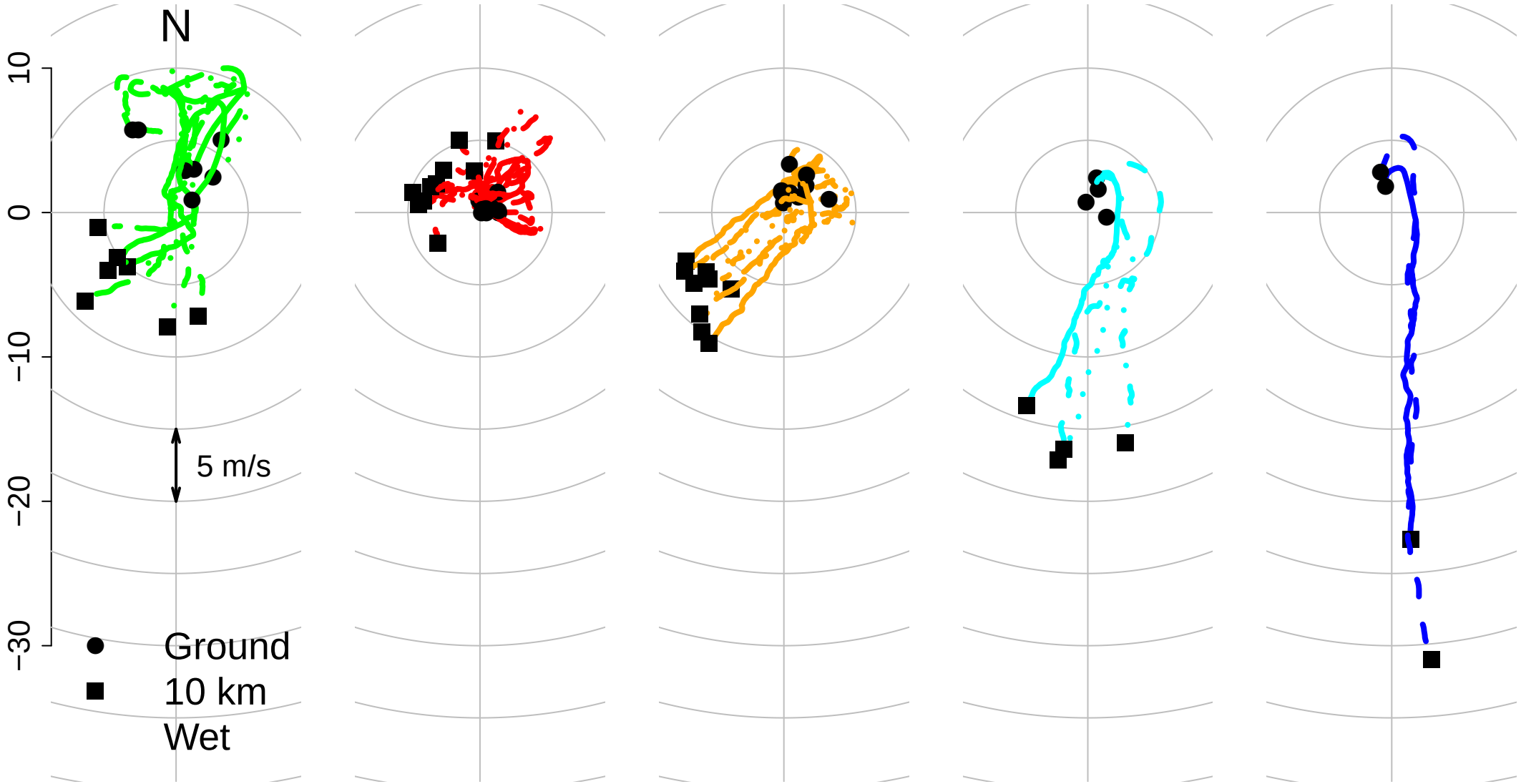
N
10
0
−10
−20
−30
5 m/s
Ground
10 km
Wet

Figure.

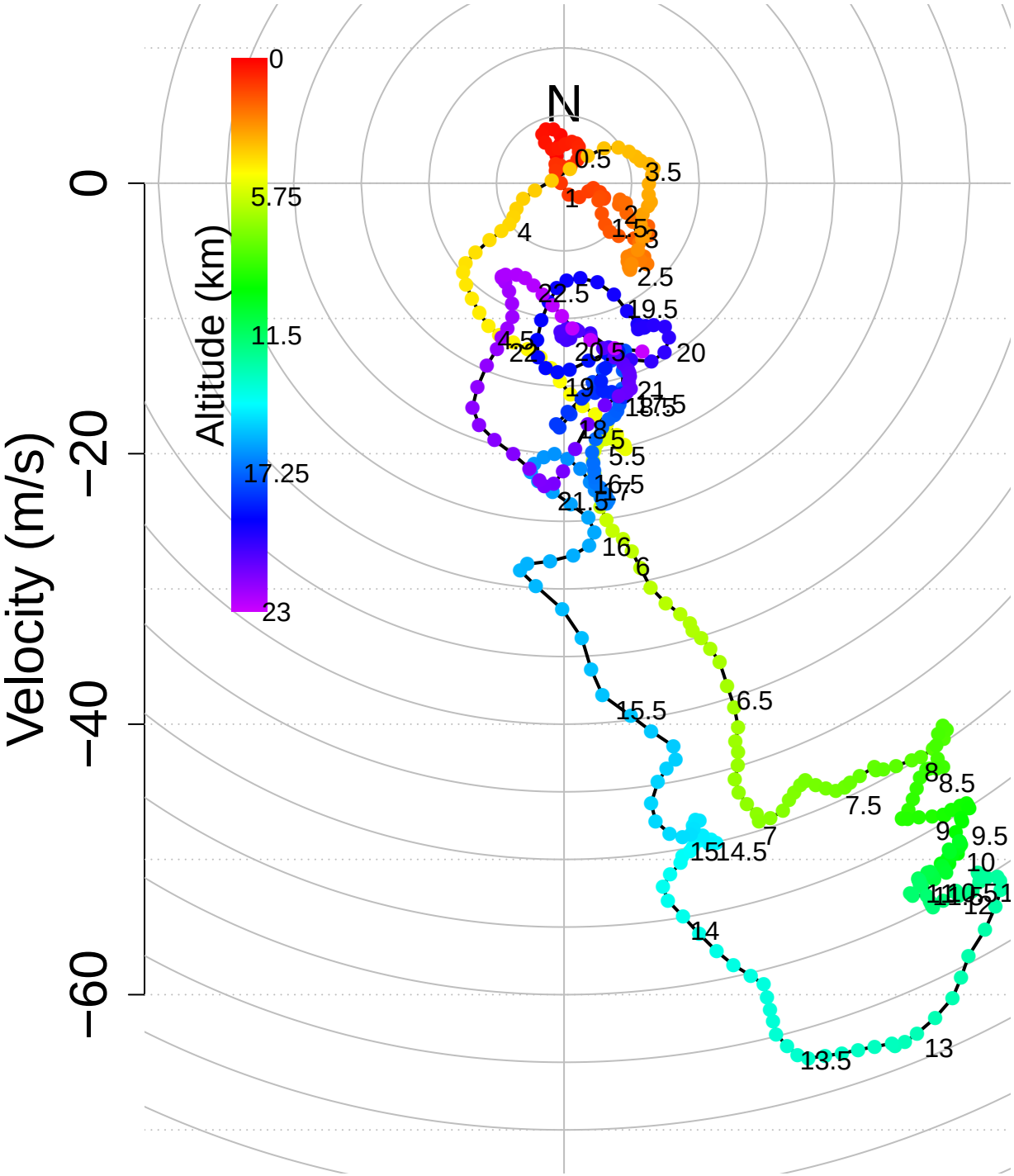
N
Velocity (m/s)
0
−20
−40
−60
Altitude (km)
0
5.75
11.5
17.25
23

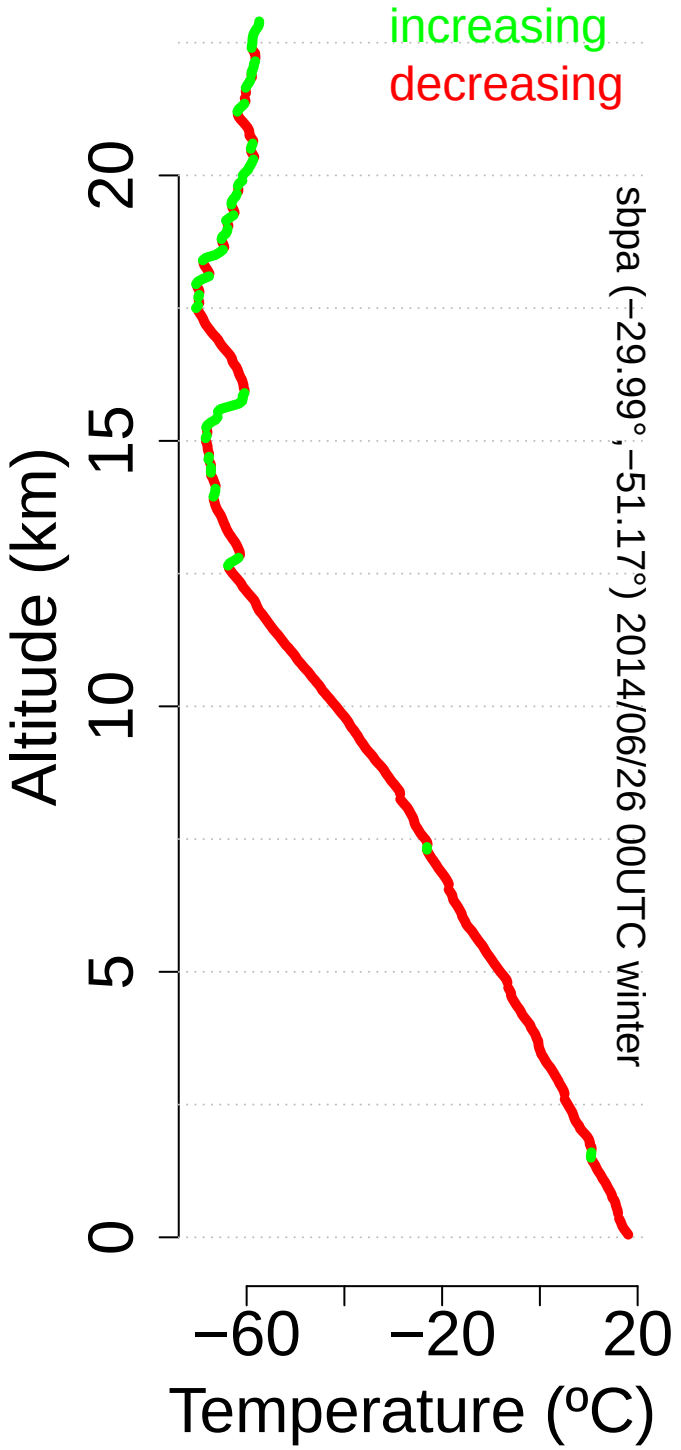
increasing
decreasing
Altitude (km)
0
5
10
15
20
−60
−20
20
Temperature (ºC)
sbpa (−29.99°, −51.17°) 2014/06/26 00UTC winter

Figure.

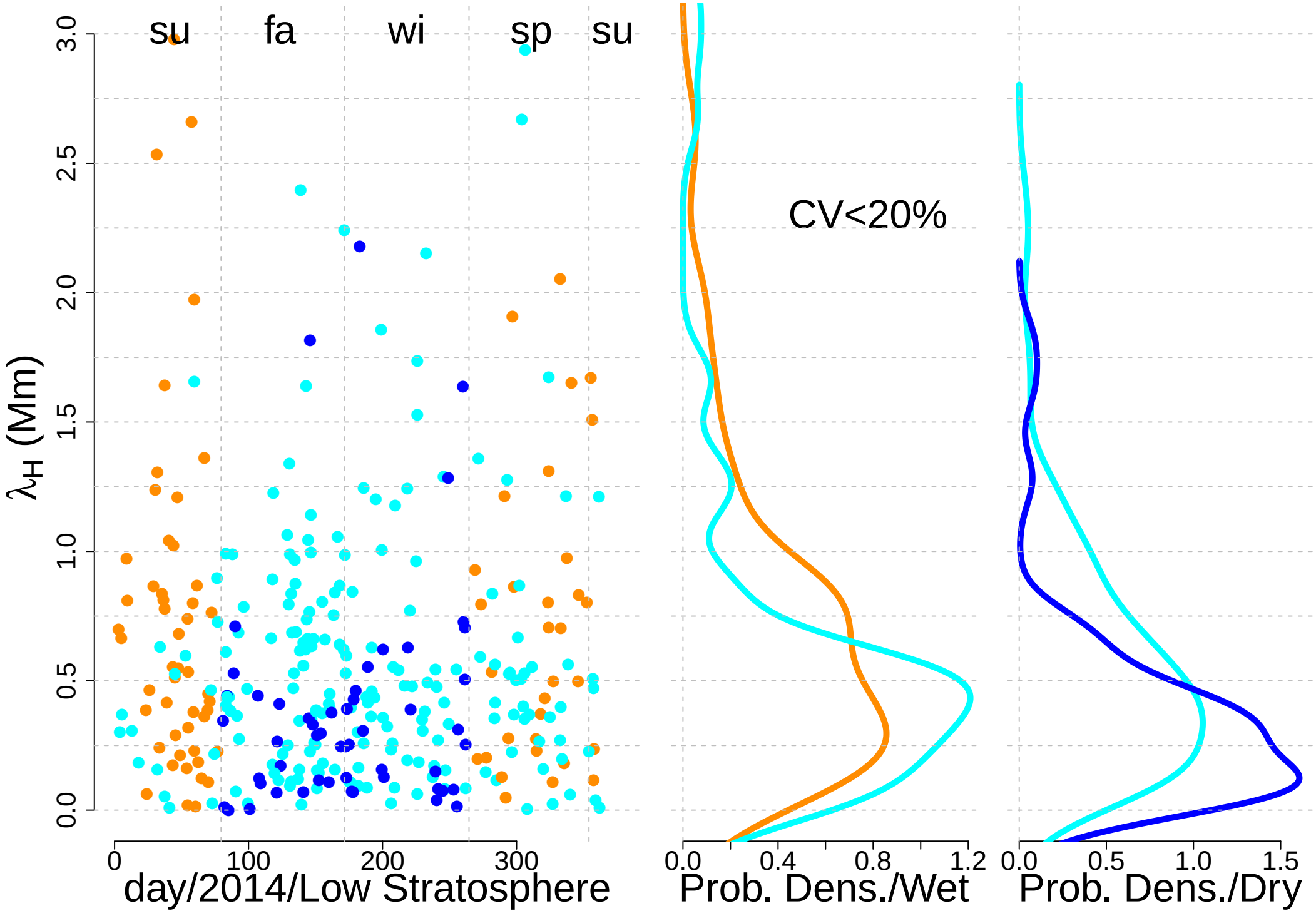
su
fa
wi
sp
su
λ_H (Mm)
0.0
0.5
1.0
1.5
2.0
2.5
3.0
0
100
200
300
day/2014/Low Stratosphere
CV<20%
0.0
0.4
0.8
1.2
Prob. Dens./Wet
0.0
0.5
1.0
1.5
Prob. Dens./Dry

Figure.

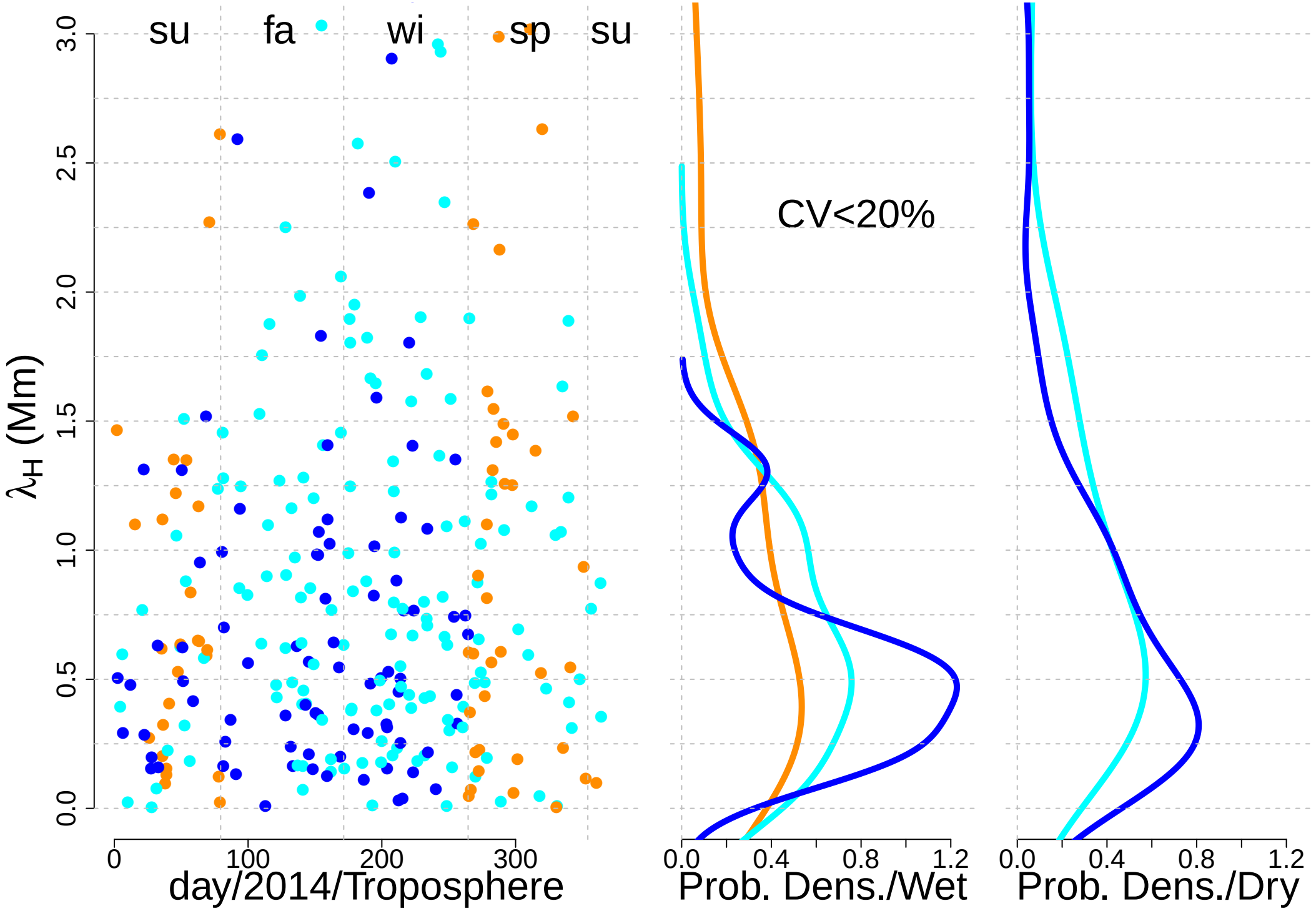
su
fa
wi
sp
su
λ_H (Mm)
0.0
0.5
1.0
1.5
2.0
2.5
3.0
0
100
200
300
day/2014/Troposphere
CV<20%
0.0
0.4
0.8
1.2
Prob. Dens./Wet
0.0
0.4
0.8
1.2
Prob. Dens./Dry

Figure.

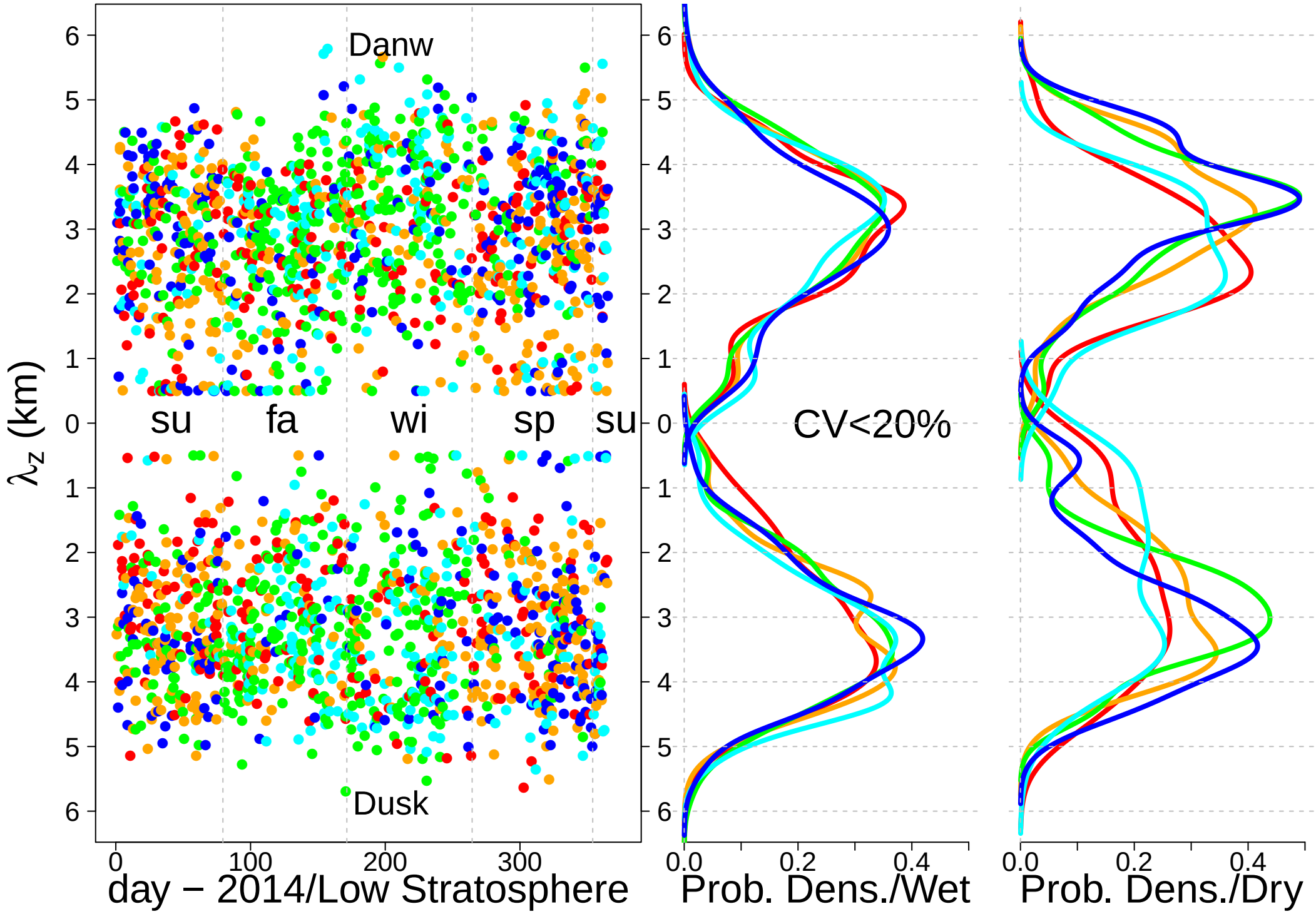
Danw
Dusk
su
fa
wi
sp
su
CV<20%
λz (km)
day – 2014/Low Stratosphere
Prob. Dens./Wet
Prob. Dens./Dry
0
100
200
300
0.0
0.2
0.4
1
2
3
4
5
6

Figure.

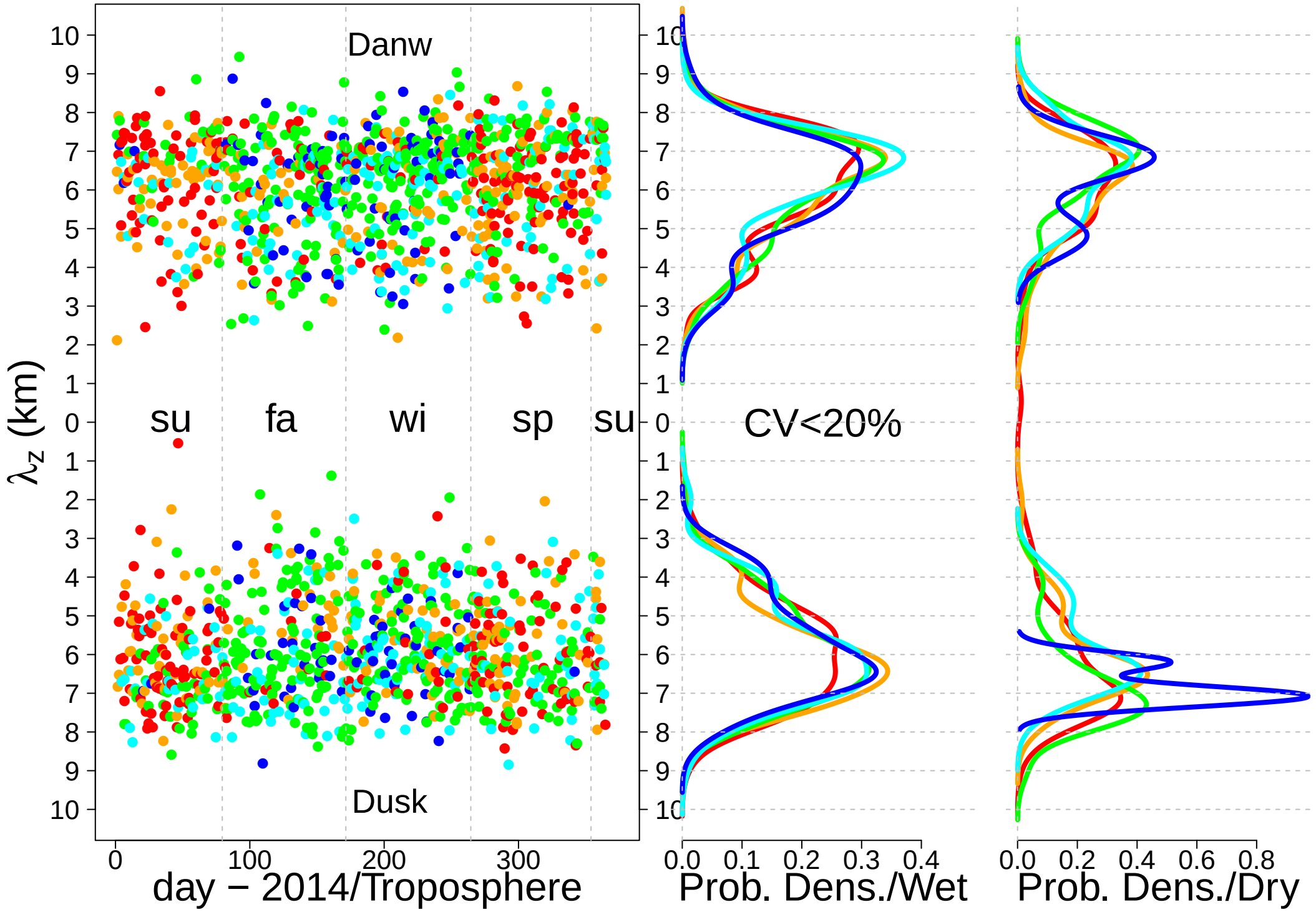
Danw
Dusk
su
fa
wi
sp
su
CV<20%
λ_z (km)
day − 2014/Troposphere
Prob. Dens./Wet
Prob. Dens./Dry

Figure.

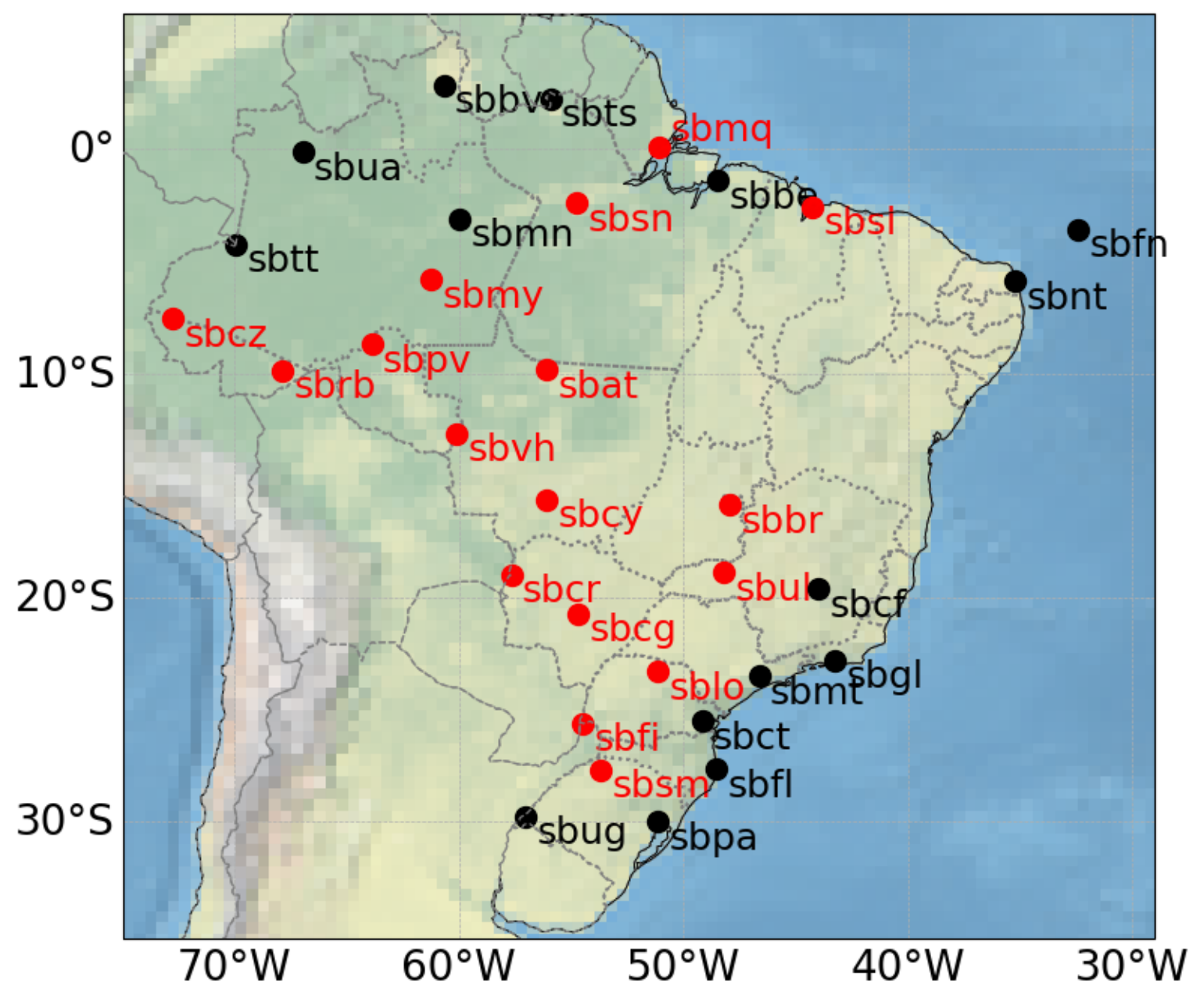
sbbv
sbts
sbmq
sbua
sbbe
sbsn
sbsl
sbfn
sbmn
sbtt
sbnt
sbmy
sbcz
sbpv
sbrb
sbat
sbvh
sbcy
sbbr
sbcr
sbul
sbcf
sbcg
sbgl
sblo
sbmt
sbfi
sbct
sbsm
sbfl
sbug
sbpa
0°
10°S
20°S
30°S
70°W
60°W
50°W
40°W
30°W

Figure.

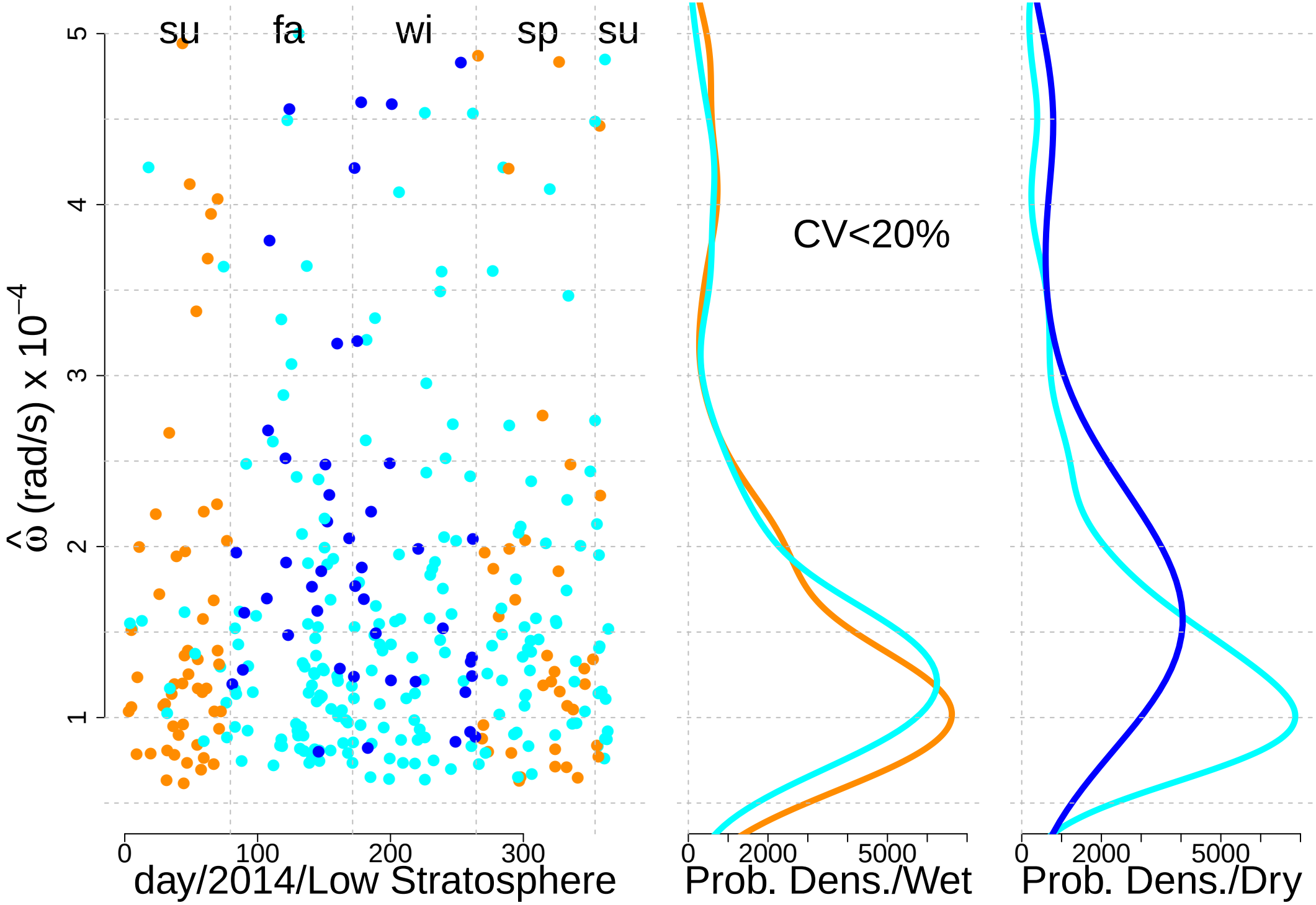
su
fa
wi
sp
su
$\hat{\omega}$ (rad/s) x 10^{-4}
1
2
3
4
5
0
100
200
300
day/2014/Low Stratosphere
CV<20%
0
2000
5000
Prob. Dens./Wet
0
2000
5000
Prob. Dens./Dry

Figure.

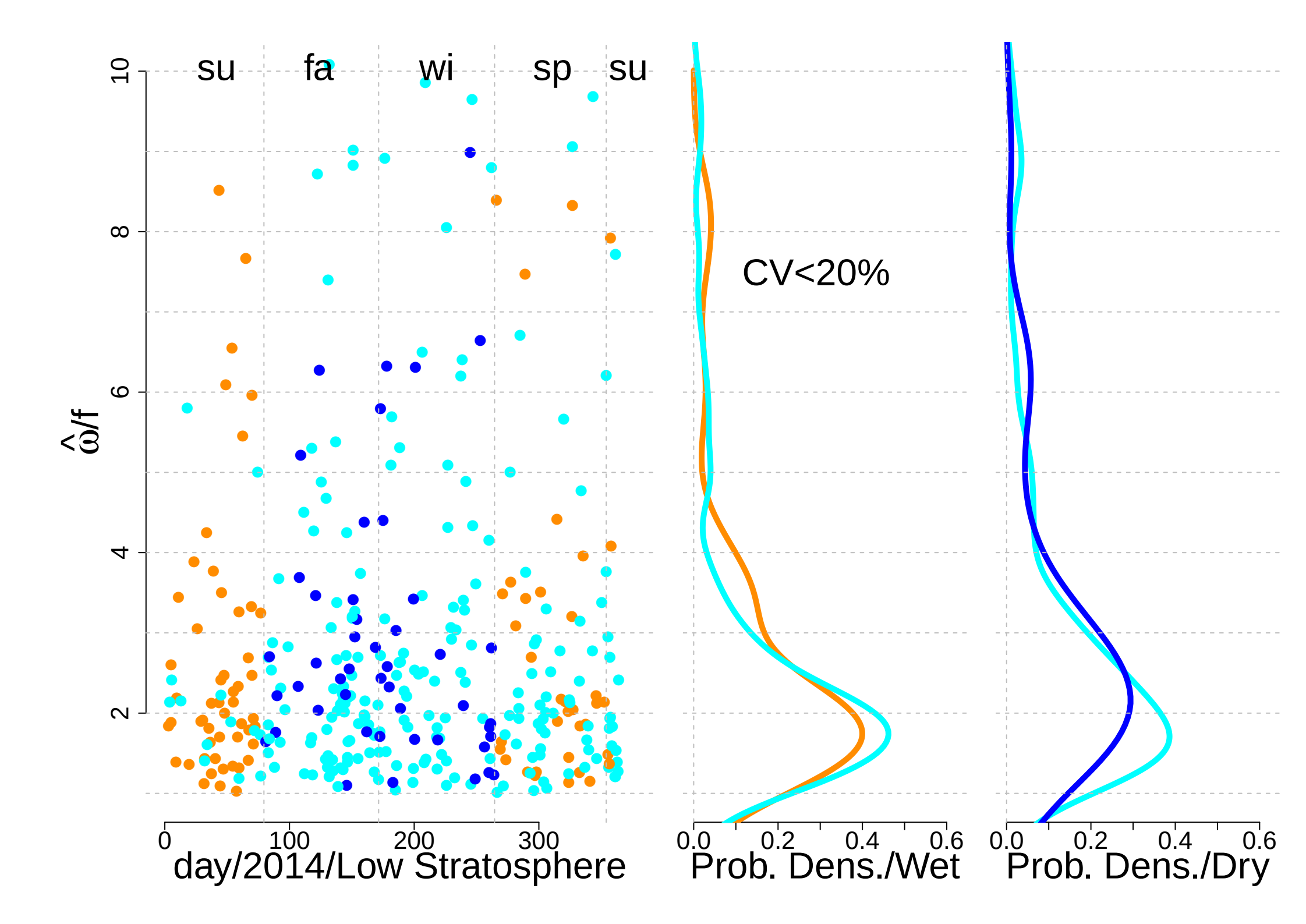
su
fa
wi
sp
su
10
8
6
4
2
$\hat{\omega}/f$
0
100
200
300
day/2014/Low Stratosphere
CV<20%
0.0
0.2
0.4
0.6
Prob. Dens./Wet
0.0
0.2
0.4
0.6
Prob. Dens./Dry

Figure.

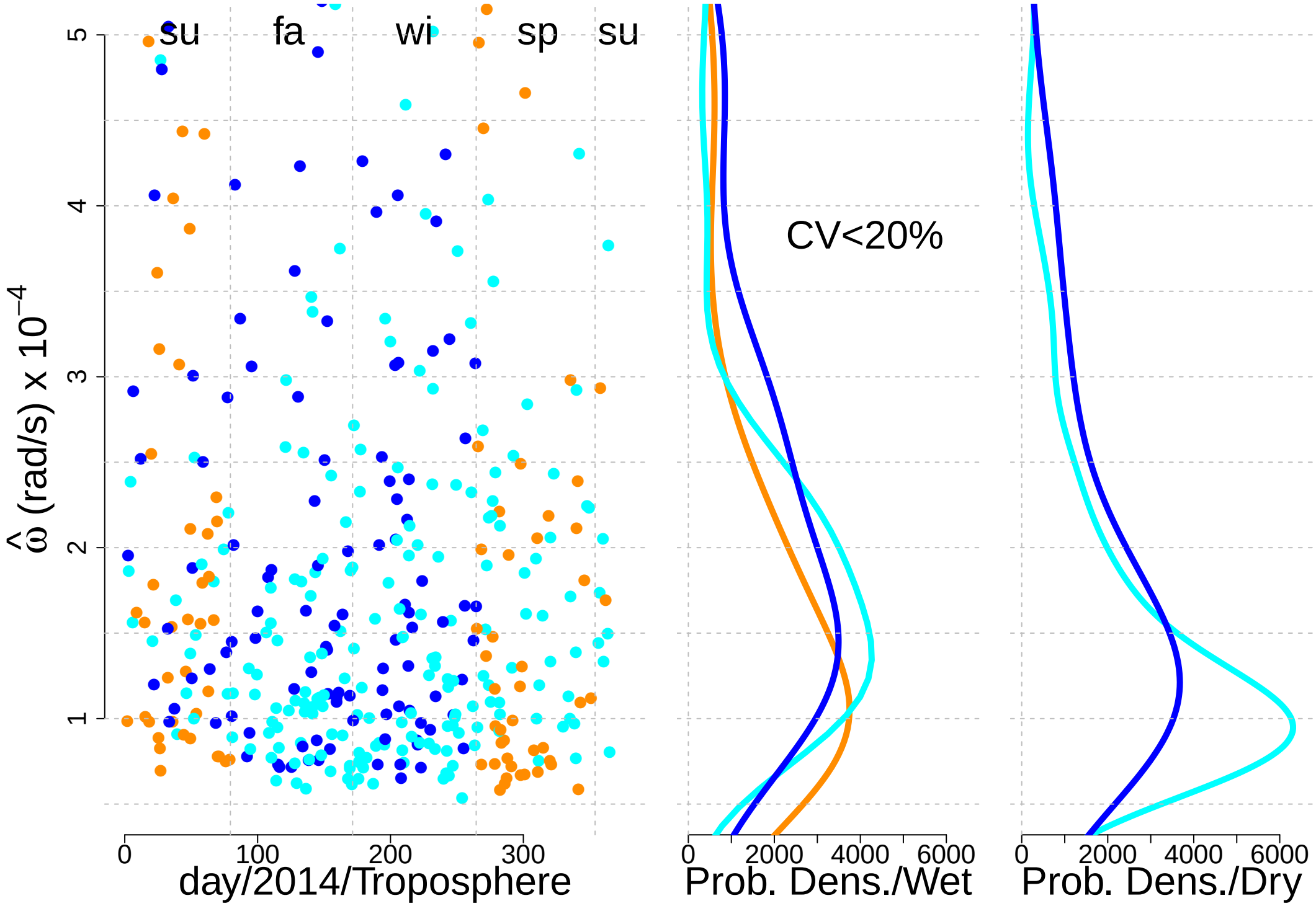
su
fa
wi
sp
su
$\hat{\omega}$ (rad/s) x 10^{-4}
1
2
3
4
5
0
100
200
300
day/2014/Troposphere
CV<20%
0
2000
4000
6000
Prob. Dens./Wet
0
2000
4000
6000
Prob. Dens./Dry

Figure.

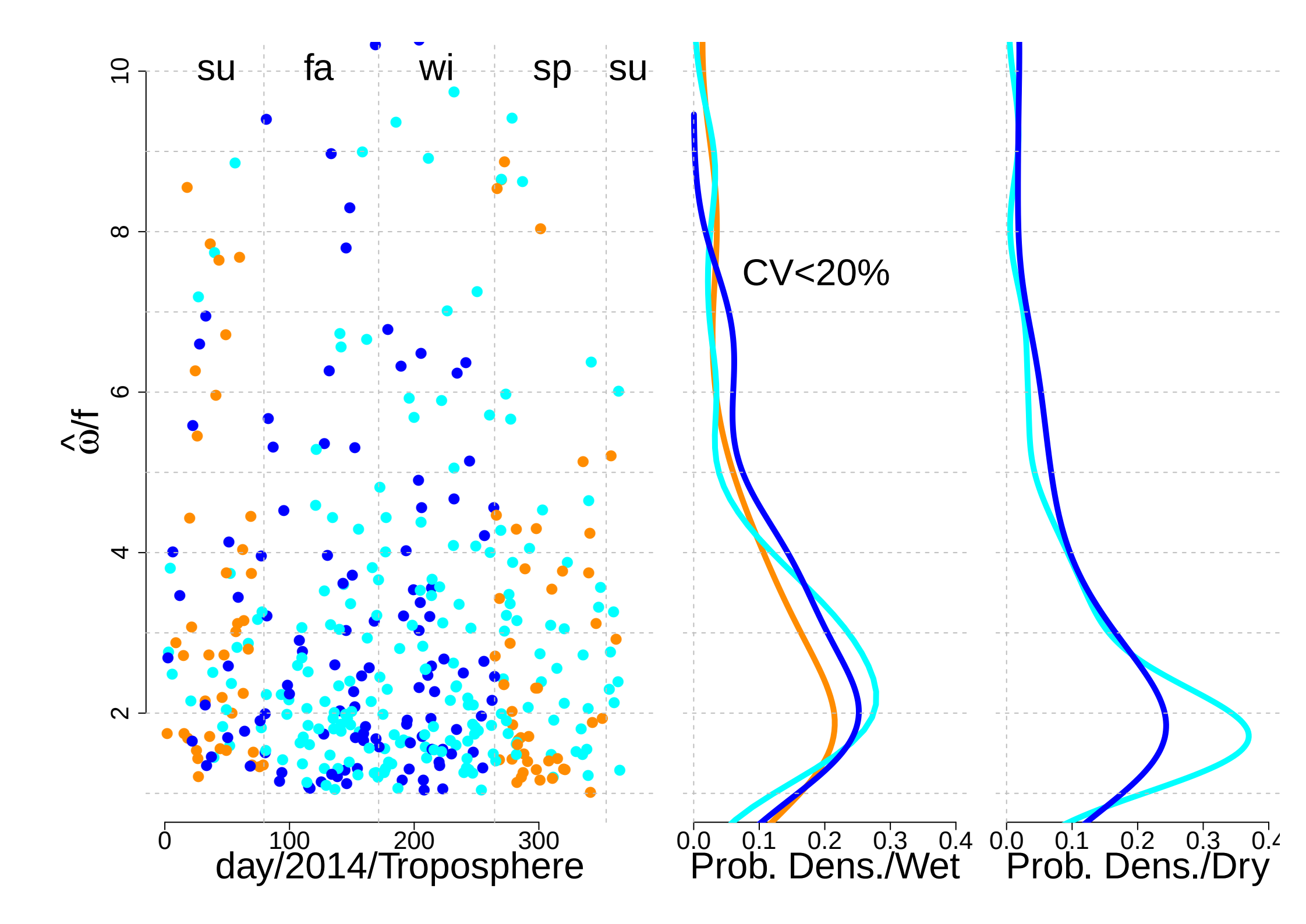
su
fa
wi
sp
su
10
8
6
4
2
$\hat{\omega}/f$
0
100
200
300
day/2014/Troposphere
CV<20%
0.0
0.1
0.2
0.3
0.4
Prob. Dens./Wet
Prob. Dens./Dry

Figure.

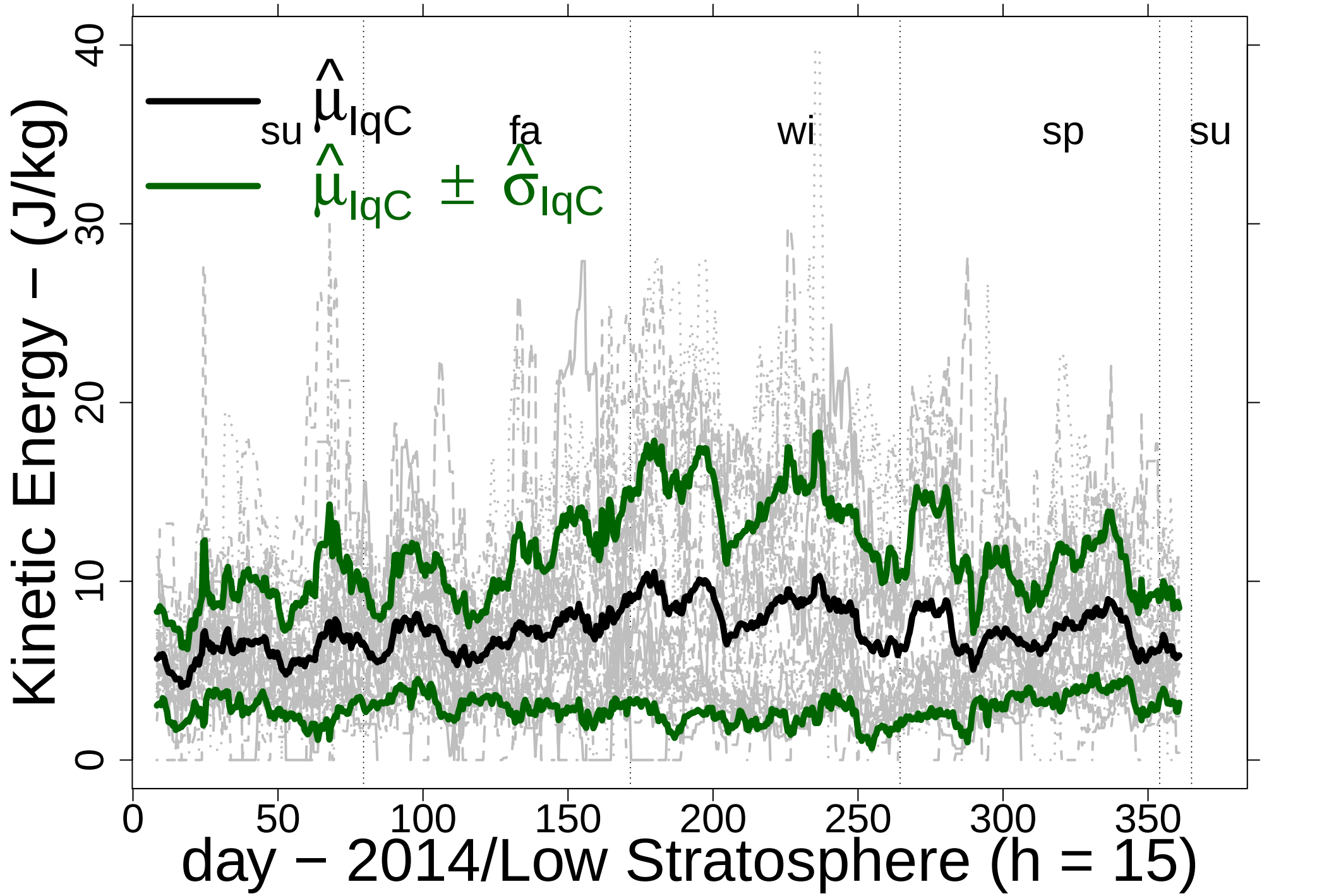
Kinetic Energy − (J/kg)
0
10
20
30
40
su
fa
wi
sp
su
$\hat{\mu}_{IqC}$
$\hat{\mu}_{IqC} \pm \hat{\sigma}_{IqC}$
0
50
100
150
200
250
300
350
day − 2014/Low Stratosphere (h = 15)

Figure.

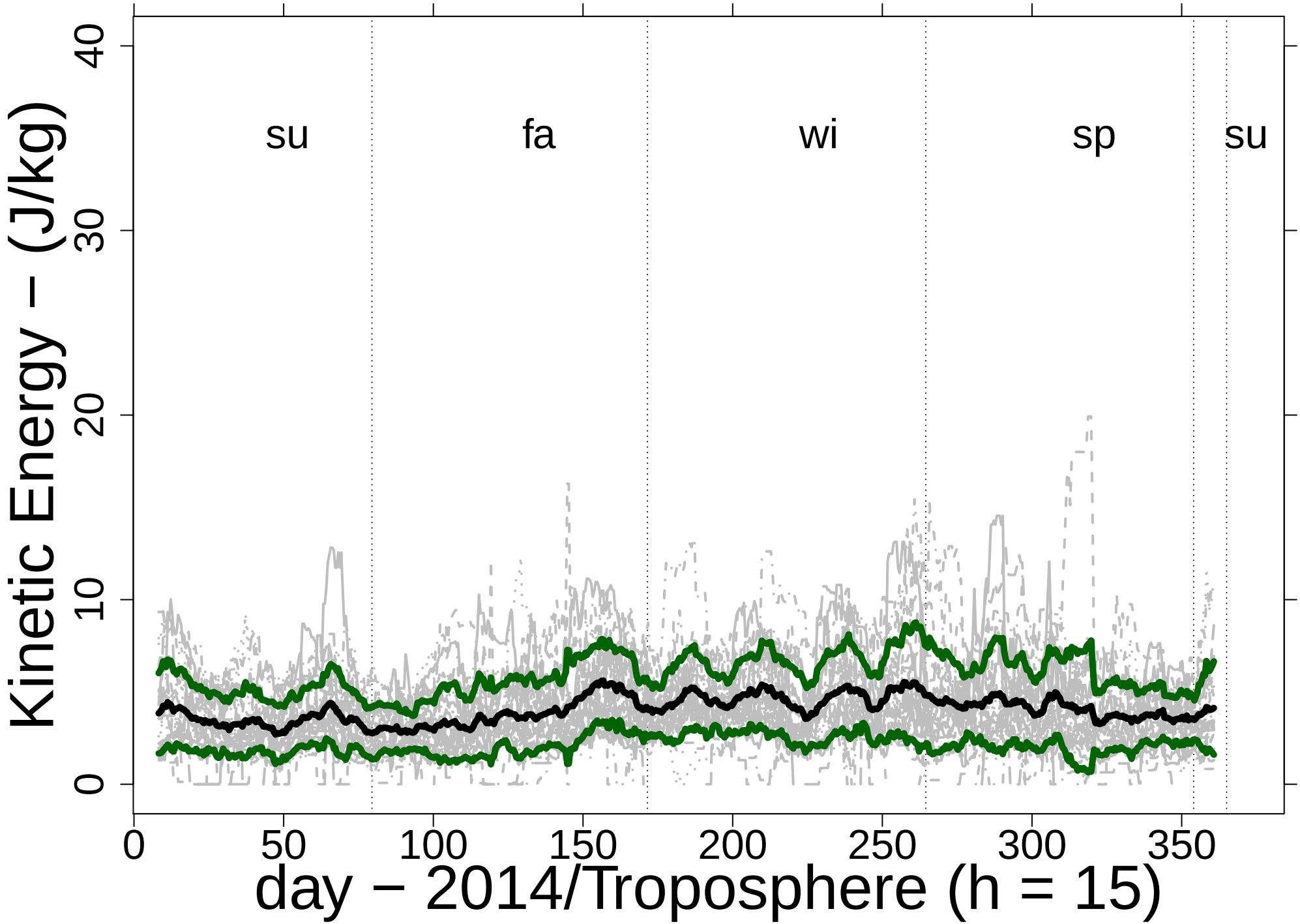
su
fa
wi
sp
su
Kinetic Energy – (J/kg)
0
10
20
30
40
0
50
100
150
200
250
300
350
day – 2014/Troposphere (h = 15)

Figure.

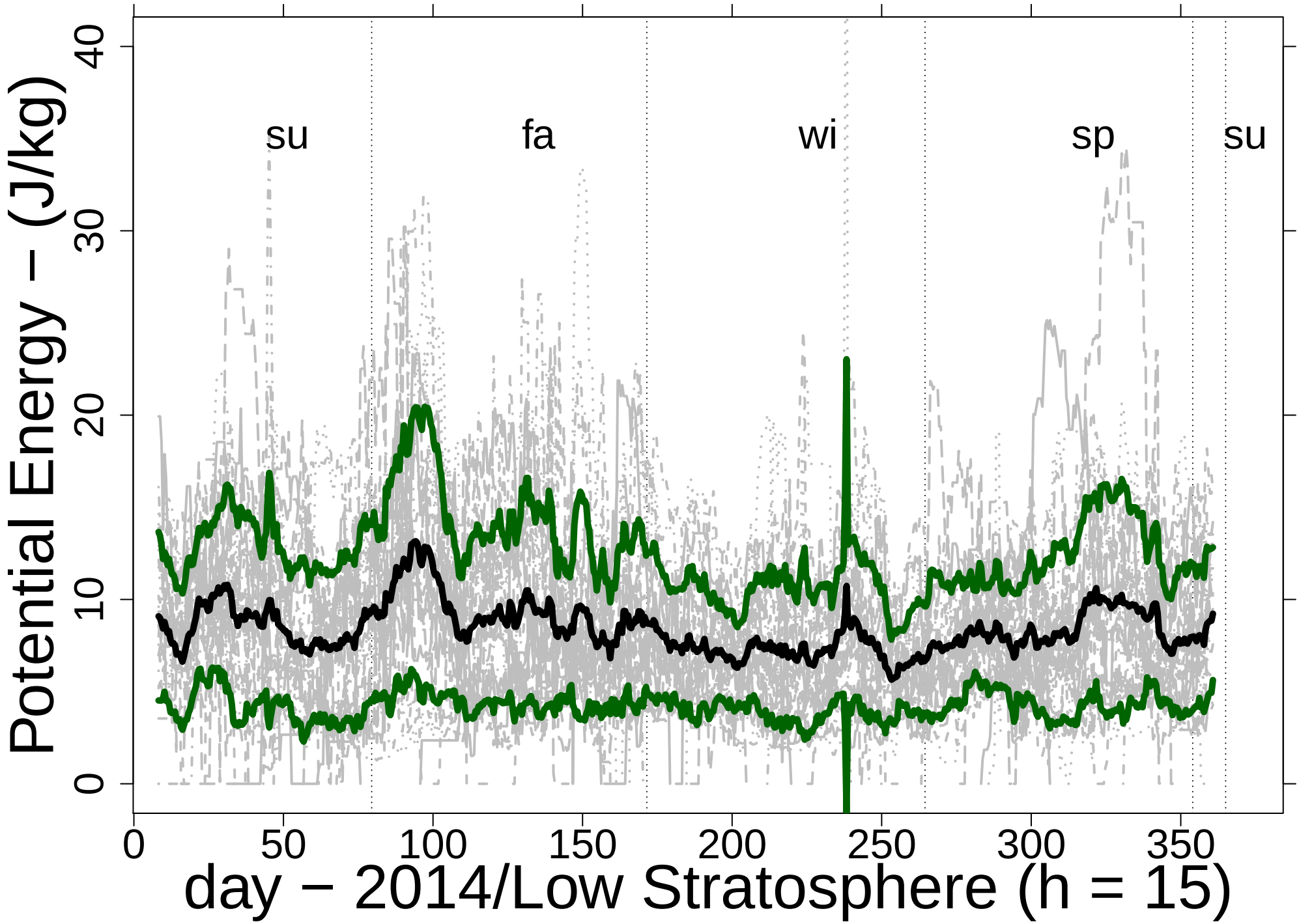
Potential Energy − (J/kg)
0
10
20
30
40
su
fa
wi
sp
su
0
50
100
150
200
250
300
350
day − 2014/Low Stratosphere (h = 15)

Figure.

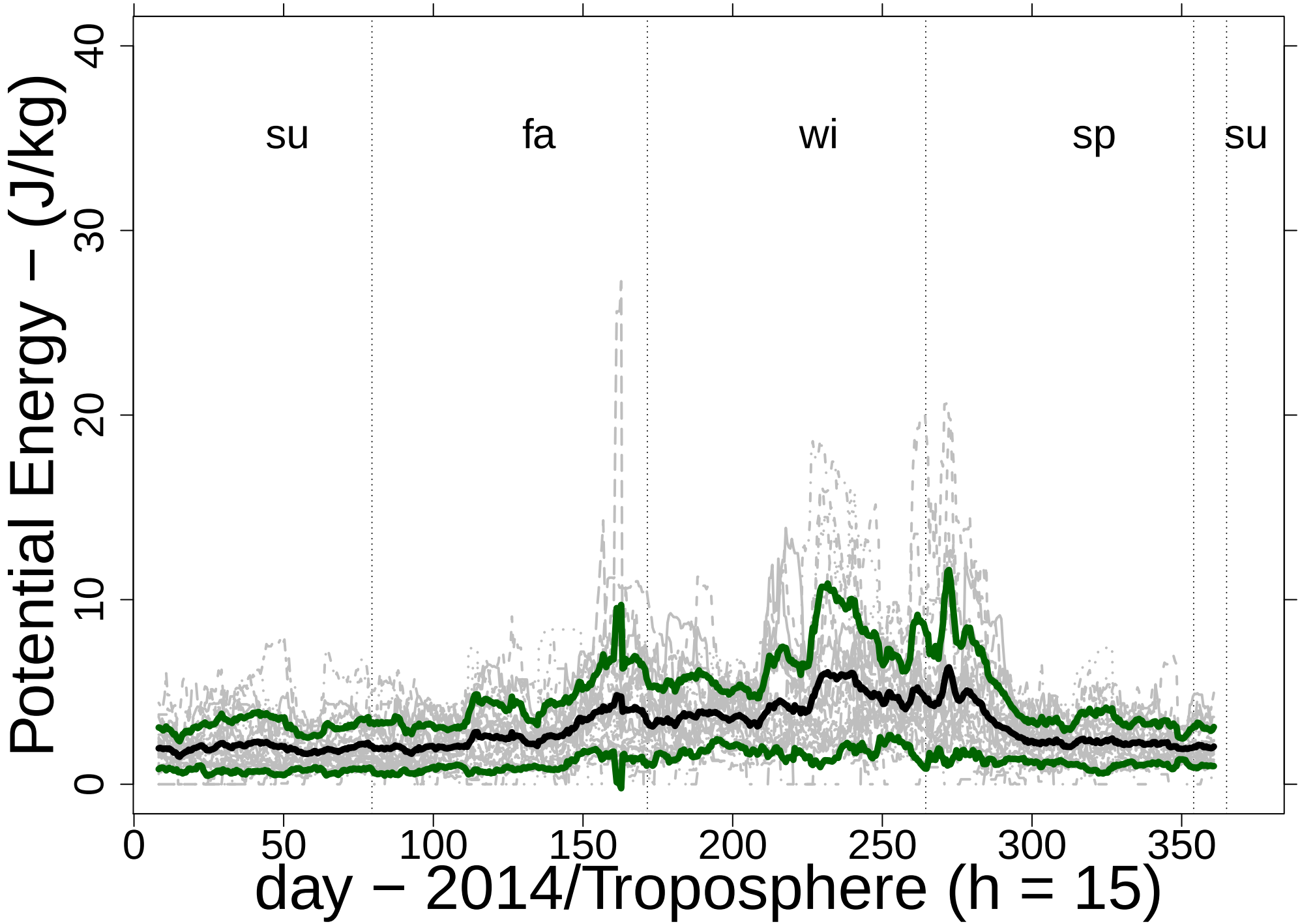
su
fa
wi
sp
su
Potential Energy − (J/kg)
0
10
20
30
40
0
50
100
150
200
250
300
350
day − 2014/Troposphere (h = 15)

Figure.

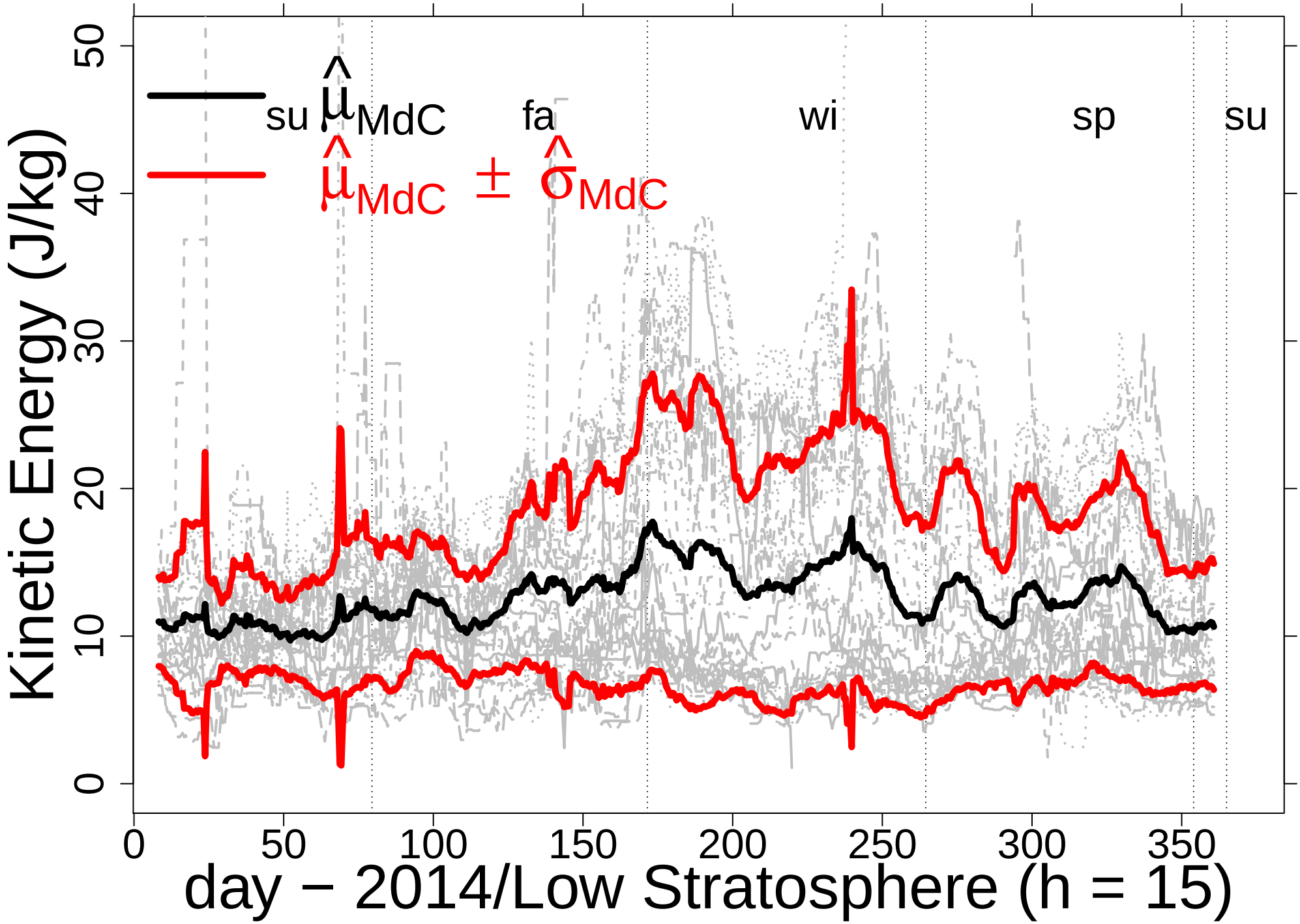
Kinetic Energy (J/kg)
0
10
20
30
40
50
su
fa
wi
sp
su
$\hat{\mu}_{MdC}$
$\hat{\mu}_{MdC} \pm \hat{\sigma}_{MdC}$
0
50
100
150
200
250
300
350
day − 2014/Low Stratosphere (h = 15)

Figure.

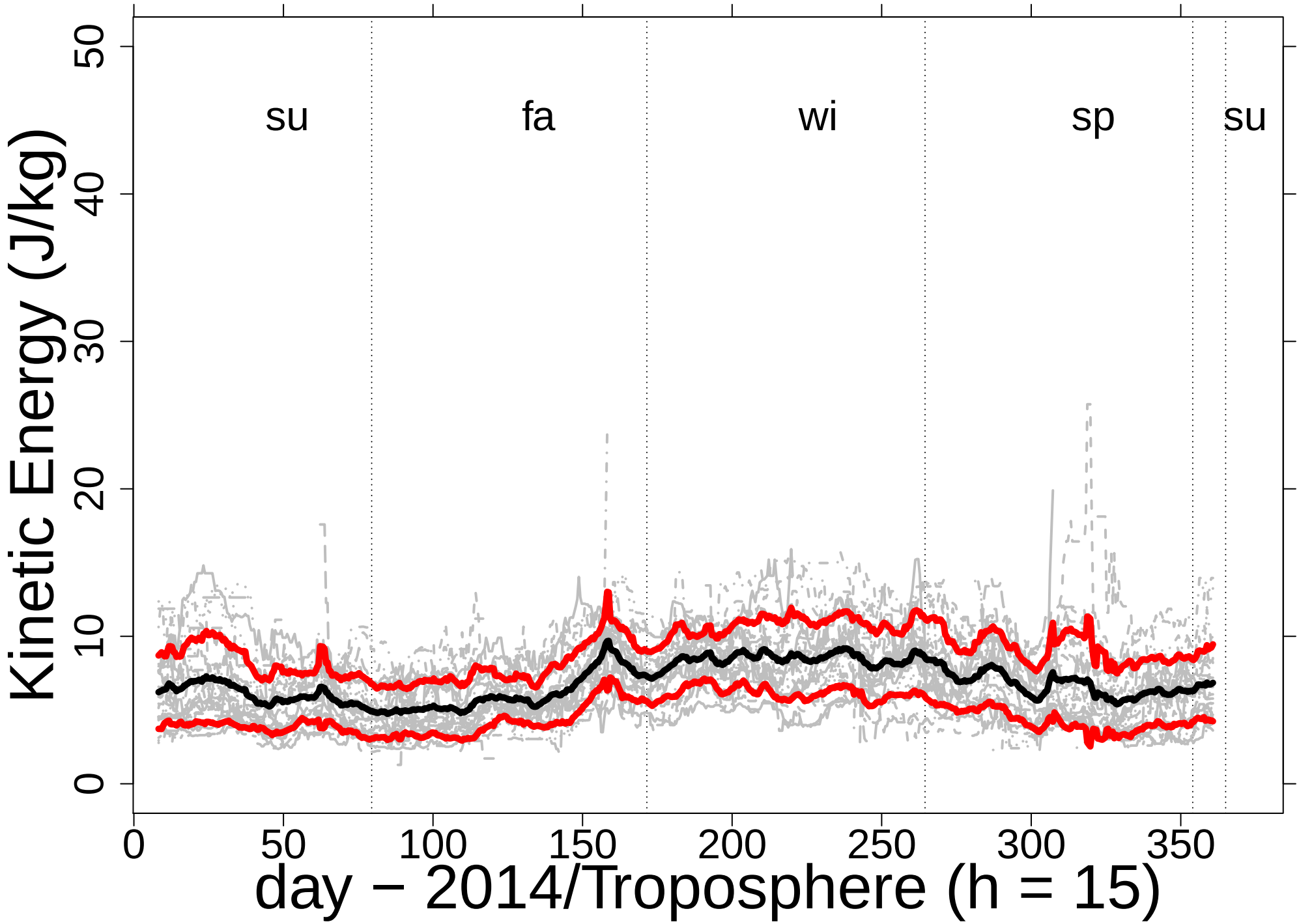
su
fa
wi
sp
su
Kinetic Energy (J/kg)
0
10
20
30
40
50
0
50
100
150
200
250
300
350
day − 2014/Troposphere (h = 15)

Figure.

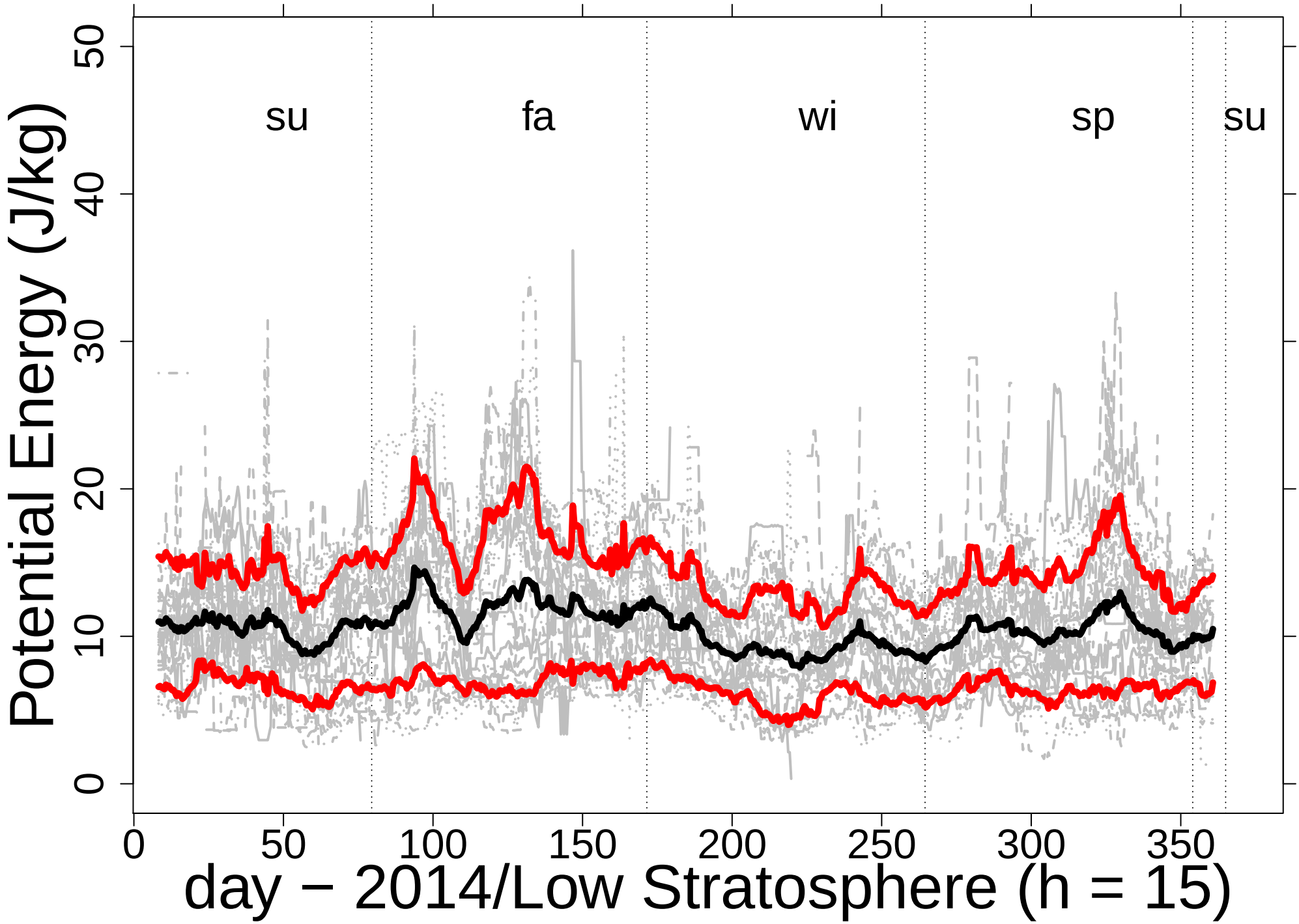
su
fa
wi
sp
su
Potential Energy (J/kg)
0
10
20
30
40
50
0
50
100
150
200
250
300
350
day − 2014/Low Stratosphere (h = 15)

Figure.

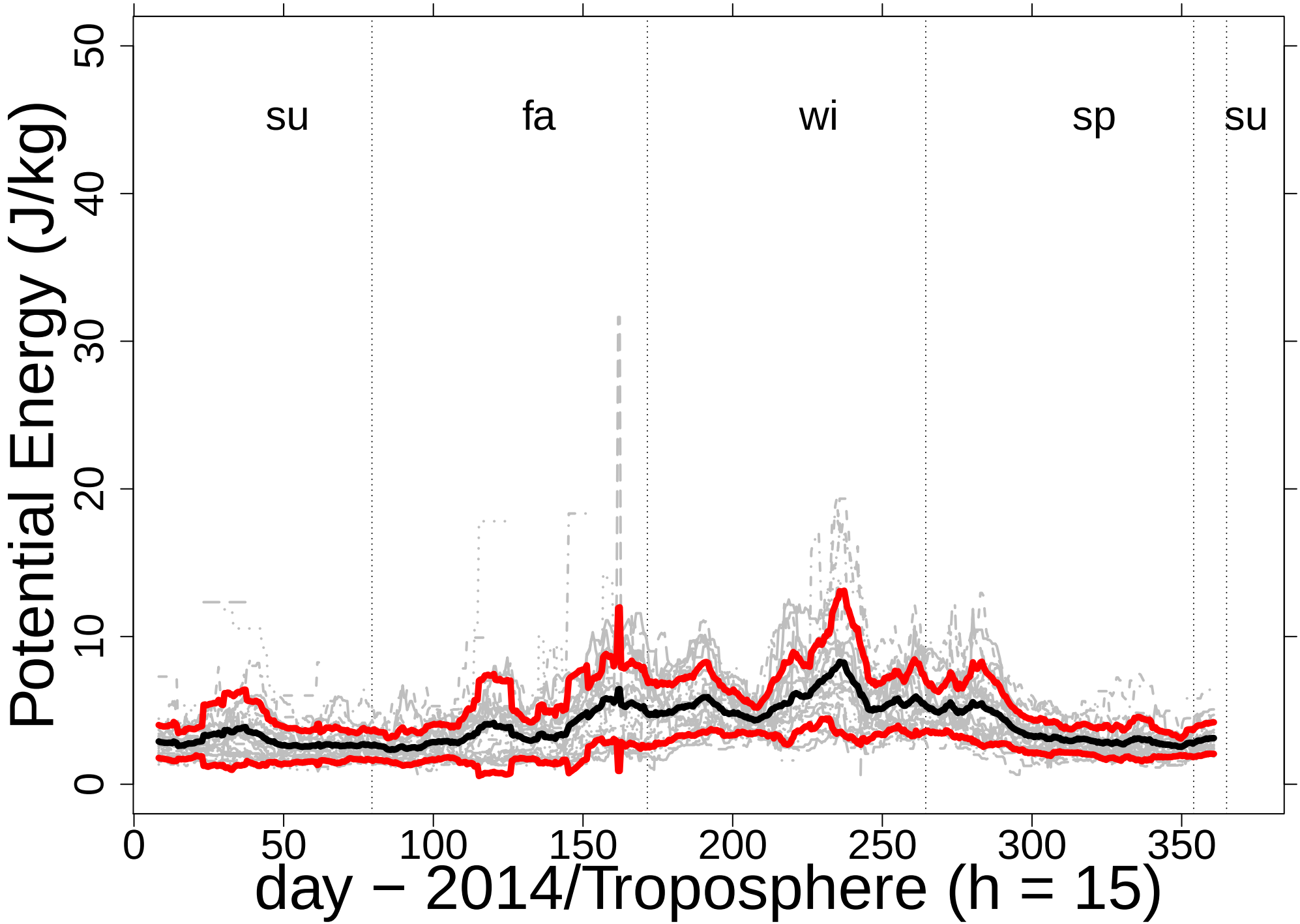
Potential Energy (J/kg)
0
10
20
30
40
50
su
fa
wi
sp
su
0
50
100
150
200
250
300
350
day − 2014/Troposphere (h = 15)

Figure.

Gravity Waves/Low Stratosphere/2014

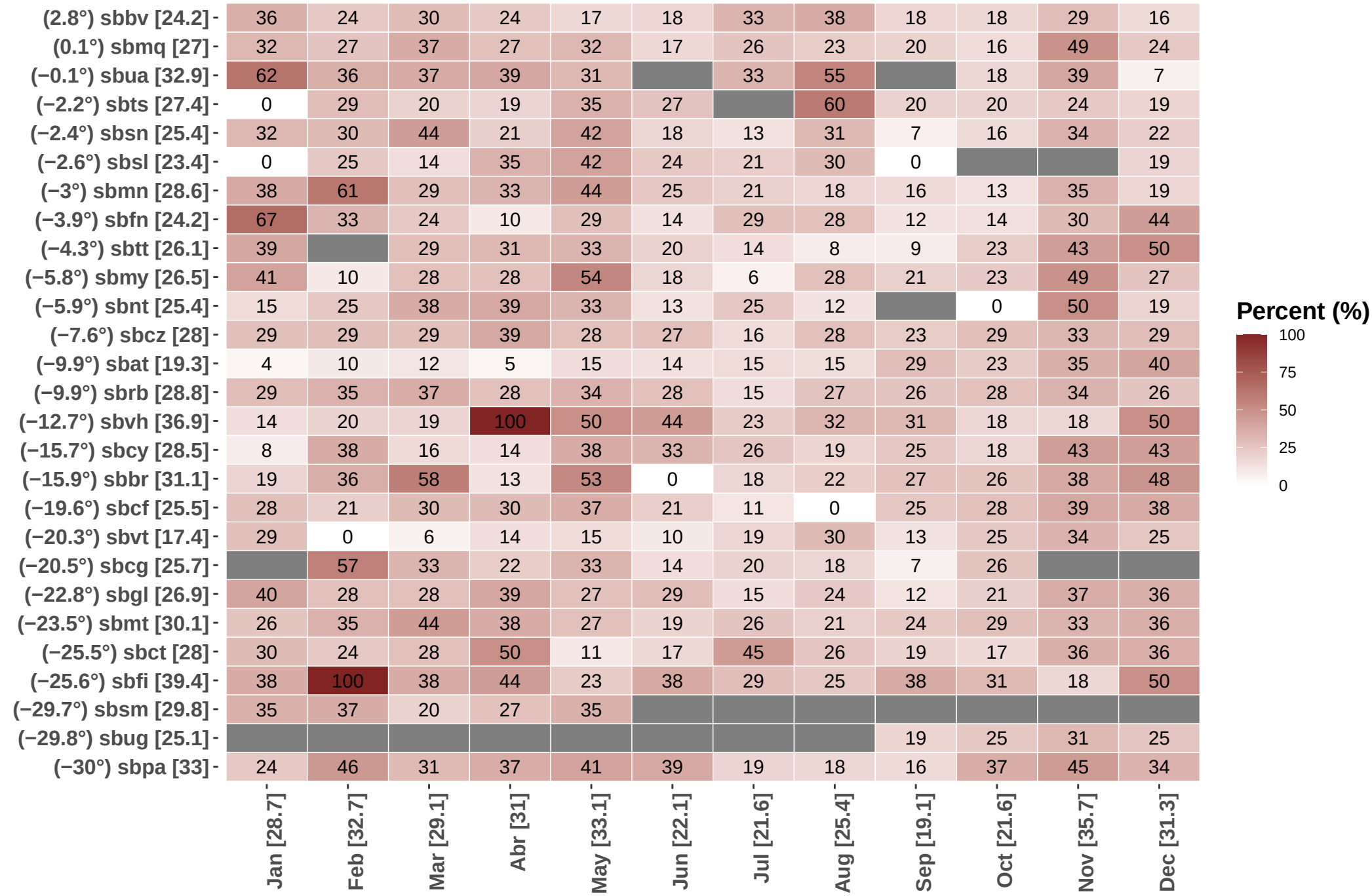

Figure.

Gravity Waves/Troposphere/2014

	Jan [28.6]	Feb [26.7]	Mar [20.5]	Abr [25.4]	May [21.5]	Jun [28]	Jul [27]	Aug [25.9]	Sep [26.2]	Oct [27.6]	Nov [23]	Dec [26.9]
(2.8°) sbbv [26.2]	5	38	28	20	38	32	11	28	28	25	17	23
(0.1°) sbmq [23.6]	15	20	31	16	29	31	30	31	20	17	13	21
(−0.1°) sbua [35]	100	40		33	17		43	29		43	40	
(−2.2°) sbts [21.1]		0	31	26	12	36		18	28	16	24	21
(−2.4°) sbsn [23.9]	35	42	19	24	22	22	23	19	18	29	14	31
(−3.9°) sbfn [25.1]	50	28	24	15	17	17	34	21	50	23	21	26
(−4.3°) sbtt [28.7]	22		0	38	23	30	25	80	8	14	25	44
(−5.8°) sbmy [30]	37	33	23	23	41	56	32	24	15	26	23	35
(−5.9°) sbnt [12.7]	50	25	0	0	0		56	0		33	0	0
(−8.7°) sbpv [24.8]	11	23	38	20	16	24	29	31	25	12	35	20
(−9.9°) sbat [17]	7	13	3	11	9	13	15	19	39	21	21	23
(−9.9°) sbrb [8.6]	50	0	33	0	0	12	20	0	0	0	0	29
(−12.7°) sbvh [32.2]	9	25	24	27	24	32	26	34	28	36	31	67
(−15.7°) sbcy [34.6]	14	38	7	67	45	34	27	27	43	30	31	32
(−15.9°) sbbr [24.1]	32	25	18	29	19	32	34	15	7	55	15	16
(−19.6°) sbcf [26]	21	21	21	26	16	36	26	31	29	33	21	28
(−20.3°) sbvt [19.2]	11	11	7	5	7	24	24	33	25	19	34	21
(−20.5°) sbcg [25.7]		24	22	14	21	28	20	21	35	47		
(−22.8°) sbgl [27.8]	60	37	15	21	29	29	31	30	21	43	26	25
(−23.3°) sblo [33.3]	0	50	25	33	25	33						
(−23.5°) sbmt [23.3]	39	19	19	27	26	31	21	17	26	26	29	16
(−25.5°) sbct [28]	26	15	28	32	23	38	32	27	38	31	17	27
(−25.6°) sbfi [29.5]	26	50	28	25	29	15	15	26	30	41	38	28
(−27.7°) sbfl [28.5]	42	27	23	34	31	24	26	32	29	23	23	42
(−29.7°) sbsm [35.5]	29	32	29	67	14							
(−29.8°) sbug [24.3]	0								21	28	29	21
(−30°) sbpa [25]	23	30	17	27	27	15	21	29	40	21	23	26

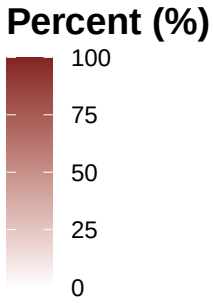

Figure.

Gravity Waves/Low Stratosphere/2014

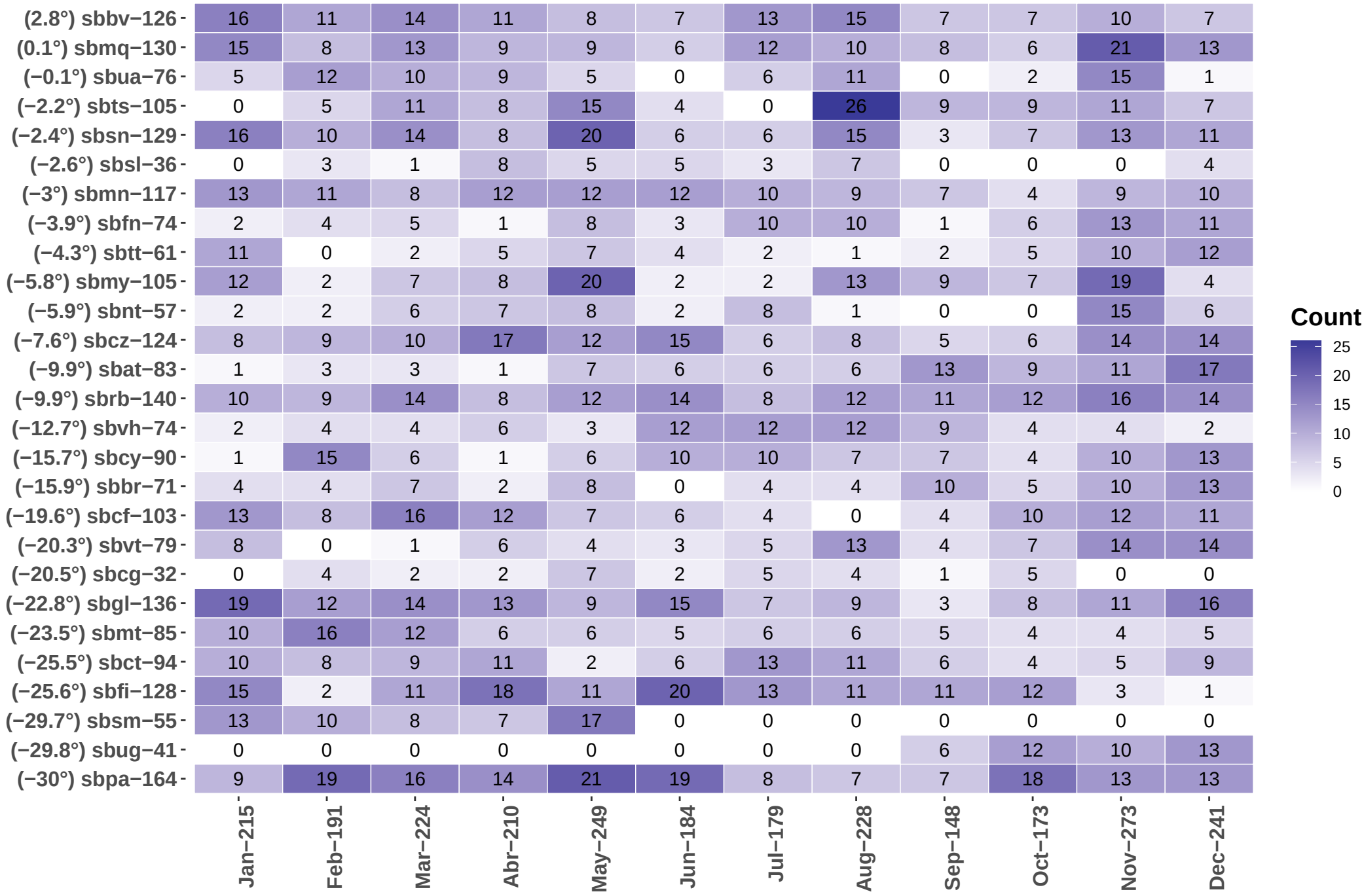

Figure.

Gravity Waves/Troposphere/2014

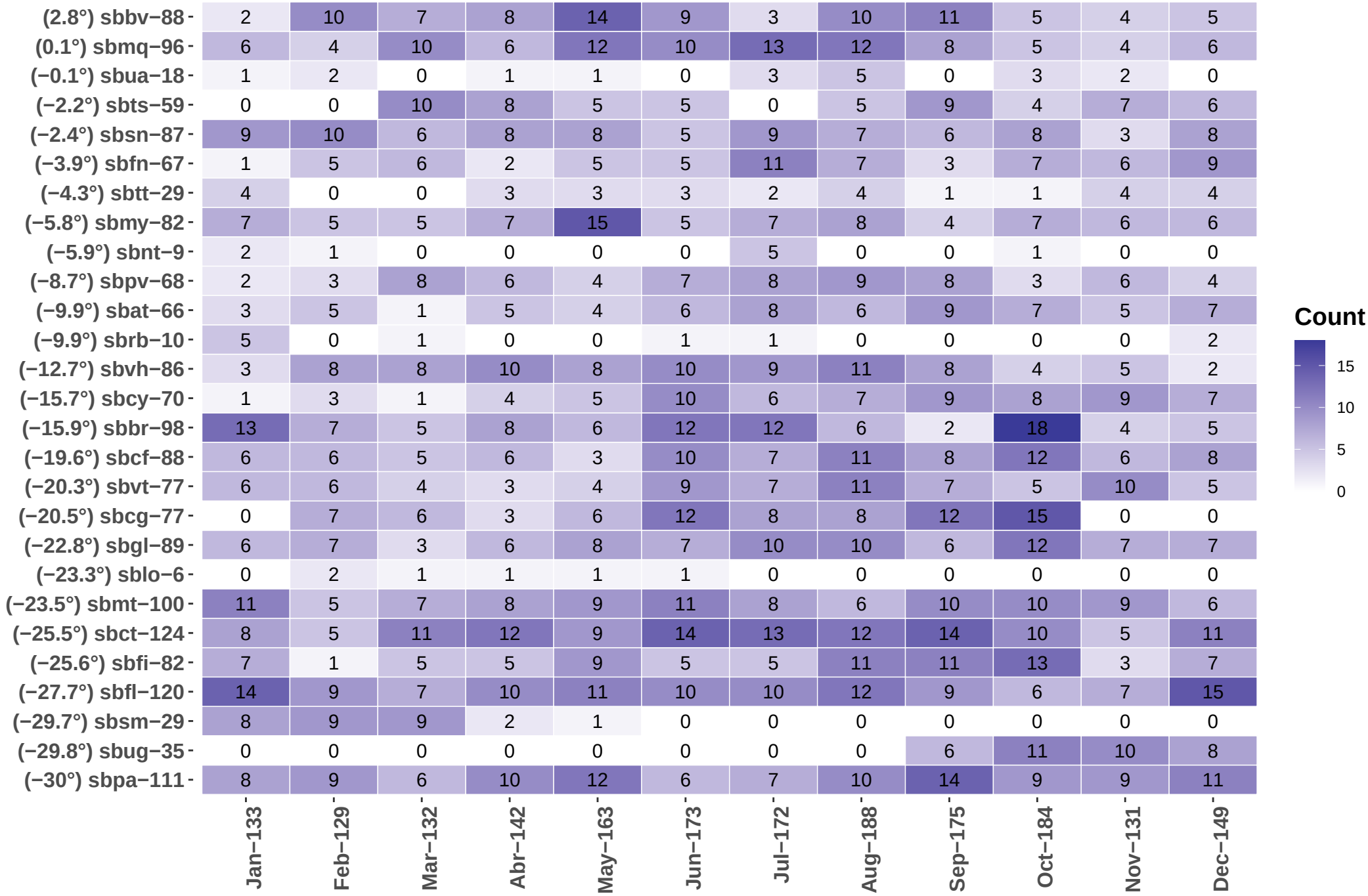

Figure.

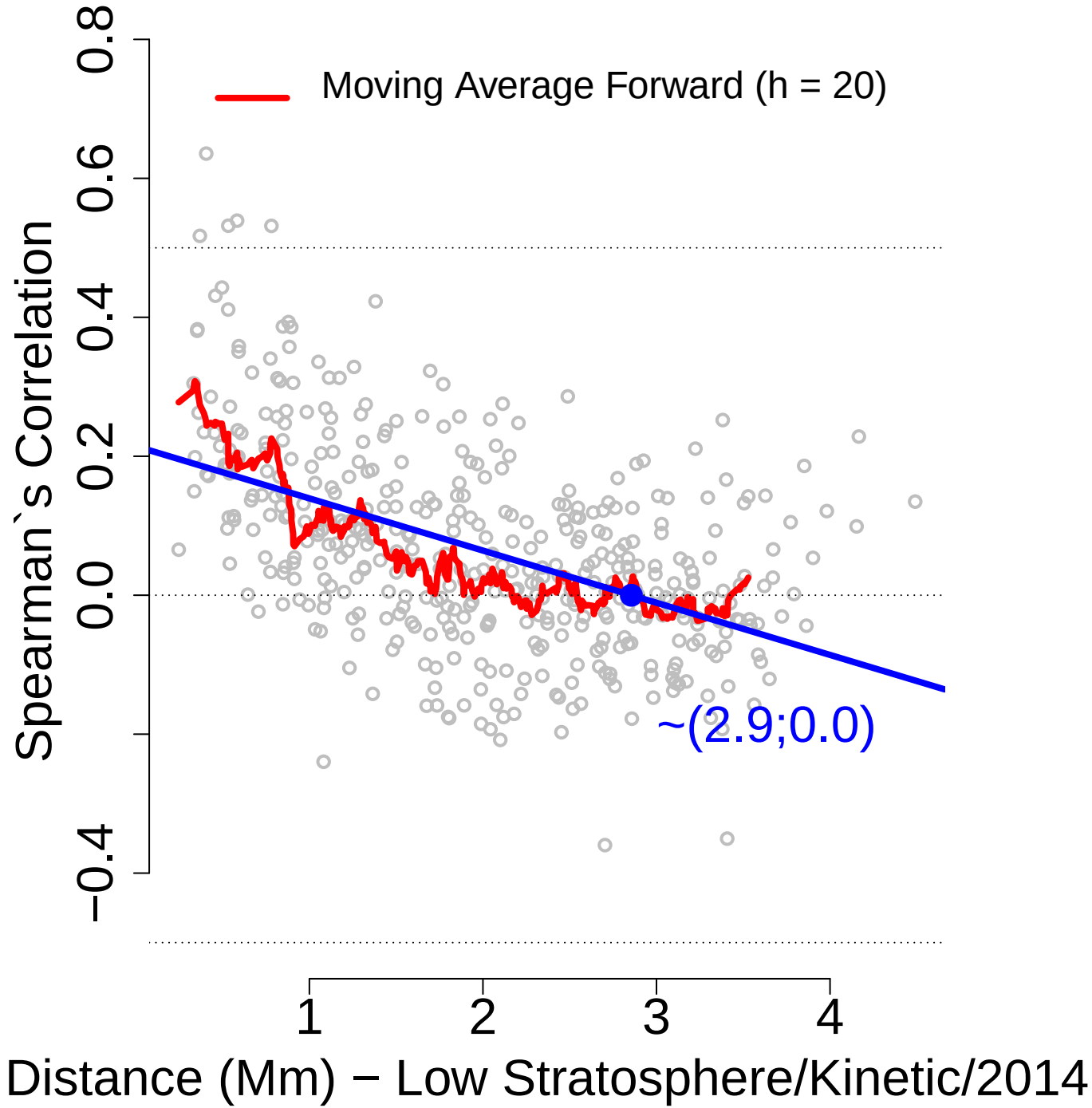
Moving Average Forward (h = 20)
Spearman`s Correlation
0.8
0.6
0.4
0.2
0.0
−0.4
~(2.9;0.0)
1
2
3
4
Distance (Mm) − Low Stratosphere/Kinetic/2014

Figure.

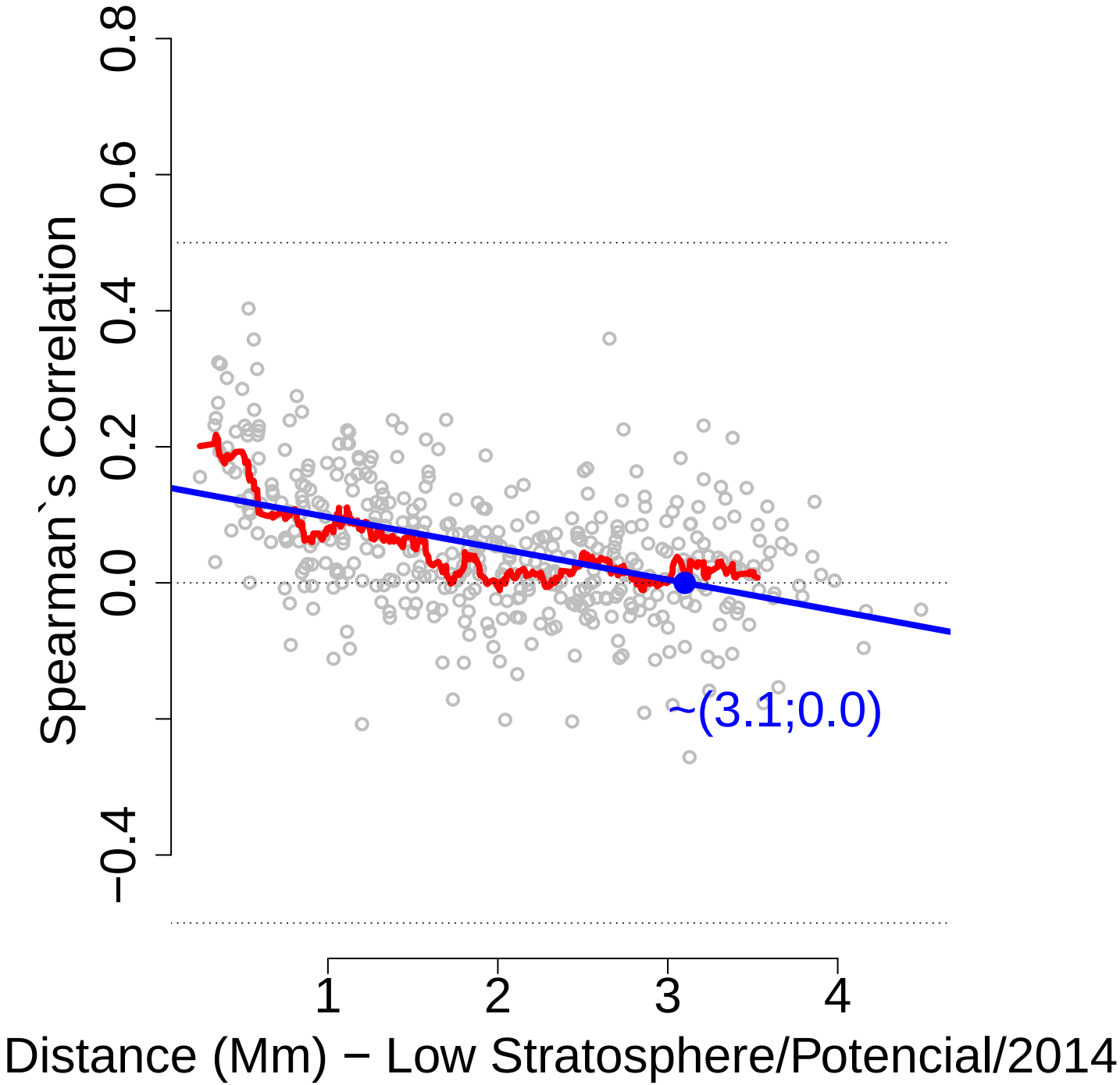
Spearman`s Correlation
0.8
0.6
0.4
0.2
0.0
−0.4
~(3.1;0.0)
1
2
3
4
Distance (Mm) − Low Stratosphere/Potencial/2014

Figure.

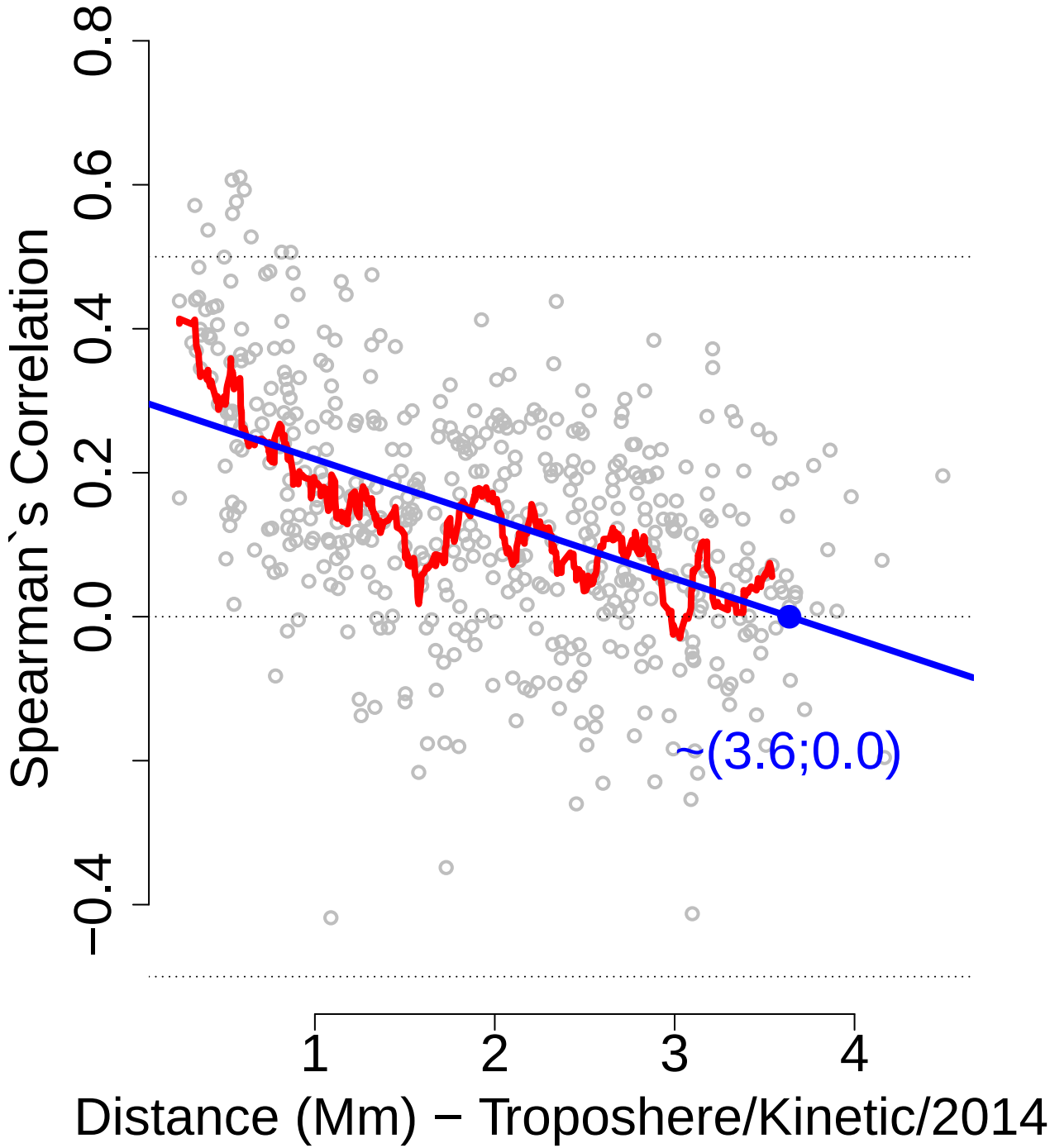
Spearman`s Correlation
0.8
0.6
0.4
0.2
0.0
−0.4
~(3.6;0.0)
1
2
3
4
Distance (Mm) − Troposhere/Kinetic/2014

Figure.

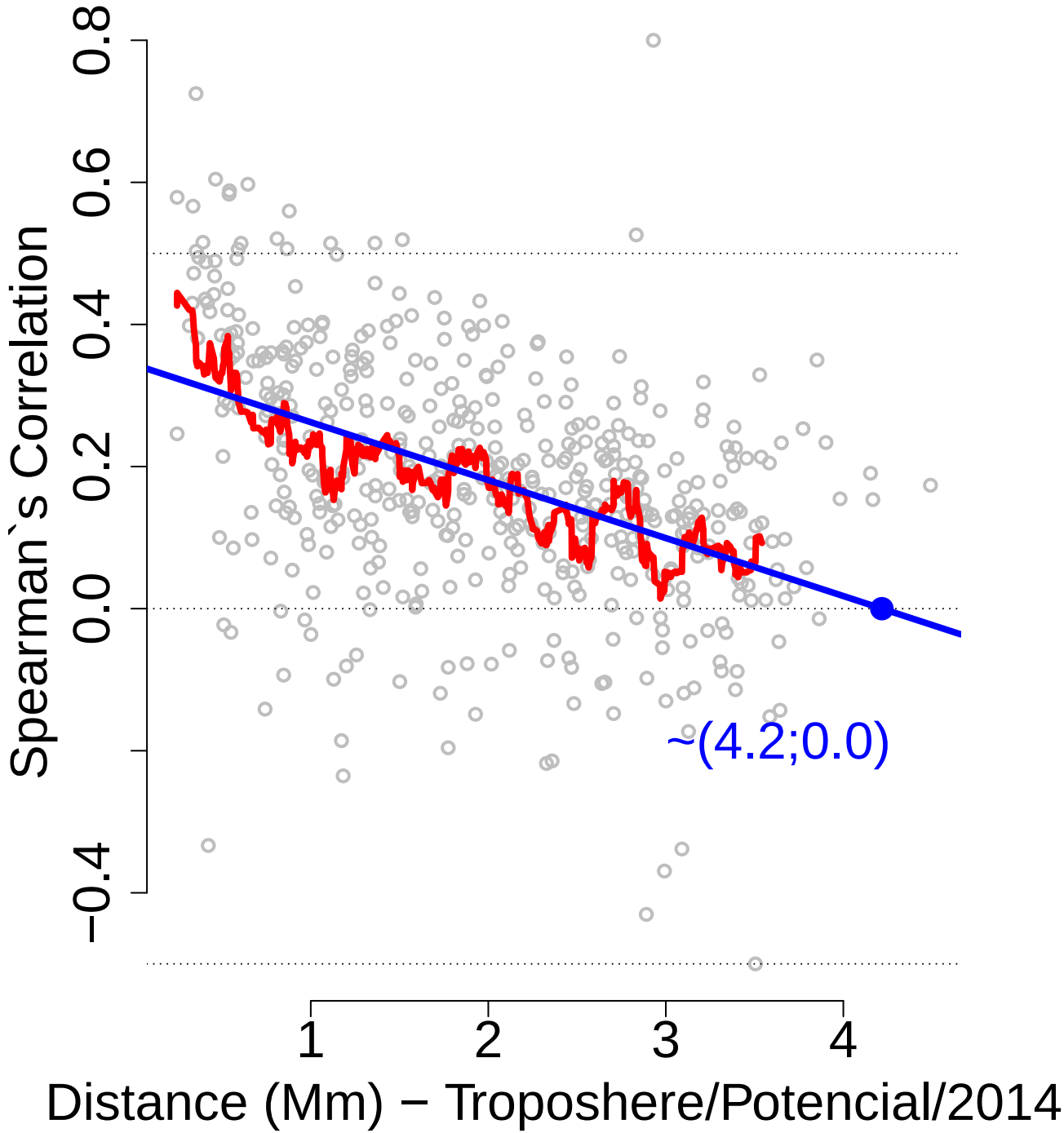
Spearman`s Correlation
0.8
0.6
0.4
0.2
0.0
−0.4
~(4.2;0.0)
1
2
3
4
Distance (Mm) − Troposhere/Potencial/2014

Figure.

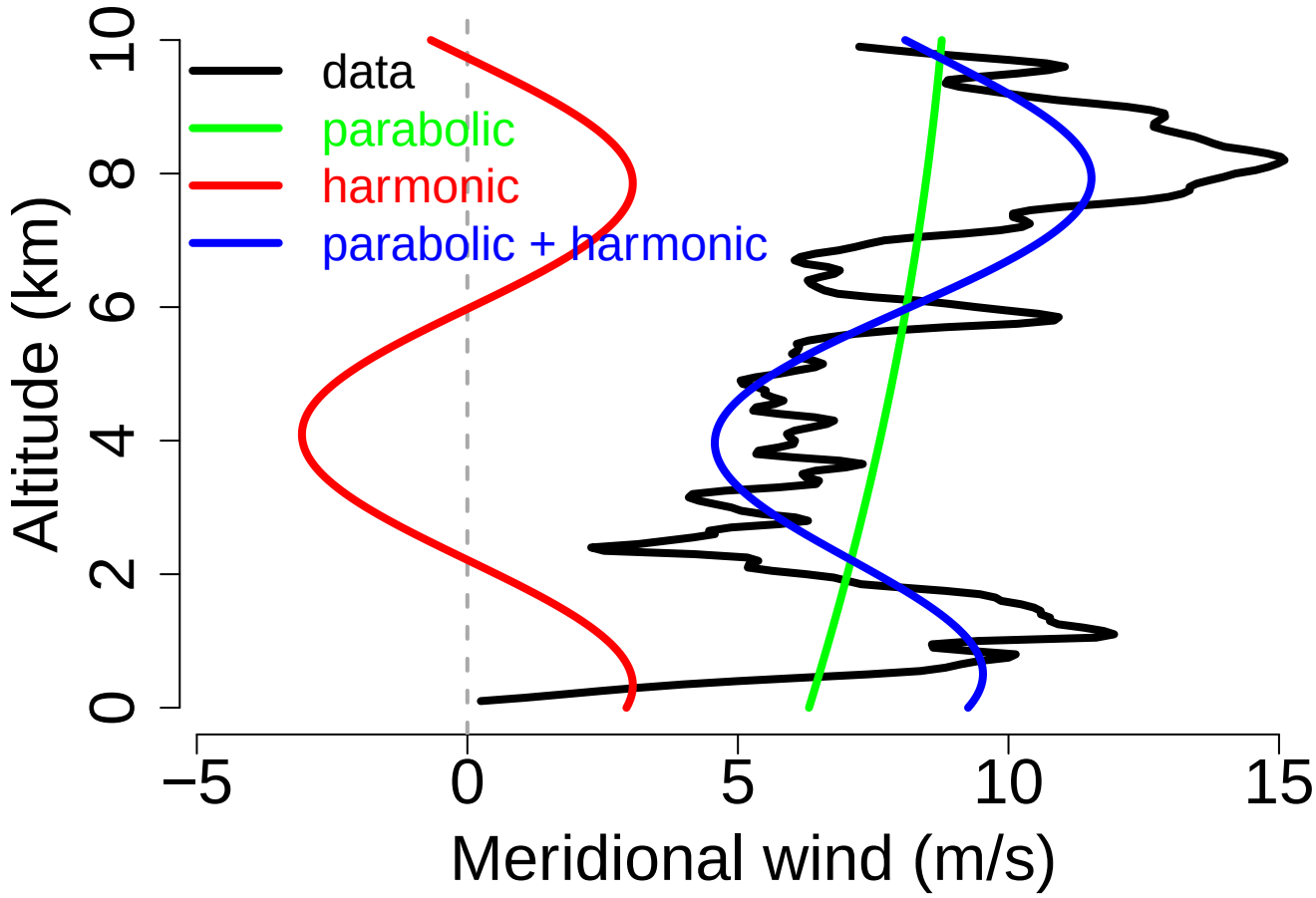
data
parabolic
harmonic
parabolic + harmonic
Altitude (km)
0
2
4
6
8
10
−5
0
5
10
15
Meridional wind (m/s)